Universidade Federal do Espírito Santo
Centro Tecnológico
Programa de Pós-Graduação em Informática

Paulo Wander Barbosa

Tumor Growth Models via Phase-Field Modeling: Vascular and Mechanical aspects

Vitória - ES, Brasil

2020

TUMOR GROWTH MODELS VIA PHASE-FIELD MODELING: VASCULAR AND MECHANICAL ASPECTS

Paulo Wander Barbosa

Tese submetida ao Programa de Pós-Graduação em Informática da Universidade Federal do Espírito Santo como requisito parcial para a obtenção do grau de Doutor em Ciência da Computação.

Aprovada em 10 de junho de 2020:

Profª. Drª. Lucia Catabriga
Orientadora

Prof. Dr. Adriano M. A. Côrtes
Coorientador

Prof. Dr. Isaac Pinheiro dos Santos
Membro Interno

Prof. Dr. Ernesto Augusto Bueno da Fonseca Lima
Membro Externo

Prof. Dr. Fernando Pereira Duda
Membro Externo

Profª. Drª. Regina Célia Cerqueira Almeida
Membro Externo

UNIVERSIDADE FEDERAL DO ESPÍRITO SANTO
Vitória-ES, 10 de junho de 2020.

UNIVERSIDADE FEDERAL DO ESPÍRITO SANTO

PROTOCOLO DE ASSINATURA

O documento acima foi assinado digitalmente com senha eletrônica através do Protocolo Web, conforme Portaria UFES nº 1.269 de 30/08/2018, por
LUCIA CATABRIGA - SIAPE 297800
Departamento de Informática - DI/CT
Em 17/06/2020 às 09:35

Para verificar as assinaturas e visualizar o documento original acesse o link:
https://api.lepisma.ufes.br/arquivos-assinados/31230?tipoArquivo=O

UNIVERSIDADE FEDERAL DO ESPÍRITO SANTO

PROTOCOLO DE ASSINATURA

O documento acima foi assinado digitalmente com senha eletrônica através do Protocolo Web, conforme Portaria UFES nº 1.269 de 30/08/2018, por
ISAAC PINHEIRO DOS SANTOS - SIAPE 2299959
Departamento de Matemática Aplicada - DMA/CEUNES
Em 18/06/2020 às 15:48

Para verificar as assinaturas e visualizar o documento original acesse o link:
https://api.lepisma.ufes.br/arquivos-assinados/31687?tipoArquivo=O

Ficha catalográfica disponibilizada pelo Sistema Integrado de Bibliotecas - SIBI/UFES e elaborada pelo autor

---

Wander Barbosa, Paulo, 1974-
W245t Tumor Growth Models via Phase-Field Modeling: Vascular and Mechanical aspects / Paulo Wander Barbosa. - 2020.
135 f. : il.

Orientadora: Lucia Catabriga.
Coorientador: Adriano Maurício de Almeida Côrtes.
Tese (Doutorado em Informática) - Universidade Federal do Espírito Santo, Centro Tecnológico.

1. Crescimento Tumoral. 2. Campo de Fase. 3. Teoria da Mistura. 4. Modelagem Matemática. 5. Análise Isogeométrica. I. Catabriga, Lucia. II. Maurício de Almeida Côrtes, Adriano. III. Universidade Federal do Espírito Santo. Centro Tecnológico. IV. Título.

CDU: 004

ACKNOWLEDGEMENTS

First of all, I thank God, for being present throughout my life and especially during the construction of this work.

I thank my parents who, with all love, dedicated their lives to the family and education of their children.

I thank all family members for their unconditional support.

I thank my wife Ione and daughter Luiza, for understanding my absence in many moments and support in all circumstances.

I thank my advisor Lucia Catabriga, for her dedicated guidance and also for the encouragement and support at all times.

I thank my co-advisor Adriano Côrtez, for his availability in academic guidance, but mainly for his companionship along the way.

I thank the members of the board, for their kindness of careful reading and valuable suggestions.

I thank my friend Michel, for his encouragement and companionship during decades of friendship.

I also thank my friends and post-graduate colleagues Sérgio, Leonardo and Riedson for their collaboration throughout the course.

I thank the High Performance Computing Center (NACAD) of the Alberto Luiz Coimbra Institute for Graduate Studies and Research in Engineering (COPPE), of the Federal University of Rio de Janeiro (UFRJ) for the granted computational resources, and its support team for the availability.

I thank the High Performance Computing Laboratory - LCAD/Ufes, for providing physical space and computational resources throughout the course. Extending the thanks to its monitors.

ABSTRACT

In this work we study tumor growth models based on mixture theory, considering two classes of continuous macroscopic models: a phenomenological and a mechanical one. The former is a hybrid multi-scale partial differential equation model describing vascular solid tumor and capillaries growth, coupled with angiogenic factors and nutrients diffusion. The capillary phase is described by a diffuse-interface model, also known as a phase-field model, giving rise to a fourth-order parabolic partial differential equation. The tip cell dynamics, responsible for the capillary migration, is described by a discrete agent-based model. This model is able to represent the tumor growth and the development of angiogenesis. The mechanical model is developed on a continuum mechanics basis by means of a continuum mixture theory, also giving rise to a system of partial differential equations. Apart from the classical setting, the framework used incorporates the balance of microforces, engendering the possibility to model some of the phases (species) as a diffuse-interface model. A four species thermodynamically consistent mechanical model was developed. With this model, we expect to quantify the influence of stresses on the growth of solid tumors. All models shown in the numerical results were discretized using spline-based Isogeometric Analysis, and implemented in PetIGA, a parallel and high-performance implementation of Isogeometric Analysis on top of the *Portable Extensible Toolkit for Scientific Computation*, better known by the acronym PETSc.

Keywords: Tumor Growth, Theory of Mixture, Phase-Field, Mathematical Modeling, Isogeometric Analysis.

RESUMO

Neste trabalho, estudamos modelos de crescimento tumoral baseados na teoria da mistura, considerando duas classes de modelos macroscópicos contínuos: um fenomenológico e um mecânico. O primeiro é um modelo híbrido de equações diferenciais parciais multiescala que descreve o crescimento de tumores sólidos vasculares e capilares, juntamente com fatores angiogênicos e difusão de nutrientes. A fase capilar é descrita por um modelo de interface difusa, também conhecido como modelo de campo de fase, dando origem a uma equação diferencial parcial parabólica de quarta ordem. A dinâmica das células da ponta, responsável pela migração capilar, é descrita por um modelo discreto baseado em agentes. Este modelo é capaz de representar o crescimento de um tumor e o desenvolvimento da angiogênese. O modelo mecânico é desenvolvido com base na mecânica do continuum por meio de uma teoria da mistura do continuum, dando origem também a um sistema de equações diferenciais parciais. Além do cenário clássico, a estrutura utilizada incorpora o equilíbrio de micro-forças, gerando a possibilidade de modelar algumas das fases (espécies) como um modelo de interface difusa. Um modelo mecânico termodinamicamente consistente de quatro espécies foi desenvolvido. Com este modelo, espera-se quantificar a influência das tensões no crescimento de tumores sólidos. Todos os modelos mostrados nos resultados numéricos foram discretizados usando a Análise Isogeométrica baseada em splines e implementados no PetIGA, uma implementação paralela e de alto desempenho da Análise Isogeométrica sobre o *Portable Extensible Toolkit for Scientific Computation*, mais conhecido pela sigla PETSc.

Palavras-chave: Crescimento Tumoral, Campo de fase, Teoria da mistura, Modelagem Matemática, Análise isogeométrica.

LIST OF FIGURES

LIST OF TABLES

CONTENTS

1 INTRODUCTION

The World Health Organization estimates that 9.6 million people lost their lives in 2018 due to cancer and 18.1 million new cases were detected [1]. This alarming number of deaths is motivating the scientific community to collaborate in the development of research capable of improving the understanding of the cancer dynamics and the current treatments available, aiming at the minimization of deaths. In recent years, many mathematical models of tumors have been developed. The research, development, and improvement of these models have great potential to accelerate the development of drugs and optimize treatments, besides replacing part of the research *in vivo* with *in silico* research, reducing the use of live guinea pigs.

The modeling of the diffusion in biological tissues, presented by Hill A. V. (1928), was the basis for mathematical models on the growth of solid tumors to be developed in the following years. The exponential, logistic and Gompertz models were used in many of them (Laird, 1964) (Garg and Miga, 2008). In the last decades, new approaches have been used in modeling tumor growth.

Generally, tumor growth models use discrete, continuous or hybrid techniques to capture the phenomena involved in the development of the tumor. Continuous models are able to show the general behavior of tumor growth, modeling the average behavior at the population level and fail to examine phenomena that occur at the single cell level (Bellomo et al., 2008). Discrete models can represent individual cells, track and update their internal states, incorporate biological rules, such as those that define the cell-cell and cell-matrix interactions involved in chemotaxis and haptotaxis (Deisboeck et al., 2011). A great computational demand is generated when describing details of the individual behavior of the cells, limiting the discrete models to the control of a relatively small number of cells (Deisboeck et al., 2011). In hybrid models, individual cells are treated discretely, but interact with other fields on the continuum (Roose et al., 2007).

A timeline describing the main facts in the history of mathematical modeling of tumor growth is presented in (Byrne, 2010). Among these facts, we highlight the presentation of the first biomechanical model of an avascular tumor (Greenspan, 1976), the first model of avascular tumor growth using mixture theory (Ward and King, 1997), and the first multiscale model of vascular tumor growth (Alarcón et al., 2004). According to Lowengrub et al. (2009), the first mathematical model focusing on angiogenesis was developed by Balding and McElwain (1985). Stokes and Lauffenburger (1991) developed the first discrete model describing angiogenesis, where each sprout is treated individually (Lima

[1] http://www.who.int/cancer/en/

et al., 2014). Chaplain and Stuart (1993) improved a continuous one-dimensional model, which describes the diffusion of angiogenic factors in the surrounding tissue, presented in (Chaplain and Stuart, 1991), to evaluate their effects on the endothelial cells of neighboring blood vessels. For a more detailed look at the history of tumor growth modeling, see Araujo and McElwain (2004), Bellomo et al. (2008).

The modeling of tumor growth requires a certain degree of minimum knowledge in some areas such as Biology, Chemistry, Mathematics and Physics. Moreover, the equations or systems of equations that govern these models generally have no analytical solution. Thus, knowledge in numerical methods is indispensable for the solution and analysis of these models. The tumor growth models presented in this work are based on mixture theory and belong to the class of continuous macroscopic models, one being phenomenological and the other mechanical.

The phenomenological model is a hybrid model of partial differential equations that operates on two scales. The model describes the growth of solid tumors, in their avascular and vascular phases, the awakening of angiogenesis, the development of capillaries and the diffusion of angiogenic factor and nutrient. The capillary phase is described by a diffuse interface model, also known as a phase field model, giving rise to a fourth order parabolic partial differential equation. The tip cell dynamics responsible for capillary migration are described by a discrete agent-based model. This model, presented in Chapter 4, is able to represent the growth of a tumor and the development of angiogenesis. It is based on Xu et al. (2016) and has been tested in the challenge of representing new tumor and capillary configurations.

The mechanical model is developed based on continuum mechanics through a theory of continuum mixture, also defined by a system of partial differential equations. In addition to the classical scenario, the structure used incorporates the microforce balance, generating the possibility of modeling some of the phases (species) as a diffuse interface model. A thermodynamically consistent mechanical model of four species was developed based on Faghihi et al. (2018). With this model, it is expected to quantify the influence of stress on the growth of solid tumors. The mechanical model is presented in Chapter 5.

All models shown in the numerical results were discretized using spline-based Isogeometric Analysis and implemented in PetIGA, a high-performance, parallel implementation of Portable Isogeometric Analysis, Extensible Toolkit for Scientific Computation, better known as PETSc. Chapter 3 provides a short presentation of the Isogeometric Analysis and PetIGA.

When presenting research in a multidisciplinary area, it is important to remember that not all people interested in the research have a multidisciplinary background. A mathematician is unlikely to know about details of a cell, while a biologist may not know thermodynamic laws. Contemplating and clarifying every detail of each area is impossible,

but a brief review can provide important definitions and indicate specialized references. That is the goal of Chapter 2.

1.1 Contributions of this thesis

This thesis aims to contribute to the study of development and numerical solution of tumor growth models. The most expressive contributions are listed below:

- The use of the PetIGA tool for the implementation of the models consisting of a system of fourth order partial differential equations, with good results in 2D and 3D;
- The implementation of a model that combines a fourth order system with angiogenesis in 2D and 3D. This model has a discrete part on agent-based, implemented in C/C++ using STL data structure. The discrete part operates between the time steps, analyzing the tumor environment and checking the conditions necessary for the development of angiogenesis. Inspired by Lima et al. (2014), we incorporated the conductivity tensor into the model, giving more realism to the capillary advance towards the tumor;
- Blocking angiogenesis and using a different initial configuration, with a tumor closer to the vessel, revealed that the model was able to capture most of the characteristics of a tumor cord. The model studied was able to capture the movement of a spherical tumor towards the vessel. After encircle the vessel, the tumor grows radially and along the vessel, forming a cylindrical structure. The model also managed to capture tumor morphology as well as nutrient distribution thus, delimiting the proliferative and hypoxic layers;
- Construction of a mechanical model, thermodynamically consistent and of four species, based on the ideas of Oden et al. (2010) and Faghihi et al. (2018). With this model, we intend to describe the physical forces acting on solid and fluid species during tumor growth.

1.2 Thesis outline

This thesis is organized as follows: Chapter 2 is dedicated to give a brief introduction and review of some biological and physical concepts used throughout the text. Chapter 3 provides a brief introduction to the Isogeometric analysis and the presentation of the PetIGA tool used in the implementation of the models. In Chapter 4, we present the phenomenological model of tumor growth with angiogenesis (Xu et al., 2016) and the improvements made in the model. Chapter 5 describes a thermodynamically consistent

mechanical model for tumor growth based on Faghihi et al. (2018) and Oden et al. (2010). In chapter 6 we present the numerical experiments related to the phenomenological model.

2 PRELIMINARIES

2.1 Fundamentals of biology

The onset and the development of tumors in the body are quite complex and involve a large number of events at different scales, namely, molecular (microscopic), cellular (mesoscopic), and tissue scales (macroscopic). Many events of the molecular scale occur within the cells, including the interpretation of external signals received by receptors on cell surfaces and nutrient uptake. The molecular machinery is responsible to orchestrate cell's functionality. Examples on the cellular scale phenomena are necrosis, apoptosis, cell division, and migration, besides the interactions among tumor cells and the other types of cells present in the body such as endothelial cells (Bussolino et al., 2003). on this scale, the collective behavior of the cells composing a tumor tissue is detectable, generally by its morphological changes when compared to the healthy tissue nearby. We describe in this section a few details of these complex multi-scale biological phenomena affecting millions of people per year diagnosticated with a tumor.

2.1.1 Cell cycle

The cells of our body have genetically programmed mechanisms that control how often they can divide, their differentiation and when their life cycle ends, keeping the appropriate number of each cell type. The *cell cycle* is a well-linked sequence of events that governs cell life and is divided into two major phases: interphase and mitosis (Weinberg, 2014). The interphase comprises the entire period between the beginning of the cell's life cycle and mitosis. It is subdivided into 3 phases: $\mathbf{G_1}$, $\mathbf{S}$, and $\mathbf{G_2}$. The $\mathbf{G_1}$ phase is where the newly formed cell initiates the cycle, at which time the cell develops, grows, and assumes its specific functions relative to its type. The $\mathbf{S}$ phase (synthesis) is the stage where the DNA is duplicated. In $\mathbf{G_2}$ phase the cell carries out the duplication of other components that will form the new cells. The mitotic phase, $\mathbf{M}$, is when the cell divides itself into two identical (daughter) cells and is also decomposed into four phases: prophase, metaphase, anaphase, and telophase. Finally, the $\mathbf{G_0}$ phase, which is located in the $\mathbf{G_1}$ phase, happens whenever the cell is not proliferating, also named, in quiescent state. For example, neurons remain in the $\mathbf{G_0}$ phase throughout their life. A representation of the cell cycle and its subdivisions is given in Figure 2.1.

In order to avoid flaws in the cell duplication process, the cell cycle has checkpoints to monitor each step, evaluating whether the cells have met the requirements to move to the next stage, or whether there is any kind of mutation. Upon detecting a failure,

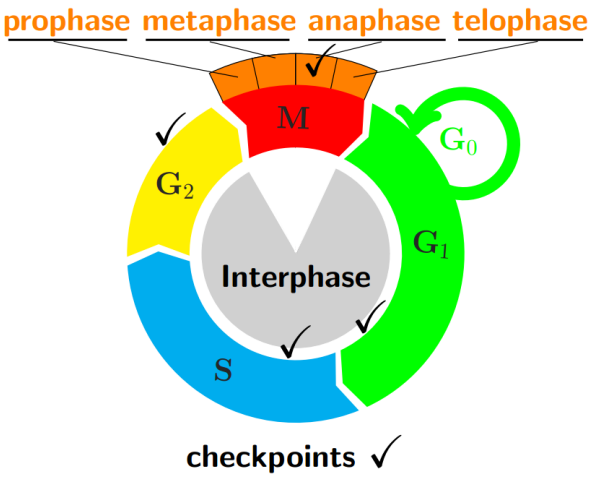

Figure 2.1 – The cell cycle and checkpoints - adapted from (Cristini and Lowengrub, 2010)

the process is interrupted until the problem is resolved. If the cell is severely damaged it will be induced to apoptosis (self-destruction). If the genome is damaged, the entry into the **S** phase is blocked at one of the checkpoints or a checkpoint stops DNA replication. In $\mathbf{G_2}$, a checkpoint does not allow entry into phase **M** if the DNA replication is not complete. Already in phase **M**, a checkpoint checks the last details before cell division is completed. Some checkpoints are represented in Figure 2.1. For more details on the cell cycle, see Weinberg (2014).

2.1.2 The Hallmarks of cancer

Some genetic and epigenetic[1] changes may accumulate in some cells over time, causing failures in the mechanism that controls cell life. These failures can generate a cluster of cells with the same problems forming a tumor. A large number of neoplastic diseases (tumors) with different characteristics affect the human being in various parts of the body. In order to provide a logical structure to organize and facilitate the understanding of the diversity of these diseases, Hanahan and Weinberg (2000) proposed six fundamental characteristics for these diseases, that can be classified as cancer (malignant tumor):

1- *Self-sufficiency in growth signals.*
2- *Insensitivity to anti-growth signals.*
3- *Evading apoptosis.*
4- *Sustained angiogenesis.*
5- *Limitless replicative potential.*
6- *Tissue invasion and metastasis.*

In Figure 2.2 we have the description of the six signs and the symbology used by Hanahan and Weinberg (2000).

[1] Heritable changes in gene expression that are not encoded in the genome (Tannock et al., 2013).

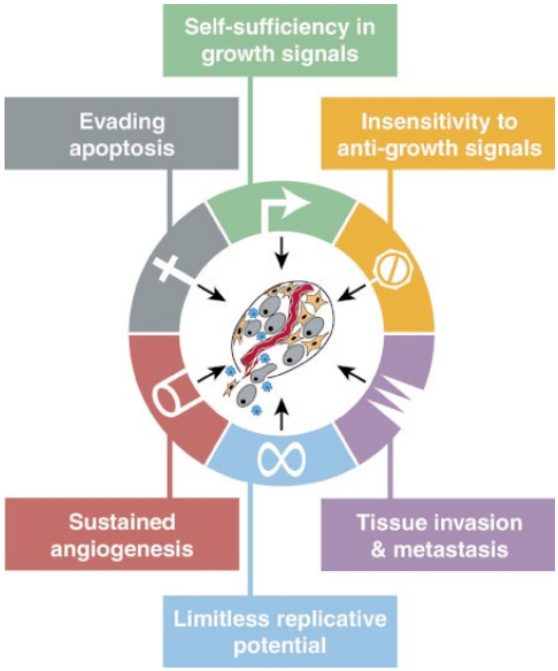

Figure 2.2 – The hallmarks of cancer - reproduced from Hanahan and Weinberg (2000).

In 2011, the list was extended adding four new characteristics (Hanahan and Weinberg, 2011). Two of them are actually enabling characteristics that contribute to the cells being able to acquire the six initial hallmarks: *Genomic Instability in Cells and Mutation* and *Tumor-Promoting Inflammation*. The other two hallmarks added are: *Cellular Energy Deregulation* and *Avoiding Immune Destruction*. In Figure 2.3, we have the new configuration for cancer hallmarks.

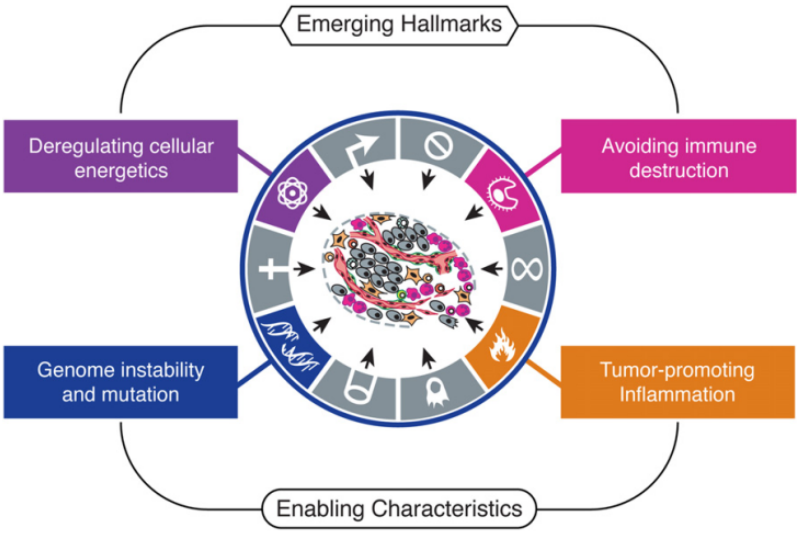

Figure 2.3 – Cancer hallmarks update - reproduced from Hanahan and Weinberg (2011).

2.1.3 Solid tumors

Solid tumors account for more than 85% of cancer mortality (Jain, 2005). Examples of solid tumors are sarcomas and carcinomas. The solid tumor carcinoma, developed by the unregulated multiplication of epithelial cells, is responsible for the most of those deaths. The epithelium is composed of sheets of tightly adhered epithelial cells that cover organ surfaces and often perform specialized functions. Epithelial tissue is not vascularized and the space between cells is minimal, leaving no space for the extracellular matrix (ECM). Epithelial cells feed through the diffusion of nutrients found in adjacent connective tissue, named the stroma, that is interlaced by blood vessels, nerves, and lymphatic vessels. It may rest on an additional layer of muscle or bone and is separated from the epithelial tissue by the basement membrane (Cristini and Lowengrub, 2010).

In the initial stage of the tumor, called the *avascular stage*, tumor cells feed on the nutrients available in the host tissue. Initially all cells are well-nourished and proliferate rapidly (Byrne and Preziosi, 2003) and, generally, the volume of a tumor does not exceed 1mm^3 at the avascular stage (Koumoutsakos et al., 2013). The growth of a spherical cluster of tumor cells prevents the nutrients from reaching the nucleus by diffusion, forming three regions: *proliferative layer*, *hypoxic layer* and *necrotic nucleus*. The proliferative layer is located in the most superficial part of the tumor and is in contact with the host tissue, therefore it has easier access to the available nutrients. The hypoxic layer is an intermediate layer, where the cells do not have access to the necessary amount of nutrients to proliferate, entering a state quiescent. The necrotic nucleus is composed by cells that die due to lack of nutrients. Figure 2.4 shows the aforementioned layers.

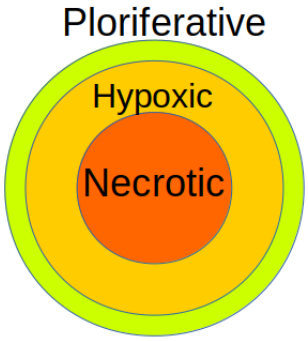

Figure 2.4 – Layers of a solid tumor in the avascular phase, based on nutrient distribution: Proliferative layer (Green), Hypoxic layer (Mustard) and Necrotic nucleus (Orange).

Another solid tumor structure is known as a tumor cord, which forms when a solid tumor grows around a blood vessel. This type of tumor has a particular sequence of layers, not following the configuration shown in Figure 2.4. Its cylindrical structure is shown in Figure 2.5, highlighting the scheme with the order of its layers.

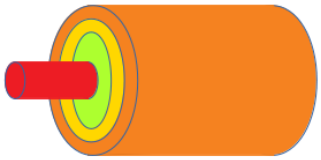

Figure 2.5 – Layers of a tumor cord based on nutrient distribution: Necrotic layer (Orange), Hypoxic layer (Mustard), Proliferative layer (Green) and in the center the vessel (red).

The proliferative layer is located in the region closest to the vessel, while the necrotic layer is located in the most distant region. The hypoxic layer occupies a transition region, between the proliferative and necrotic layer. Radial growth is limited by the low concentration of nutrients in the hypoxic and necrotic layers, so the radius of the cylindrical structure tends to become constant. In this configuration, longitudinal growth prevails.

These structures were studied by Moore et al. (1984), Bertuzzi and Gandolfi (2000), Scalerandi et al. (2003), Bertuzzi et al. (2004), Astanin and Tosin (2007) and others. Bertuzzi et al. (2002), for example, constructs a mathematical model that describes the steady state proliferative behavior of the cell population within a tumor cord.

Szymańska et al. (2018) presents simulations of a individual-based, force-based model of cell growth which is driven by forces acting upon the cell. Their tumor growth simulations focus on the description of the tumor cord. Tumor cells are placed around a small blood vessel that secretes nutrients. The concentration of nutrients is constant within the vessel and diffuses through the tissue, reaching zero at a distance of about 200μm. Figure 2.6 shows the result of one of its simulations.

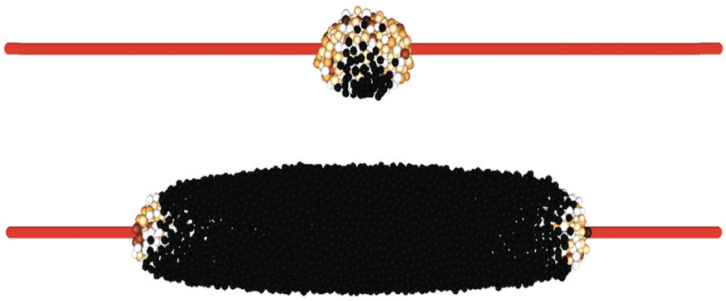

Figure 2.6 – Plots showing results of numerical simulations of Szymańska et al. (2018), where a growing tumor cord around a central blood vessel at times $332h$ and $1332h$. As the tumor cord grows, the cells further from the vessel become necrotic (black). – adapted from Szymańska et al. (2018).

A tumor growth model was presented by Astanin and Tosin (2007) to describe the behavior of the tumor cord. It is based on the theory of mixture and is composed of two partial differential equations. One equation governs the volume of tumor cells and the other, nutrients. The results show a constant layer of tumor cells around the vessel and a

constant velocity of expansion. For the other hand, Tosin (2009) performed experiments with an integro-differential free boundary model, being able to describe the evolution of the tumor cord and the concentration of nutrients. Figure 2.7 shows the two-dimensional domain of the experiment performed by Tosin (2009).

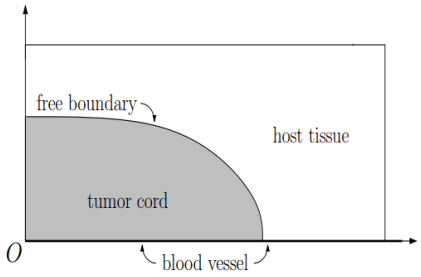

Figure 2.7 – A rectangular domain divided into two subregions, representing the tumor cord and host tissue, separated by a free boundary. The blood vessel coincides with the horizontal axis – adapted from Tosin (2009).

In one of his experiments, Tosin (2009) places a small tumor in the lower left part of the domain, next to the blood vessel. Figure 2.8 shows two stages of the experiment, where Fig. 2.8(a) represents time $t = 100$ and Fig. 2.8(b) represents time $t = 900$.

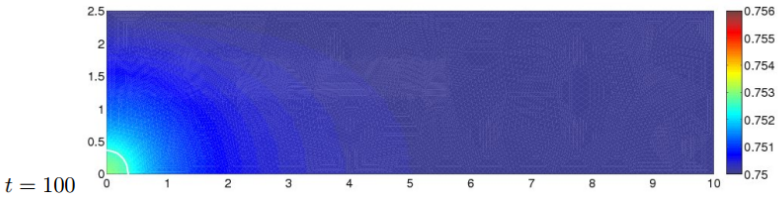

(a) Experiment setup at $t = 100$, tumor and nutrients.

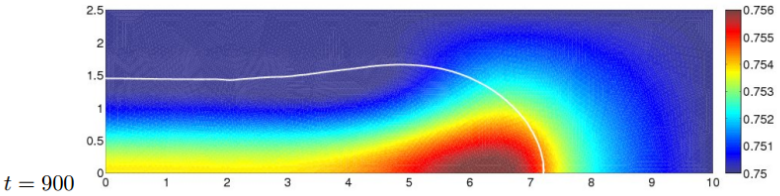

(b) Experiment setup at time $t = 900$.

Figure 2.8 – The white line indicates the position of the interface between tumor cells and host tissue. The concentration of nutrients is given by the variation of colors. Reproduced from (Tosin, 2009)

According to Harris (2002), 180μm is the calculated distance that oxygen diffuses as it passes from the capillary to the cells before it is completely metabolized. For this reason, in our experiments involving a tumor cord (section 6.5), the distance between the pre-existing vessel and the tumor is less than 180μm, thus allowing the arrival of nutrients from the capillary to feed the tumor.

2.1.4 Angiogenesis

Due to the privation of nutrients, hypoxic tumor cells produce angiogenic factors, capable of inducing *angiogenesis*, that can be defined as the process in which new blood vessels are formed from pre-existing ones through migration and proliferation mechanisms (Xu et al., 2016). The process of tumor angiogenesis was discovered in the 1970s by Folkman (1971). Tumor angiogenic factors (TAF) diffuse through the tumor and host tissue in search of blood vessels rich in nutrients. The blood vessels are lined with endothelial cells, that upon contact with angiogenic factors, obtain two different phenotypes: stalk and tip. Endothelial cells with the tip phenotype acquire filopodia, extensions capable of analyzing the surrounding environment and guiding the cell towards the tumor, following the gradient of angiogenic factor (Hellström et al., 2007; Suchting et al., 2007; Aird, 2012). Endothelial cells with the stalk phenotype proliferate creating a new capillary, maintaining the connection between the tip cell and the original vessel. A ligand for Notch receptors, called Delta-like 4 (Dll4), regulates the branching of vessels, inhibiting the formation of endothelial tip cells in response to TAF (Hellström et al., 2007; Suchting et al., 2007). Searching for an adequate ratio between the stalk and tip cells, required for correct sprouting and branching patterns(Hellström et al., 2007). Figure 2.9 shows a scheme growth of a new capillary from a pre-existing vessel.

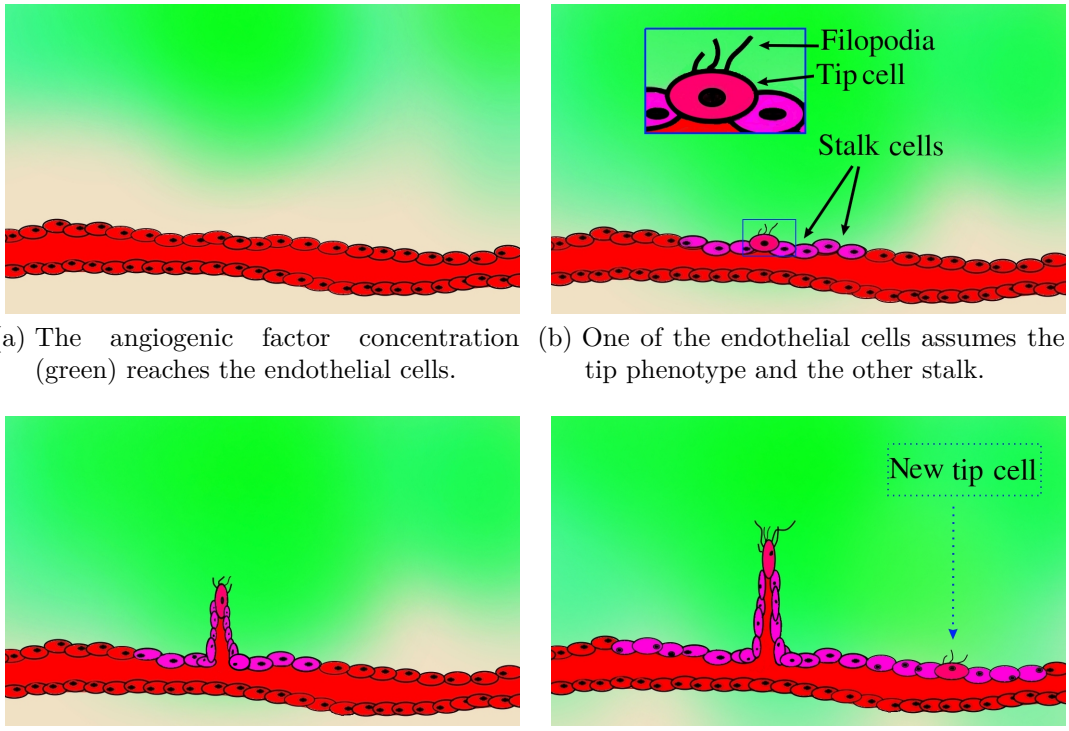

(a) The angiogenic factor concentration (green) reaches the endothelial cells.

(b) One of the endothelial cells assumes the tip phenotype and the other stalk.

(c) The tip cell moves toward the tumor and the stalk cells proliferate.

(d) The TAF reaches other endothelial cells and another tip cell is activated.

Figure 2.9 – Growth of new capillaries from pre-existing vessels.

When the new capillary, guided by the tip cell, reaches the tumor it provides nutrients for the tumor cells to proliferate. It takes approximately 10 to 21 days for the growing network to link the tumor to the parent vessel (Mantzaris et al., 2004), and the tumor growth enters in the vascular stage. The connection of the tumor to the blood vessels creates the opportunity for the tumor cells to fall into the bloodstream and migrate to other organs.

2.1.5 Mechanical response

The proliferation of the tumor cells and the increase of the tumor mass promotes the appearance of physical forces when the solid tumor growths in confined spaces *in vivo*. Knowing how these forces affect tumor development is one of the goals in biomechanical research on tumor growth. Koike et al. (2002) found that solid stress facilitates the formation of spheroids in rat prostate carcinoma cells, even though the tumor cells used are highly metastatic, which in the absence of stress would not have this morphology. The authors suggest that cell matrix adhesion is predominant. Those kind of cell may be adequate for spheroid formation, whereas solid stress may be required to form spheroids in the cell.

Stylianopoulos et al. (2012) studied the effect of externally applied stress on solid tumors. In the experiment the tumor cells were dipped in agarose gel with different levels of stiffness and it was observed that the increase of the compressive stress inhibits the growth of spheroids. Stylianopoulos et al. (2013) considers in his model, in the tumor environment, three types of stress: growth-induced stress, externally applied stress, and fluid pressure. The action of solid stress on a tumor is presented in (Stylianopoulos et al., 2013) by a scheme described in Figure 2.10. In the interior, the tumor is compressed while at the interface with the normal tissue the tumor is compressed in the radial direction and stretched in the circumferential. Stylianopoulos et al. (2013) states that, as a result of these stresses, peritumoral vessels might form elliptical rather than circular shapes.

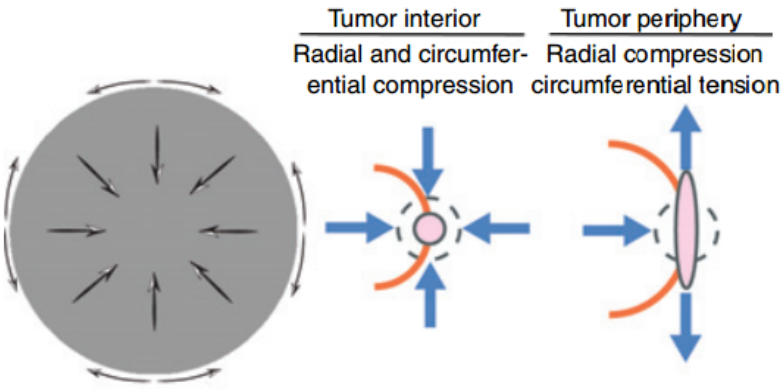

Figure 2.10 – Action of solid stress on a tumor – adapted from Stylianopoulos et al. (2013).

Mechanical forces applied to the solids cause deformation and the forces applied to the liquids cause flow (Fung, 1977), but when mechanical forces act on biological tissues they can induce biological responses to those stimuli in the cells. According to Zhu et al. (2002), there is an increasing evidence that many conditions of cells, normal and diseased, are dependent on or regulated by their mechanical environment. The evidence that proliferating tumor cells cause compression and collapse of intratumoral vessels are shown in Padera et al. (2004). The compression in the vessels makes the arrival of nutrients to the tumor be difficult, resulting in the inhibition of tumor growth. The decreasing of the nutrient supply to the tumor can turn proliferative tumor cells into hypoxic cells. According to Jain et al. (2014), hypoperfusion and hypoxia contribute to immune evasion, promote malignant progression and metastasis, and also reduce the efficacy of a number of therapies, including radiation.

Nia et al. (2017) used the planar-cut method, which provides 2D maps of solid stress in tumors, to estimate and compare the solid stress, elastic energy and mechanical stiffness in size-matched tumors formed from the same cell lines, and in primary versus metastatic sites. With this experiment they discovered three important relationships between these physical quantities, the type of cell and also the location of the tumor:

(i) solid stress and elastic energy are mechanical abnormalities that vary between tumors;

(ii) solid stress and elastic energy depend on both the cancer-cell type and the microenvironment in which they reside;

(iii) tumors with greater elastic energy are not necessarily stiffer, and stiffer tumors do not necessarily have greater elastic energy.

According to Taber (2004), problems involving deformation of soft biological tissues are among the most challenging in applied mechanics. The continuum mechanics is a powerful tool and provides a strong theoretical basis to model the physical phenomena that act in the tumor environment. A brief review of the main concepts used in this work is presented in the next section.

2.2 Fundamental laws of physics

The fundamental laws of physics were developed over centuries by observations and experiments, always accompanied by a rigorous mathematical description. These laws are fundamental to describe mathematical models for complex phenomena that occur in several areas of knowledge. The scope of these laws also covers the biological area, the subject of this work.

The continuum mechanics considers the laws of physics to study deformations and forces acting on a body which can be solid, liquid or gas. To apply mathematical concepts to these bodies, the continuum hypothesis is applied, disregarding the discrete nature of matter - that is, the spaces between the molecules that form bodies are neglected - and the body is considered a continuous medium. With this, it is possible to define quantities, represented by continuous functions such as mass density, displacement, velocity and deformation (Reddy, 2013).

The references used in the composition of this section are the works of Gonzalez and Stuartt (2008), Gurtin et al. (2010), Epstein (2012), Reddy (2013).

2.2.1 Motion

The motion of a body $\boldsymbol{B} \subset \mathbb{R}^3$ is given by a smooth function φ, which at each point $\boldsymbol{X} \in \boldsymbol{B}$ and a time $t \in [0, T]$, is associated with a point $\boldsymbol{x} \in \mathbb{R}^3$,

$$\varphi(\boldsymbol{X}, t) = \boldsymbol{x}. \tag{2.1}$$

By fixing the time t, the function

$$\varphi_t(\boldsymbol{X}) = \varphi(\boldsymbol{X}, t) \tag{2.2}$$

will be called the deformation function of body $\boldsymbol{B}$. In this way the function φ is considered a continuous deformation of the body $\boldsymbol{B}$. We use the notation $\boldsymbol{B}_t$ to represent the image of the deformation, $\boldsymbol{B}_t = \varphi_t(\boldsymbol{B})$. For $t = 0$ we consider the function $\varphi_0(\boldsymbol{X}) = \boldsymbol{X}$, so $\varphi_0(\boldsymbol{B}) = \boldsymbol{B}_0 = \boldsymbol{B}$.

The domain $\boldsymbol{B}$ and the image $\boldsymbol{B}_t$ are called the reference body (material) and the deformed (spatial) body, respectively. The configuration of the body $\boldsymbol{B}$ is called material configuration and the elements associated with it - such as points, vectors, derivatives and others - are called material elements. Similarly, the configuration and elements associated with body $\boldsymbol{B}_t$ are called spatial configuration and spatial elements. A representation of a function φ and some material and spatial elements are shown in Figure 2.11.

Let β be a scalar, vector or tensor field, and γ be a vector or tensor field. We consider the symbols GRAD(β) and DIV(γ) to represent the gradient and divergence of the field in the reference configuration. Similarly, the symbols $\nabla\beta$ and $\nabla \cdot \gamma$ represent the gradient and the divergence of the field in the spatial configuration.

The local deformation of a body can be represented by the gradient of the function φ_t

$$\frac{\partial \varphi_t(\boldsymbol{X})}{\partial \boldsymbol{X}} = \frac{\partial \boldsymbol{x}}{\partial \boldsymbol{X}} = GRAD(\varphi) = \mathbf{F} \ . \tag{2.3}$$

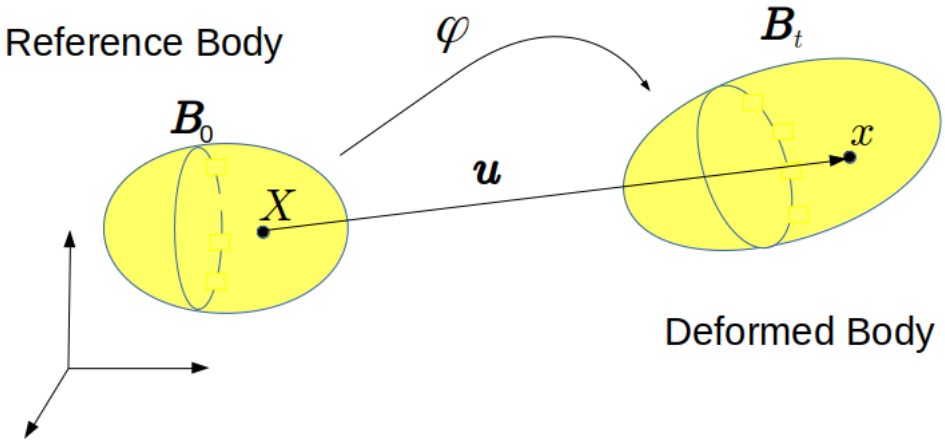

Figure 2.11 – Function φ, the displacement vector $\boldsymbol{u}$, the reference body $\boldsymbol{B}_0$ and deformed body $\boldsymbol{B}_t$.

The *deformation gradient* $\mathbf{F}$ is a second-order tensor defined by

$$\mathbf{F} = \left[\frac{\partial \boldsymbol{x}_i}{\partial X_j}\right] = \begin{bmatrix} \frac{\partial \boldsymbol{x}_1}{\partial X_1} & \frac{\partial \boldsymbol{x}_1}{\partial X_2} & \frac{\partial \boldsymbol{x}_1}{\partial X_3} \\ \frac{\partial \boldsymbol{x}_2}{\partial X_1} & \frac{\partial \boldsymbol{x}_2}{\partial X_2} & \frac{\partial \boldsymbol{x}_2}{\partial X_3} \\ \frac{\partial \boldsymbol{x}_3}{\partial X_1} & \frac{\partial \boldsymbol{x}_3}{\partial X_2} & \frac{\partial \boldsymbol{x}_3}{\partial X_3} \end{bmatrix}. \tag{2.4}$$

In general, the tensor $\mathbf{F}$ is not symmetrical and its determinant J is called the *Jacobian of motion*. If $J = 1$ for all points of the body, the deformation preserves the volume of the body and is called *isochoric*. A fundamental hypothesis for the study of the movement of a body is to demand that the determinant of the deformation gradient be non-zero ($J \neq 0$). A physical reason for assuming this hypothesis is to prevent the density from taking on unwanted values, such as zero in the initial configuration. Here we impose $J > 0$, thus ensuring that the deformation will preserve the orientation of the body (Gonzalez and Stuartt, 2008).

Considering φ_t invertible and of class $C^k(\boldsymbol{B})$, the hypothesis $J > 0$ guarantees that φ_t^{-1} is also class $C^k(\boldsymbol{B})$. Bowen (1976) suggests assuming sufficient smoothness of φ_t so as to make any needed mathematical operations correct. Here we consider $k = 2$, as in Ogden (1984).

$$\varphi_t(\boldsymbol{X}) = \boldsymbol{x} \qquad \varphi_t^{-1}(\boldsymbol{x}) = \boldsymbol{X}. \tag{2.5}$$

The *velocity* of the particle at time t is given by

$$\mathbf{V}(\boldsymbol{X}, t) = \frac{\partial \varphi(\boldsymbol{X}, t)}{\partial t} = \frac{\partial \varphi(\varphi^{-1}(\boldsymbol{x}), t)}{\partial t} = \mathbf{v}(\boldsymbol{x}, t). \tag{2.6}$$

The *material time derivative* of a scalar field β is given by

$$\frac{d\beta}{dt} = \frac{\partial \beta}{\partial t} + \mathbf{v} \cdot \nabla \beta, \tag{2.7}$$

where $\mathbf{v}$ is the velocity of the particle at time t.

The following theorem was introduced due to its importance in the multiplicative decomposition of tensors and its use in the creation of fundamental tensors to study deformation.

Theorem 1. *(Polar Decomposition) Let* $\mathbf{F}$ *be an invertible tensor* ($J = det(\mathbf{F}) \neq 0$). *Then, there are symmetric, positive-definite tensors* $\mathbf{U}$ *and* $\mathbf{V}$ *and a rotation* $\mathbf{R}$ *such that*

$$\mathbf{F} = \mathbf{RU} = \mathbf{VR},$$

where $\mathbf{U} = \sqrt{\mathbf{F}^T\mathbf{F}}$ *and* $\mathbf{V} = \sqrt{\mathbf{F}\mathbf{F}^T}$.

For a better analysis of the changes in the geometry of a body, tensor $\mathbf{F}$ can help to define, respectively, the *right* and *left Cauchy-green strain tensors* as:

$$\mathbf{C} = \mathbf{F}^T\mathbf{F} = \mathbf{U}^2, \tag{2.8}$$

$$\mathbf{B} = \mathbf{F}\mathbf{F}^T = \mathbf{V}^2, \tag{2.9}$$

where it is taking into account only the variations in the distances and neglecting rotations and translations. The tensors $\mathbf{C}$ and $\mathbf{B}$ are symmetric positive definite.

The *displacement* $\boldsymbol{u}$ of a body's particle is given by the difference between its initial position $\boldsymbol{X}$ and its final position $\boldsymbol{x}$,

$$\boldsymbol{u}(\boldsymbol{x}) = \boldsymbol{x} - \varphi^{-1}(\boldsymbol{x}, t) = \boldsymbol{x} - \boldsymbol{X}. \tag{2.10}$$

Figure 2.11 shows the representation of the displacement $\boldsymbol{u} \in \mathbb{R}^3$. The deformation and displacement in one dimension can be seen in Fig. 2.12.

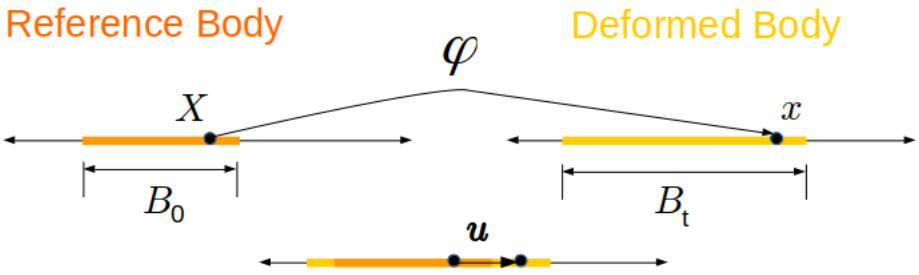

Figure 2.12 – Deformation function φ_t, reference body $\boldsymbol{B}_0$, deformed body $\boldsymbol{B}_t$, displacement $\boldsymbol{u}$.

In the context of tumor growth, both tumor and host tissue coexist with mechanical forces acting on them. Moreover, they themselves exert forces on all components of the environment. The development, the shape and even the malignancy of tumors are influenced by those mechanical forces.

In general, there are two types of forces in the mechanics of the continuum: *surface forces* and *body forces*. Surface forces act on the body surface and are calculated per unit of surface area through which they act – they are called contact forces. Body forces act at a distance, without physical contact between bodies, such as gravity. Those forces act on the volume or mass elements in the body.

When a force $\mathbf{f}$ is applied on a deformable body $\boldsymbol{B}$ it is expected that the force does not act at all points of $\boldsymbol{B}$ with the same intensity and direction. Given a point $x \in \boldsymbol{B}_t$, take a plane s that passes through x, and the normal vector $\boldsymbol{n}$ that determines it. Take in s, an element of area Δs with center x. The result of the internal force acting on this element of area Δs is represented by the vector $\Delta \boldsymbol{f}$.

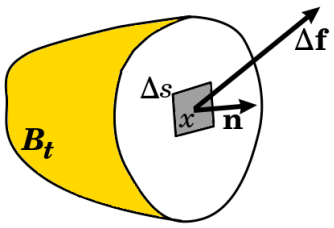

Figure 2.13 – Surface force $\Delta \boldsymbol{f}$ on surface area element Δs at point x.

The traction vector, defined as

$$\mathbf{t}(\boldsymbol{x}, t, \mathbf{n}) = \lim_{\Delta s \to 0} \frac{\Delta \mathbf{f}}{\Delta s} \tag{2.11}$$

gives an idea of how the surface force $\mathbf{f}$ acts on the body and it depends on the point $\boldsymbol{x}$ and the vector $\mathbf{n}$, normal to the element of area Δs.

The traction vector appears in the integral form of the momentum balance on a surface integral. Transforming the integral form to a local form requires that all integrals be volume integrals and the shape of the traction vector makes it difficult to use the divergence theorem for such a change (Goriely, 2017). An alternative is to write the traction vector as a result of applying a tensor over the normal vector. Cauchy principles can be used to show that the surface force density depends linearly on the normal unit vector (Ogden, 1984), when $\mathbf{t}$ is continuously differentiable. This means that

$$\mathbf{t}(\boldsymbol{x}, t, \boldsymbol{n}) = \mathbf{T}(\boldsymbol{x}, t)\mathbf{n}(\boldsymbol{x}) \ , \tag{2.12}$$

where $\mathbf{T}$ is a second order tensor, called *Cauchy stress tensor* and is one of the main stress measures. The Cauchy stress tensor is defined in current configuration as the tensor that maps $\mathbf{n}$ in $\mathbf{t}$, according to (2.12). Figure 2.14 shows the Cauchy tensor acting on vector $\mathbf{n}$, which is unitary and normal to surface R_t at point x.

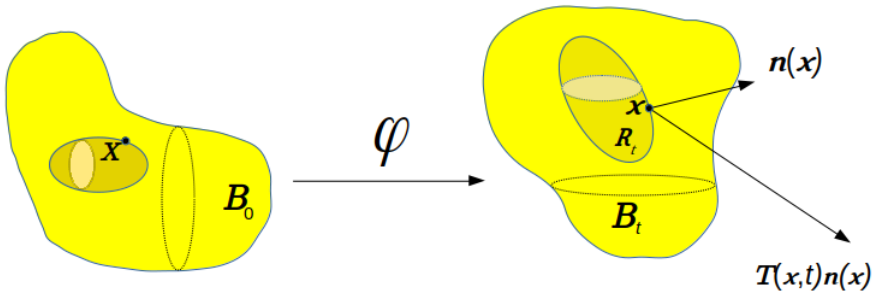

Figure 2.14 – The Cauchy tensor acts on the vector $\mathbf{n}$, which is unitary and normal to the surface R_t at point x.

2.2.2 Balance laws

The balance laws are physical principles that must be satisfied for all materials systems. The form of each balance law depends on the fields and the forces that are considered in the model. A thermo-mechanical system must include the following balance laws:

- balance of mass;
- balance of linear momentum;
- balance of angular momentum;
- balance of energy;
- the second law of thermodynamics.

From that moment on we consider $\varphi : \boldsymbol{B} \times [0, \infty) \longrightarrow \mathbb{R}^3$ the motion of a continuous body $\boldsymbol{B}$, with an associated spatial velocity field $\mathbf{v}(\boldsymbol{x}, t)$ and a spatial mass density field $\rho(\boldsymbol{x}, t)$.

Balance of mass

This law states that mass is neither created nor destroyed in a closed system, so it can also be called the mass conservation principle. The mass balance in the Eulerian configuration can be written as

$$\frac{\partial \rho}{\partial t} + \nabla \cdot (\rho \mathbf{v}) = 0, \tag{2.13}$$

for all $\boldsymbol{x} \in \boldsymbol{B}$ and $t \geqslant 0$. Considering the material time derivative definition, Eq. (2.13) can be written as

$$\frac{\partial \rho}{\partial t} + \mathbf{v} \cdot \nabla \rho + \rho \nabla \cdot \mathbf{v} = 0 \tag{2.14}$$

$$\frac{d\rho}{dt} + \rho \nabla \cdot \mathbf{v} = 0. \tag{2.15}$$

Balance of linear momentum

This law is equivalent to Newton's second law of motion applied to a deformable continuum and relates forces acting on a body with its acceleration. We consider here two types of forces: macroscopic and microscopic.

The *balance of linear momentum for macroscopic forces* in the Eulerian configuration can be described as

$$\rho\frac{\partial \mathbf{v}}{\partial t} + \rho(\nabla \mathbf{v})\mathbf{v} = \nabla \cdot \mathbf{T} + \rho\mathbf{b}, \tag{2.16}$$

or, considering the material time derivative definition,

$$\rho\frac{d\mathbf{v}}{dt} = \nabla \cdot \mathbf{T} + \rho\mathbf{b}, \tag{2.17}$$

for all $\boldsymbol{x} \in \boldsymbol{B}$ and $t \geqslant 0$, where $\mathbf{T}(\boldsymbol{x}, t)$ is the Cauchy stress field and $\mathbf{b}(\boldsymbol{x}, t)$ is the body force. A new version for Eq. (2.16) can be found by multiplying Eq. (2.14) by $\mathbf{v}$ and adding Eq. (2.16) as follows

$$\begin{aligned}
\rho\frac{\partial \mathbf{v}}{\partial t} + \rho(\nabla \mathbf{v})\mathbf{v} + \frac{\partial \rho}{\partial t}\mathbf{v} + (\mathbf{v}\cdot\nabla\rho)\mathbf{v} + (\rho\nabla\cdot\mathbf{v})\mathbf{v} &= \nabla\cdot\mathbf{T} + \rho\mathbf{b} \\
\frac{\partial(\rho\mathbf{v})}{\partial t} + \rho(\nabla \mathbf{v})\mathbf{v} + (\mathbf{v}\cdot\nabla\rho)\mathbf{v} + (\rho\nabla\cdot\mathbf{v})\mathbf{v} &= \nabla\cdot\mathbf{T} + \rho\mathbf{b} \\
\frac{\partial(\rho\mathbf{v})}{\partial t} + \rho\left[\mathbf{v}\cdot(\nabla\mathbf{v}) + (\nabla\cdot\mathbf{v})\mathbf{v}\right] + (\mathbf{v}\cdot\nabla\rho)\mathbf{v} &= \nabla\cdot\mathbf{T} + \rho\mathbf{b} \\
\frac{\partial(\rho\mathbf{v})}{\partial t} + \rho\left[\nabla\cdot(\mathbf{v}\otimes\mathbf{v})\right] + (\mathbf{v}\otimes\mathbf{v})\nabla\rho &= \nabla\cdot\mathbf{T} + \rho\mathbf{b} \\
\frac{\partial(\rho\mathbf{v})}{\partial t} + \nabla\cdot(\rho\mathbf{v}\otimes\mathbf{v}) &= \nabla\cdot\mathbf{T} + \rho\mathbf{b}.
\end{aligned} \tag{2.18}$$

The microforces describe forces associated with microscopic configurations of atoms. Gurtin (1996) justifies a separate micro-balance as a consequence of the large difference in the scales involved. The microforce system consists of a vector stress $\boldsymbol{\xi}$, an internal scalar force π and an external scalar force τ. The *microforce balance* is given by

$$\nabla\cdot\boldsymbol{\xi} + \pi + \tau = 0. \tag{2.19}$$

Balance of angular momentum

This law, when applied in nonpolar materials, is greatly simplified and is represented by

$$\mathbf{T} = \mathbf{T}^T\ . \tag{2.20}$$

Thus, the conservation of angular momentum reduces to the assertion that the Cauchy tensor is symmetric.

Balance of energy

The energy stored in a body $\boldsymbol{B}_t$ is represented by the internal energy $\varepsilon(\mathbf{x}, t)$. Contributions to internal energy can occur in various ways, for example by heating the body $\boldsymbol{B}_t$

or by the mechanical work applied on it. The release of internal energy can also occur in several ways such as: heat, movement or mechanical work. The internal energy can be composed, for example, by mechanical, thermal, chemical or electromagnetic contributions. Considering only the mechanical and thermal energies, the energy balance equation can be written as

$$\rho\frac{d\varepsilon}{dt} = \mathbf{T} : \mathbf{D} - \nabla \cdot \mathbf{q} + \rho r \qquad \forall \mathbf{x} \in \boldsymbol{B}_t,\ t \geqslant 0, \tag{2.21}$$

where $\mathbf{D}$ is the symmetric part of $\nabla\mathbf{v}$, $\mathbf{q}(\mathbf{x}, t)$ is the heat flux vector field, $r(\mathbf{x}, t)$ is the heat supply field per unit mass. Equation (2.21) is known as the *first law of thermodynamics*. A new version of this equation can be formulated taking into account the chemical energy and work done by the microforces.

Second law of thermodynamics

One form of the second law of thermodynamics is given by the inequality of *Clausius–Duhem*

$$\rho\frac{d\eta}{dt} \geqslant \frac{\rho r}{\theta} - \nabla \cdot \left(\frac{\mathbf{q}}{\theta}\right) \qquad \forall \mathbf{x} \in \boldsymbol{B}_t,\ t \geqslant 0, \tag{2.22}$$

where $\eta(\mathbf{x}, t)$ is the entropy field per unit mass (Gurtin, 1996) and $\theta(\mathbf{x}, t)$ is the (absolute) temperature field in $\boldsymbol{B}_t$.

For details on continuum mechanics and laws of equilibrium, Gonzalez and Stuartt (2008) and Truesdell (1992) are good references. For a biological view of continuum mechanics, Fung (1977) is a good recommendation.

2.3 Mixture theory

When a body is formed by the mixture of two or more constituents, its individual physical properties may influence movement and deformation, as well as the possibility of chemical interaction between constituents. There are two types of mixture: homogeneous and heterogeneous (Concha, 2014). A homogeneous mixture occurs at the molecular level, whereas a heterogeneous mixture occurs at the macroscopic level and is called a multiphase mixture. The components of a multiphase mixture can be identified at different phases.

The theory of continuous mixture was developed for the study of bodies with multiple constituents. The initial ideas for mixture theory are credited to Fick (1855) and Darcy (1856). However, Truesdell (1957) stands out in the development of this theory. Truesdell presented a unified treatment of the mass, momentum and energy balance equations and discussed possible forms for the second axiom of thermodynamics (Bowen, 1976).

The constituents present in the mixture coexist, that is, each constituent is dense in the mixture. Thus, for each point of the space occupied by the mixture, there are particles belonging to each of the constituents. The mixture can be seen as a superposition of continuous media, where each one follows its own movement with the restriction imposed

by the interaction between the components (Concha, 2014). The mixture, when treated as a body composed of a single component, must obey the physical laws imposed on the bodies.

The study of phases evolution in a mixture and the transition between them requires the demarcation of the position occupied by each phase, determined by the interface. There are two main phase evolution models: sharp interface and diffuse interface. In sharp interface models the phase shift is abrupt. In the diffuse interface model changes between phases take place quickly but smoothly. Figure 2.15 shows a two phase model configuration where dotted line describes the phase transition for sharp interface and diffuse interface. A diffuse interface has non-zero thickness, i.e. there is a transition region between one phase to another. When using a sharp interface approach, it is necessary to track interfaces during evolution by tracking the position of interfaces through mathematical equations (Moelans et al., 2008).

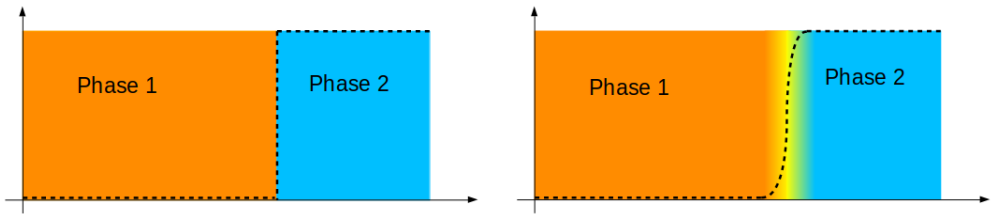

(a) Sharp interface. (b) Difuse interface.

Figure 2.15 – Two phase model configuration.

In the diffuse interface approach, the microstructure is represented by means of a set of phase-field variables that are continuous functions of space and time. The temporal evolution of the phase-field variables is described by a set of partial differential equations (Moelans et al., 2008).

Biological growth can be modeled as a continuous and homogeneous solid domain composed of a single constituent. This approach may ignore phenomena that play important biological roles during growth, including reaction and transport of nutrients, enzymes, and by-products. Thus, the formulation of a model for biological growth will be enriched using the mixture theory, which may include contributions from various constituents, solid or liquid, as well as growth factors and cytokines, nutrients and interstitial fluid waste products, all involved in the biochemical and biophysical process of growth (Ambrosi et al., 2011).

Continuous models of tumor growth based on mixture theory have already been described by a set of important references, such as Byrne (2003), Cristini et al. (2009), Oden et al. (2010), and Lima et al. (2014). Those models often use mass balance equations to describe their solid components (such as vessels, tumor tissue, healthy tissue), reaction-

diffusion equations for fluid components (such as nutrients and agiogenic factors) and source terms to perform coupling between equations. The choices made to describe the velocities of these components characterize two main classes of macroscopic models: *phenomenological models* and *mechanical models*.

Phenomenological models are very important and widely used in tumor modeling and, in general, they make an assumption about movement of cells (or matrix components), ignoring many mechanical effects. On the other hand, mechanical models use force-balance or momentum balance interactions to determine the movements of the components in response to the physical forces involved (Bellomo et al., 2008). According to ODEN et al. (2013), there is increasing evidence that many of the complex processes involved in the growth of tumors can be captured by phenomenological models, and by careful characterizations of mechanical, chemical, and thermodynamical properties of tissue.

From now on, our main references will be Bowen (1976), Rajagopal and Tao (1995), and Oden et al. (2010). Generalizing the idea of movement and deformation for the theory of mixture, we consider that there are N constituents in the mixture and X_α, $\alpha = 1, 2, ..., N$, is the position of a particle of the α constituent in its reference configuration. For each constituent α, there is a function of the motion, defined by

$$\varphi_\alpha(\boldsymbol{X}_\alpha, t) = \boldsymbol{x}. \tag{2.23}$$

The deformation gradient of each constituent is given by

$$\mathbf{F}_\alpha = \frac{\partial \varphi_\alpha}{\partial \boldsymbol{X}_\alpha}. \tag{2.24}$$

To know the contribution of each constituent in the volume of the mixture at point $\boldsymbol{x}$, the *volume fraction* is defined as

$$\phi_\alpha(\boldsymbol{x}, t) = \frac{\partial v_\alpha}{\partial v}, \tag{2.25}$$

where ∂v is a differential volume containing the point $\boldsymbol{x}$, and ∂v_α is the proportion of volume occupied by the constituent α. The mixture is considered *saturated*, when the sum of the volume fractions of the constituents is equal to 1, i.e.,

$$\sum_{\alpha=1}^{N} \phi_\alpha(\boldsymbol{x}, t) = 1. \tag{2.26}$$

The *mass density* of the mixture, ρ, is given by the sum of the mass densities of each constituent $\hat{\rho}_\alpha$

$$\rho(\boldsymbol{x}, t) = \sum_{\alpha=1}^{N} \hat{\rho}_\alpha(\boldsymbol{x}, t), \tag{2.27}$$

where

$$\hat{\rho}_\alpha(\boldsymbol{x}, t) = \rho_\alpha(\boldsymbol{x}, t)\phi_\alpha(\boldsymbol{x}, t), \tag{2.28}$$

and ρ_α represent the mass of the α-constituent per unit volume of the constituent. The *mass concentration* of the α-constituent is defined by

$$c_\alpha(\boldsymbol{x}, t) = \frac{\hat{\rho}_\alpha(\boldsymbol{x}, t)}{\rho(\boldsymbol{x}, t)}. \tag{2.29}$$

The *velocity* of a particle of the α-constituent at time t is given by

$$\mathbf{v}_\alpha(\boldsymbol{x}, t) = \frac{\partial \varphi(\boldsymbol{X}_\alpha(\boldsymbol{x}, t), t)}{\partial t}, \tag{2.30}$$

and the *velocity gradient* of each constituent will be represented by

$$\mathbf{L}_\alpha = \nabla \mathbf{v}_\alpha(\boldsymbol{x}, t). \tag{2.31}$$

The *mean velocity of the mixture* can be calculated as follows,

$$\mathbf{v} = \frac{1}{\rho} \sum_{\alpha=1}^{N} \rho_\alpha \phi_\alpha \mathbf{v}_\alpha. \tag{2.32}$$

The velocity of the α-constituent in relation to the mean velocity of the mixture is called the *diffusion velocity* and is defined by

$$\mathbf{u}_\alpha = \mathbf{v}_\alpha - \mathbf{v}. \tag{2.33}$$

The tensor $\mathbf{L}_\alpha$ can be decomposed as a sum of a symmetrical part $\mathbf{D}_\alpha$ and an antisymmetric part $\mathbf{W}_\alpha$, where

$$\mathbf{D}_\alpha = \frac{1}{2}[\mathbf{L}_\alpha + \mathbf{L}_\alpha^T], \tag{2.34}$$

$$\mathbf{W}_\alpha = \frac{1}{2}[\mathbf{L}_\alpha - \mathbf{L}_\alpha^T]. \tag{2.35}$$

The material-time derivative relative to the αth constituent of a scalar field β is given by the relation

$$\frac{d^\alpha \beta}{dt} = \frac{\partial \beta}{\partial t} + \mathbf{v}_\alpha \cdot \nabla \beta. \tag{2.36}$$

A relation between the material-time derivative (2.7) and (2.36) is given by the following expression,

$$\frac{d\beta}{dt} = \frac{d^\alpha \beta}{dt} - \mathbf{u}_\alpha \cdot \nabla \beta. \tag{2.37}$$

Proof In fact,

$$\begin{aligned}
\frac{d\beta}{dt} &= \frac{\partial \beta}{\partial t} + \mathbf{v} \cdot \nabla \beta \\
&= \frac{\partial \beta}{\partial t} + (\mathbf{v}_\alpha - \mathbf{u}_\alpha) \cdot \nabla \beta \\
&= \left(\frac{\partial \beta}{\partial t} + \mathbf{v}_\alpha \cdot \nabla \beta \right) - \mathbf{u}_\alpha \cdot \nabla \beta \\
&= \frac{d^\alpha \beta}{dt} - \mathbf{u}_\alpha \cdot \nabla \beta.
\end{aligned}$$

2.4 The balance laws for mixtures

Let us consider a mixture with N constituents, where each of them must obey the specific balance laws, formulated with the incorporation of terms that represent the interaction between the components of the mixture. Our main references for this section are: Bowen (1976), Rajagopal and Tao (1995), Gurtin (1996), Oden et al. (2010), Faghihi et al. (2018). We will use the notation ϕ_α to represent the volume fraction of the α-th constituent, that is the contribution of the constituent to the volume of the mixture at the point $\boldsymbol{x}$, that is $\phi_\alpha(\boldsymbol{x}, t) = \dfrac{\partial v_\alpha}{\partial v}$.

2.4.1 Mass balance

The mass balance of the species composing the mixture takes into account the mass exchange between the species. Thus, the mass balance of the species in the Eulerian configuration is given by

$$\boxed{\frac{\partial \rho_\alpha \phi_\alpha}{\partial t} + \nabla \cdot (\rho_\alpha \phi_\alpha \mathbf{v}_\alpha) = S_\alpha - \nabla \cdot \mathbf{J}_\alpha,} \tag{2.38}$$

where S_α is the mass supplied to constituent α by other constituents and $\mathbf{J}_\alpha$ is the mass flux due to changes in the chemical potential (Oden et al., 2010). Another way to write the equation (2.38) is

$$\frac{\partial \rho_\alpha \phi_\alpha}{\partial t} + \mathbf{v}_\alpha \cdot \nabla(\rho_\alpha \phi_\alpha) + \rho_\alpha \phi_\alpha \nabla \cdot \mathbf{v}_\alpha = S_\alpha - \nabla \cdot \mathbf{J}_\alpha \ , \tag{2.39}$$

$$\frac{d^\alpha \rho_\alpha \phi_\alpha}{dt} = S_\alpha - \nabla \cdot \mathbf{J}_\alpha - \rho_\alpha \phi_\alpha \nabla \cdot \mathbf{v}_\alpha \ . \tag{2.40}$$

The sum of all species represented by Eq. (2.38) yields an equation of conservation of mass equivalent to Eq. (2.13), where only one constituent is considered,

$$\sum_\alpha \left[\frac{\partial \rho_\alpha \phi_\alpha}{\partial t} + \nabla \cdot (\rho_\alpha \phi_\alpha \mathbf{v}_\alpha) \right] = \sum_\alpha \left[S_\alpha - \nabla \cdot \mathbf{J}_\alpha \right]. \tag{2.41}$$

Therefore

$$\sum_\alpha \left[S_\alpha - \nabla \cdot \mathbf{J}_\alpha \right] = 0, \tag{2.42}$$

and

$$\frac{\partial \left(\sum_\alpha \rho_\alpha \phi_\alpha \right)}{\partial t} + \nabla \cdot \left(\sum_\alpha \rho_\alpha \phi_\alpha \mathbf{v}_\alpha \right) = 0 \ . \tag{2.43}$$

Taking into account Eqs. (2.27), (2.28) and (2.32) on Eq.(2.43) we get

$$\frac{\partial \rho}{\partial t} + \nabla \cdot (\rho \mathbf{v}) = 0 \ . \tag{2.44}$$

Using the mass concentration c_α, given by Eq. (2.29), the mass balance is also described, in terms of c_α, as

$$\rho\frac{dc_\alpha}{dt} + \nabla\cdot(\rho_\alpha\phi_\alpha\mathbf{u}_\alpha) = S_\alpha - \nabla\cdot\mathbf{J}_\alpha, \tag{2.45}$$

remembering that $\mathbf{u}_\alpha = \mathbf{v}_\alpha - \mathbf{v}$ is the diffusion velocity of the α-component.

The Eq. (2.45) shows that when diffusion and chemical reactions are absent, the concentrations are constant (Bowen, 1976). An application of Eq.(2.45) occurs when a property Θ of the mixture is described as a weighted sum of the same property Θ_α of each constituent

$$\Theta = \frac{1}{\rho}\sum_\alpha \rho_\alpha\phi_\alpha\Theta_\alpha \ . \tag{2.46}$$

Eqs. (2.45) and (2.46) give us an identity that is of fundamental importance in mixture theory, according to Bowen (1976) ,

$$\rho\frac{d\Theta}{dt} = \sum\left[\rho_\alpha\phi_\alpha\frac{d^\alpha\Theta_\alpha}{dt} - \nabla\cdot(\rho_\alpha\phi_\alpha\Theta_\alpha\mathbf{u}_\alpha) + \Theta_\alpha\left(S_\alpha - \nabla\cdot\mathbf{J}_\alpha\right)\right] \ . \tag{2.47}$$

A similar identity to Eq. (2.47) can be described to relate $\mathbf{v}$ and $\mathbf{v}_\alpha$

$$\rho\frac{d\mathbf{v}}{dt} = \sum\left[\rho_\alpha\phi_\alpha\frac{d^\alpha\mathbf{v}_\alpha}{dt} - \nabla\cdot(\rho_\alpha\phi_\alpha\mathbf{v}_\alpha\otimes\mathbf{u}_\alpha) + \mathbf{v}_\alpha\left(S_\alpha - \nabla\cdot\mathbf{J}_\alpha\right)\right], \tag{2.48}$$

and replacing $\mathbf{v}_\alpha$ for $\mathbf{u}_\alpha + \mathbf{v}$ in the last two terms of the second member, we can rewrite Eq.(2.48) as

$$\rho\frac{d\mathbf{v}}{dt} = \sum\left[\rho_\alpha\phi_\alpha\frac{d^\alpha\mathbf{v}_\alpha}{dt} - \nabla\cdot(\rho_\alpha\phi_\alpha\mathbf{u}_\alpha\otimes\mathbf{u}_\alpha) + \mathbf{u}_\alpha\left(S_\alpha - \nabla\cdot\mathbf{J}_\alpha\right)\right]. \tag{2.49}$$

The proof of Eqs.(2.48) and (2.49) are shown, respectively, in Appendix A.3 and A.4.

2.4.2 Force balance

We have seen in Section (2.2.2) that macroscopic and microscopic forces involved in a thermomechanical system must satisfy laws described in Eqs. (2.16) and (2.19). By working with a body made up of N constituents, the forces associated with that body also must respect those laws and partial forces, associated with each of the constituents, are used to describe versions them.

The *balance of macroscopic forces* for the α-constituent will be

$$\boxed{\rho_\alpha\phi_\alpha\frac{\partial\mathbf{v}_\alpha}{\partial t} + \rho_\alpha\phi_\alpha\nabla(\mathbf{v}_\alpha)\mathbf{v}_\alpha = \nabla\cdot\mathbf{T}_\alpha + \rho_\alpha\phi_\alpha\mathbf{b}_\alpha + \hat{\mathbf{p}}_\alpha,} \tag{2.50}$$

or, equivalently,

$$\rho_\alpha\phi_\alpha\frac{d^\alpha\mathbf{v}_\alpha}{dt} = \nabla\cdot\mathbf{T}_\alpha + \rho_\alpha\phi_\alpha\mathbf{b}_\alpha + \hat{\mathbf{p}}_\alpha, \tag{2.51}$$

where $\mathbf{T}_\alpha$ is the *partial Cauchy stress tensor*, $\mathbf{b}_\alpha$ is the *partial body force* and $\hat{\mathbf{p}}_\alpha$ is the momentum supply due to the interaction between the α-th constituent and other constituents.

Considering the multiplication of Eq. (2.38) by $\mathbf{v}_\alpha$ and adding the result to Eq. (2.50), we can find the following version for the balance of macroscopic forces

$$\frac{\partial \rho_\alpha \phi_\alpha \mathbf{v}_\alpha}{\partial t} + \nabla \cdot (\rho_\alpha \phi_\alpha \mathbf{v}_\alpha \otimes \mathbf{v}_\alpha) = \nabla \cdot \mathbf{T}_\alpha + \rho_\alpha \phi_\alpha \mathbf{b}_\alpha + (S_\alpha - \nabla \cdot \mathbf{J}_\alpha)\mathbf{v}_\alpha + \hat{\mathbf{p}}_\alpha \ . \tag{2.52}$$

To get the expression displayed in Eq. (2.52) the manipulations are identical to those given in Eq. (2.18).

The *microforce balance* for the α-constituent is given by

$$\nabla \cdot \boldsymbol{\xi}_\alpha + \pi_\alpha + \tau_\alpha = 0. \tag{2.53}$$

where $\boldsymbol{\xi}_\alpha$ is the thermodynamic stress conjugate to the gradient of species volume fractions, π_α is the internal microforce, and τ_α is the external microforce associated with volume fraction (Faghihi et al., 2018).

The sum of the macro-force balances of each species, where each balance is given by Eq. (2.51), results in

$$\sum \rho_\alpha \phi_\alpha \frac{d^\alpha \mathbf{v}_\alpha}{\partial t} = \sum \nabla \cdot \mathbf{T}_\alpha + \sum \rho_\alpha \phi_\alpha \mathbf{b}_\alpha + \sum \hat{\mathbf{p}}_\alpha \ , \tag{2.54}$$

and considering Eq. (2.49) , result in

$$\rho \frac{d\mathbf{v}}{dt} + \sum \nabla \cdot (\rho_\alpha \phi_\alpha \mathbf{u}_\alpha \otimes \mathbf{u}_\alpha) - \sum \mathbf{u}_\alpha \left(S_\alpha - \nabla \cdot \mathbf{J}_\alpha\right) = \sum \nabla \cdot \mathbf{T}_\alpha + \sum \rho_\alpha \phi_\alpha \mathbf{b}_\alpha + \sum \hat{\mathbf{p}}_\alpha, \tag{2.55}$$

or

$$\rho \frac{d\mathbf{v}}{dt} = \nabla \cdot \left\{ \sum \left[\mathbf{T}_\alpha - \rho_\alpha \phi_\alpha \mathbf{u}_\alpha \otimes \mathbf{u}_\alpha \right] \right\} + \sum \rho_\alpha \phi_\alpha \mathbf{b}_\alpha + \sum \left[\mathbf{u}_\alpha \left(S_\alpha - \nabla \cdot \mathbf{J}_\alpha\right) + \hat{\mathbf{p}}_\alpha \right]. \tag{2.56}$$

The total stress of the mixture is given by the sum of the partial stresses of the components plus a correction term. This term arises from the fact that the velocities of the components differ from the mean velocity, contributing to the momentum of the mixture (Epstein, 2012). Comparing Eq. (2.56) with Eq. (2.17) we get

$$\mathbf{T} = \sum_{\alpha=1}^{N} \left[\mathbf{T}_\alpha - \rho_\alpha \phi_\alpha \mathbf{u}_\alpha \otimes \mathbf{u}_\alpha \right], \tag{2.57}$$

$$\mathbf{b} = \frac{1}{\rho} \sum_{\alpha=1}^{N} \rho_\alpha \phi_\alpha \mathbf{b}_\alpha, \tag{2.58}$$

$$\mathbf{0} = \sum \left[\mathbf{u}_\alpha \left(S_\alpha - \nabla \cdot \mathbf{J}_\alpha\right) + \hat{\mathbf{p}}_\alpha \right] = \sum \left[\mathbf{v}_\alpha \left(S_\alpha - \nabla \cdot \mathbf{J}_\alpha\right) + \hat{\mathbf{p}}_\alpha \right]. \tag{2.59}$$

For partial microforces we can describe

$$\xi = \sum_{\alpha=1}^{N} \xi_\alpha, \tag{2.60}$$

$$\pi = \sum_{\alpha=1}^{N} \pi_\alpha, \tag{2.61}$$

$$\tau = \sum_{\alpha=1}^{N} \tau_\alpha. \tag{2.62}$$

Assuming that for each α, $\hat{\mathbf{p}}_\alpha = -\mathbf{v}_\alpha\,(S_\alpha - \nabla\cdot\mathbf{J}_\alpha)$, we have two options for the momentum balance

$$\rho_\alpha\phi_\alpha\frac{\partial\mathbf{v}_\alpha}{\partial t} + \rho_\alpha\phi_\alpha\nabla(\mathbf{v}_\alpha)\mathbf{v}_\alpha = \nabla\cdot\mathbf{T}_\alpha + \rho_\alpha\phi_\alpha\mathbf{b}_\alpha - \mathbf{v}_\alpha\,(S_\alpha - \nabla\cdot\mathbf{J}_\alpha)\ , \tag{2.63}$$

or

$$\frac{\partial\rho_\alpha\phi_\alpha\mathbf{v}_\alpha}{\partial t} + \nabla\cdot(\rho_\alpha\phi_\alpha\mathbf{v}_\alpha\otimes\mathbf{v}_\alpha) = \nabla\cdot\mathbf{T}_\alpha + \rho_\alpha\phi_\alpha\mathbf{b}_\alpha\ . \tag{2.64}$$

2.4.3 Balance of angular momentum

The balance of *angular momentum* in each species, considering nonpolar materials, is given by the symmetry of the partial Cauchy stress tensor

$$\boxed{\mathbf{T}_\alpha = \mathbf{T}_\alpha^T.} \tag{2.65}$$

2.4.4 Energy balance

In the formulation of models of biological phenomena, such as tumor growth, chemical energy plays a crucial role and should be considered as one of the energies that contribute to internal energy. The contribution made by chemical energy will be denoted by $\mathcal{M}_\alpha$. Based on the ideas of Gurtin (1996) and Faghihi et al. (2018), we also consider the work, $\mathcal{W}_\alpha^{\mathrm{m}}(R_t)$, performed by external microforces, in addition to the contribution $\mathcal{W}_\alpha^{\mathrm{s}}(R_t)$, given by standard forces (macroforces), where R_t is an arbitrary part of $\boldsymbol{B}_t$. Considering that the mixture and its constituents are isothermal, the contributions made by the heat flux vector field, $\mathbf{q}_\alpha$, and the heat supply field, r_α, are neglected, thus

$$\frac{d^\alpha}{dt}\int_{R_t}\rho_\alpha\phi_\alpha\varepsilon_\alpha\ dV = \mathcal{W}_\alpha^{\mathrm{s}}(R_t) + \mathcal{W}_\alpha^{\mathrm{m}}(R_t) + \mathcal{M}_\alpha, \tag{2.66}$$

where,

$$\mathcal{W}_\alpha^{\mathrm{s}}(R_t) = \int_{R_t}\mathbf{T}_\alpha : \mathbf{L}_\alpha dV = \int_{R_t}\mathbf{T}_\alpha : \mathbf{D}_\alpha dV\ , \tag{2.67}$$

$$\mathcal{W}_\alpha^{\mathrm{m}}(R_t) = \int_{\partial R_t}(\xi_\alpha\cdot\mathbf{n})\frac{d^\alpha\phi_\alpha}{dt}\ dA + \int_{R_t}\tau_\alpha\frac{d^\alpha\phi_\alpha}{dt}\ dV\ , \tag{2.68}$$

$$\mathcal{M}_\alpha = \int_{R_t}\mu_\alpha S_\alpha\ dV - \int_{\partial R_t}\mu_\alpha\mathbf{J}_\alpha\cdot\mathbf{n}\ dA\ , \tag{2.69}$$

μ_α is the chemical potential the specie. We can rewrite $\mathcal{W}_\alpha^{\mathrm{m}}$ as

$$\begin{aligned}\mathcal{W}_\alpha^{\mathrm{m}}(R_t) &= \int_{R_t} \nabla\cdot\left(\frac{d^\alpha\phi_\alpha}{dt}\xi_\alpha\right)\,dV + \int_{R_t}\tau_\alpha\frac{d^\alpha\phi_\alpha}{dt}\,dV \\ &= \int_{R_t}\left(\frac{d^\alpha\phi_\alpha}{dt}\nabla\cdot\xi_\alpha + \xi_\alpha\cdot\nabla\left(\frac{d^\alpha\phi_\alpha}{dt}\right)\right)\,dV + \int_{R_t}\tau_\alpha\frac{d^\alpha\phi_\alpha}{dt}\,dV\ , \end{aligned} \tag{2.70}$$

and using Eq. (2.19), $\mathcal{W}_\alpha^{\mathrm{m}}(R_t)$ can be rewritten as

$$\begin{aligned}\mathcal{W}_\alpha^{\mathrm{m}}(R_t) &= \int_{R_t}\left(\frac{d^\alpha\phi_\alpha}{dt}\left(-\pi_\alpha-\tau_\alpha\right) + \xi_\alpha\cdot\nabla\left(\frac{d^\alpha\phi_\alpha}{dt}\right)\right)\,dV + \int_{R_t}\tau_\alpha\frac{d^\alpha\phi_\alpha}{dt}\,dV \\ &= \int_{R_t}\left(\xi_\alpha\cdot\nabla\left(\frac{d^\alpha\phi_\alpha}{dt}\right) - \pi_\alpha\frac{d^\alpha\phi_\alpha}{dt}\right)\,dV. \end{aligned} \tag{2.71}$$

The contribution $\mathcal{M}_\alpha$ can be described by

$$\begin{aligned}\mathcal{M}_\alpha &= \int_{R_t}\mu_\alpha S_\alpha\,dV - \int_{R_t}\nabla\cdot\left(\mu_\alpha\mathbf{J}_\alpha\right)\,dV \\ &= \int_{R_t}\mu_\alpha S_\alpha\,dV - \int_{R_t}\left(\mu_\alpha\nabla\cdot\mathbf{J}_\alpha + \mathbf{J}_\alpha\cdot\nabla\mu_\alpha\right)\,dV\ , \end{aligned} \tag{2.72}$$

using Eq. (2.40) the chemical energy can be represented by

$$\begin{aligned}\mathcal{M}_\alpha &= \int_{R_t}\mu_\alpha S_\alpha\,dV - \int_{R_t}\left(\mu_\alpha\left(S_\alpha - \rho_\alpha\phi_\alpha\nabla\cdot\mathbf{v}_\alpha - \frac{d^\alpha\rho_\alpha\phi_\alpha}{dt}\right) + \mathbf{J}_\alpha\cdot\nabla\mu_\alpha\right)\,dV \\ &= \int_{R_t}\left(\mu_\alpha\rho_\alpha\phi_\alpha\nabla\cdot\mathbf{v}_\alpha + \mu_\alpha\frac{d^\alpha\rho_\alpha\phi_\alpha}{dt} - \mathbf{J}_\alpha\cdot\nabla\mu_\alpha\right)\,dV\ . \end{aligned} \tag{2.73}$$

Considering the *Reynolds' transport theorem* on the first member of Eq. (2.66) and passing the derivative into the integral, we arrive at

$$\begin{aligned}\frac{d^\alpha}{dt}\int_{R_t}\rho_\alpha\phi_\alpha\varepsilon_\alpha\,dV &= \int_{R_t}\frac{d^\alpha\rho_\alpha\phi_\alpha\varepsilon_\alpha}{dt} + \rho_\alpha\phi_\alpha\varepsilon_\alpha\nabla\cdot\mathbf{v}_\alpha\,dV \\ &= \int_{R_t}\left(\rho_\alpha\phi_\alpha\frac{d^\alpha\varepsilon_\alpha}{dt} + \varepsilon_\alpha\left(\frac{d^\alpha\rho_\alpha\phi_\alpha}{dt} + \rho_\alpha\phi_\alpha\nabla\cdot\mathbf{v}_\alpha\right)\right)\,dV \\ &= \int_{R_t}\left(\rho_\alpha\phi_\alpha\frac{d^\alpha\varepsilon_\alpha}{dt} + \varepsilon_\alpha\left(S_\alpha - \nabla\cdot\mathbf{J}_\alpha\right)\right)\,dV. \end{aligned} \tag{2.74}$$

Substituting in Eq. (2.66) the expressions of Eqs. (2.67), (2.71), (2.73), and, (2.74), we arrive at

$$\begin{aligned}\int_{R_t}\left(\rho_\alpha\phi_\alpha\frac{d^\alpha\varepsilon_\alpha}{dt} + \varepsilon_\alpha\left(S_\alpha - \nabla\cdot\mathbf{J}_\alpha\right)\right)\,dV &= \int_{R_t}\mathbf{T}_\alpha:\mathbf{D}_\alpha\,dV \\ &+ \int_{R_t}\left(\xi_\alpha\cdot\nabla\left(\frac{d^\alpha\phi_\alpha}{dt}\right) - \pi_\alpha\frac{d^\alpha\phi_\alpha}{dt}\right)\,dV \\ &+ \int_{R_t}\left(\mu_\alpha\rho_\alpha\phi_\alpha\nabla\cdot\mathbf{v}_\alpha + \mu_\alpha\frac{d^\alpha\rho_\alpha\phi_\alpha}{dt} - \mathbf{J}_\alpha\cdot\nabla\mu_\alpha\right)\,dV. \end{aligned} \tag{2.75}$$

Since Eq. (2.75) is valid for every part R_t of $\boldsymbol{B}_t$, it can be written as

$$\rho_\alpha\phi_\alpha\frac{d^\alpha\varepsilon_\alpha}{dt} + \varepsilon_\alpha\left(S_\alpha - \nabla\cdot\mathbf{J}_\alpha\right) = \mathbf{T}_\alpha : \mathbf{D}_\alpha - \pi_\alpha\frac{d^\alpha\phi_\alpha}{dt} + \xi_\alpha\cdot\nabla\left(\frac{d^\alpha\phi_\alpha}{dt}\right) + \mu_\alpha\rho_\alpha\phi_\alpha\nabla\cdot\mathbf{v}_\alpha + \mu_\alpha\frac{d^\alpha\rho_\alpha\phi_\alpha}{dt} - \mathbf{J}_\alpha\cdot\nabla\mu_\alpha. \tag{2.76}$$

Thus, the *local energy balance* for an individual constituent is given by

$$\rho_\alpha\phi_\alpha\frac{d^\alpha\varepsilon_\alpha}{dt} = \mathbf{T}_\alpha : \mathbf{D}_\alpha - \pi_\alpha\frac{d^\alpha\phi_\alpha}{dt} + \xi_\alpha\cdot\nabla\left(\frac{d^\alpha\phi_\alpha}{dt}\right) + \mu_\alpha\rho_\alpha\phi_\alpha\nabla\cdot\mathbf{v}_\alpha + \mu_\alpha\frac{d^\alpha\rho_\alpha\phi_\alpha}{dt} - \mathbf{J}_\alpha\cdot\nabla\mu_\alpha - \varepsilon_\alpha\left(S_\alpha - \nabla\cdot\mathbf{J}_\alpha\right) \tag{2.77}$$

On the other hand, Faghihi et al. (2018) describe the internal energy of the mixture as

$$\rho\frac{d\varepsilon}{dt} = \sum_\alpha\left[\mathbf{T}_\alpha : \mathbf{D}_\alpha - \pi_\alpha\frac{d^\alpha\phi_\alpha}{dt} + \xi_\alpha\cdot\nabla\left(\frac{d^\alpha\phi_\alpha}{dt}\right) + \mu_\alpha\frac{d^\alpha\rho_\alpha\phi_\alpha}{dt} - \mathbf{J}_\alpha\cdot\nabla\mu_\alpha\right], \tag{2.78}$$

where it is considered

$$\rho\frac{d\varepsilon}{dt} = \sum_\alpha\rho_\alpha\phi_\alpha\frac{d^\alpha\varepsilon_\alpha}{dt}\ . \tag{2.79}$$

The energy balance equations for individual constituent (2.77) and for the mixture (2.78) are not equivalent, once we consider

$$\rho\varepsilon = \sum_\alpha\rho_\alpha\phi_\alpha\varepsilon_\alpha\ , \tag{2.80}$$

whose derivative is not equal to Eq. (2.79).

2.4.5 Second law of thermodynamics

According to Rajagopal and Tao (1995) one of the dilemmas encountered when working with a mixture is whether we consider that the entropy inequality holds for each constituent or only for the mixture as a whole. The constraint given by *Clausius-Duhem* inequality will be made on the mixture, as in Faghihi et al. (2018), and not on each individual constituent. Based again on Oden et al. (2010), the inequality for the second law of thermodynamics for the mixture is given by

$$\sum_\alpha\left\{\rho_\alpha\phi_\alpha\frac{d^\alpha\eta_\alpha}{dt} - \frac{1}{\theta_\alpha}\rho_\alpha\phi_\alpha r_\alpha + \eta_\alpha(S_\alpha - \nabla\cdot\mathbf{J}_\alpha) + \nabla\cdot\mathbf{H}_\alpha - \nabla\cdot(\rho_\alpha\phi_\alpha\eta_\alpha\mathbf{u}_\alpha)\right\} \geqslant 0, \tag{2.81}$$

where η_α is the entropy per unit mass, $\mathbf{H}_\alpha$ is the entropy flux in the α th constituent, and θ_α is its absolute temperature.

The entropy density of the mixture is given by the sum of the specific entropy density of each constituent, that is

$$\rho\eta = \sum_\alpha\rho_\alpha\phi_\alpha\eta_\alpha\ , \tag{2.82}$$

and using identity given by Eq. (2.47), we get its derivative defined as

$$\rho\frac{d\eta}{dt} = \sum_{\alpha}\left\{\rho_\alpha\phi_\alpha\frac{d^\alpha\eta_\alpha}{dt} + \eta_\alpha(S_\alpha - \nabla\cdot\mathbf{J}_\alpha) - \nabla\cdot(\rho_\alpha\phi_\alpha\eta_\alpha\mathbf{u}_\alpha)\right\} \ . \tag{2.83}$$

From Eqs. (2.81) and (2.83) we have the inequality

$$\rho\frac{d\eta}{dt} - \sum_{\alpha}\frac{1}{\theta_\alpha}\rho_\alpha\phi_\alpha r_\alpha + \sum_{\alpha}\nabla\cdot\mathbf{H}_\alpha \geqslant 0 \ . \tag{2.84}$$

Considering the entropy flow

$$\mathbf{H}_\alpha = \frac{\mathbf{q}_\alpha}{\theta} + \rho_\alpha\phi_\alpha\eta_\alpha\mathbf{u}_\alpha \ , \tag{2.85}$$

The inequality in Eq. (2.81) takes the form

$$\sum_{\alpha}\left\{\rho_\alpha\phi_\alpha\frac{d^\alpha\eta_\alpha}{dt} - \frac{1}{\theta_\alpha}\rho_\alpha\phi_\alpha r_\alpha + \eta_\alpha(S_\alpha - \nabla\cdot\mathbf{J}_\alpha) + \nabla\cdot\frac{\mathbf{q}_\alpha}{\theta}\right\} \geqslant 0. \tag{2.86}$$

From now on the contributions of $\mathbf{q}_\alpha$ and r_α will be neglected and Eq. (2.86) can be rewritten as

$$\sum_{\alpha}\left\{\rho_\alpha\phi_\alpha\frac{d^\alpha\eta_\alpha}{dt} + \eta_\alpha(S_\alpha - \nabla\cdot\mathbf{J}_\alpha)\right\} \geqslant 0 \ . \tag{2.87}$$

We can rewrite (2.87) in terms of the *Helmholtz free energy*, a measure of the energy available to do work at constant temperature (Capaldi, 2012) which, for constituent α, is given by

$$\psi_\alpha(\boldsymbol{x},t) = \varepsilon_\alpha(\boldsymbol{x},t) - \theta_\alpha(\boldsymbol{x},t)\eta_\alpha(\boldsymbol{x},t), \tag{2.88}$$

and for $\theta_\alpha(x,t) = \theta > 0$, the derivative of Eq. (2.88) is

$$\frac{d^\alpha\psi_\alpha}{dt} = \frac{d^\alpha\varepsilon_\alpha}{dt} - \theta\frac{d^\alpha\eta_\alpha}{dt}. \tag{2.89}$$

Multiplying the Eq. (2.89) by $\rho_\alpha\phi_\alpha$ we have

$$\rho_\alpha\phi_\alpha\frac{d^\alpha\psi_\alpha}{dt} = \rho_\alpha\phi_\alpha\frac{d^\alpha\varepsilon_\alpha}{dt} - \theta\rho_\alpha\phi_\alpha\frac{d^\alpha\eta_\alpha}{dt} \tag{2.90}$$

$$\theta\rho_\alpha\phi_\alpha\frac{d^\alpha\eta_\alpha}{dt} = -\rho_\alpha\phi_\alpha\frac{d^\alpha\psi_\alpha}{dt} + \rho_\alpha\phi_\alpha\frac{d^\alpha\varepsilon_\alpha}{dt} \tag{2.91}$$

$$\rho_\alpha\phi_\alpha\frac{d^\alpha\eta_\alpha}{dt} = \frac{1}{\theta}\left[-\rho_\alpha\phi_\alpha\frac{d^\alpha\psi_\alpha}{dt} + \rho_\alpha\phi_\alpha\frac{d^\alpha\varepsilon_\alpha}{dt}\right]. \tag{2.92}$$

Replacing Eq. (2.92) in the inequality of Eq. (2.87) we arrive at

$$\rho\frac{d\eta}{dt} = \sum_{\alpha}\left\{\frac{1}{\theta}\left[-\rho_\alpha\phi_\alpha\frac{d^\alpha\psi_\alpha}{dt} + \rho_\alpha\phi_\alpha\frac{d^\alpha\varepsilon_\alpha}{dt}\right] + \eta_\alpha(S_\alpha - \nabla\cdot\mathbf{J}_\alpha)\right\} \geqslant 0 \ . \tag{2.93}$$

The free energy per unit volume is

$$\Psi_\alpha = \rho_\alpha\phi_\alpha\psi_\alpha \ , \tag{2.94}$$

and its derivative, by the product rule, is

$$\frac{d^\alpha \Psi_\alpha}{dt} = \rho_\alpha \phi_\alpha \frac{d^\alpha \psi_\alpha}{dt} + \psi_\alpha \frac{d^\alpha \rho_\alpha \phi_\alpha}{dt} \tag{2.95}$$

$$\frac{d^\alpha \Psi_\alpha}{dt} = \rho_\alpha \phi_\alpha \frac{d^\alpha \psi_\alpha}{dt} + \psi_\alpha \left(S_\alpha - \nabla \cdot \mathbf{J}_\alpha - \rho_\alpha \phi_\alpha \nabla \cdot \mathbf{v}_\alpha\right) \tag{2.96}$$

$$\rho_\alpha \phi_\alpha \frac{d^\alpha \psi_\alpha}{dt} = \frac{d^\alpha \Psi_\alpha}{dt} - \psi_\alpha \left(S_\alpha - \nabla \cdot \mathbf{J}_\alpha - \rho_\alpha \phi_\alpha \nabla \cdot \mathbf{v}_\alpha\right) \tag{2.97}$$

$$\rho_\alpha \phi_\alpha \frac{d^\alpha \psi_\alpha}{dt} = \frac{d^\alpha \Psi_\alpha}{dt} - \psi_\alpha \left(S_\alpha - \nabla \cdot \mathbf{J}_\alpha\right) + \Psi_\alpha \operatorname{tr}(\mathbf{L}_\alpha). \tag{2.98}$$

Substituting Eq. (2.98) into Eq. (2.93) we can write

$$\rho \frac{d\eta}{dt} = \sum_\alpha \left\{ \frac{1}{\theta} \left[-\frac{d^\alpha \Psi_\alpha}{dt} + \psi_\alpha \left(S_\alpha - \nabla \cdot \mathbf{J}_\alpha\right) - \Psi_\alpha \operatorname{tr}(\mathbf{L}_\alpha) + \rho_\alpha \phi_\alpha \frac{d^\alpha \varepsilon_\alpha}{dt} \right] + \eta_\alpha (S_\alpha - \nabla \cdot \mathbf{J}_\alpha) \right\} \geqslant 0 \tag{2.99}$$

$$\sum_\alpha \left\{ \frac{1}{\theta} \left[-\frac{d^\alpha \Psi_\alpha}{dt} + (\psi_\alpha + \theta \eta_\alpha)(S_\alpha - \nabla \cdot \mathbf{J}_\alpha) - \Psi_\alpha \operatorname{tr}(\mathbf{L}_\alpha) + \rho_\alpha \phi_\alpha \frac{d^\alpha \varepsilon_\alpha}{dt} \right] \right\} \geqslant 0 \tag{2.100}$$

$$\sum_\alpha \left\{ \frac{1}{\theta} \left[-\frac{d^\alpha \Psi_\alpha}{dt} + \varepsilon_\alpha (S_\alpha - \nabla \cdot \mathbf{J}_\alpha) - \Psi_\alpha \operatorname{tr}(\mathbf{L}_\alpha) + \rho_\alpha \phi_\alpha \frac{d^\alpha \varepsilon_\alpha}{dt} \right] \right\} \geqslant 0 \tag{2.101}$$

since that $\theta > 0$ is constant,

$$\sum_\alpha \left\{ -\frac{d^\alpha \Psi_\alpha}{dt} + \varepsilon_\alpha (S_\alpha - \nabla \cdot \mathbf{J}_\alpha) - \Psi_\alpha \operatorname{tr}(\mathbf{L}_\alpha) + \rho_\alpha \phi_\alpha \frac{d^\alpha \varepsilon_\alpha}{dt} \right\} \geqslant 0 \ . \tag{2.102}$$

Finally, substituting Eq. (2.77) into Eq. (2.102), the second law of thermodynamics can be described as

$$\sum_\alpha \left\{ -\frac{d^\alpha \Psi_\alpha}{dt} - \Psi_\alpha \operatorname{tr}(\mathbf{L}_\alpha) + \mathbf{T}_\alpha : \mathbf{D}_\alpha - \pi_\alpha \frac{d^\alpha \phi_\alpha}{dt} + \xi_\alpha \cdot \nabla \left(\frac{d^\alpha \phi_\alpha}{dt} \right) + \mu_\alpha \frac{d^\alpha \rho_\alpha \phi_\alpha}{dt} - \mathbf{J}_\alpha \cdot \nabla \mu_\alpha + \mu_\alpha \rho_\alpha \phi_\alpha \nabla \cdot \mathbf{v}_\alpha \right\} \geqslant 0 \ . \tag{2.103}$$

2.5 Phase-field

Phase-field models have the ability to simulate the creation and evolution of various morphological patterns, in addition to continuously tracking the movements of the interface.

The Cahn-Hilliard and Allen-Cahn equations are phase-field models widely used to describe the phase separation in a binary mixture. These equations can be derived from the total free energy functional

$$\Psi(p) = \int_B \psi(p, \nabla p)\, d\upsilon, \tag{2.104}$$

where B is the region of space occupied by the material,

$$\psi(p, \nabla p) = f(p) + \frac{1}{2}\alpha \left|\nabla p\right|^2, \tag{2.105}$$

p is the order parameter, $\frac{1}{2}\alpha \left|\nabla p\right|^2$ is the gradient energy, and f is the coarse-grain free energy, a double well potential where the minimum points define the phases (Gurtin, 1996).

Cahn-Hilliard equation is of a fourth-order, conservative and has the form

$$\frac{\partial p}{\partial t} = k\Delta \left(f'(p) - \alpha\Delta p\right), \tag{2.106}$$

where k is constant.

The Allen-Cahn equation is second-order, non-conservative and has the form

$$\beta\frac{\partial p}{\partial t} = -\left(f'(p) - \alpha\Delta p\right), \tag{2.107}$$

where β is constant.

The expression in parentheses in (2.106) and (2.107) is found with the variational derivative of the functional $\Psi(p)$

$$\frac{\delta\Psi(p)}{\delta p} = f'(p) - \alpha\Delta p. \tag{2.108}$$

3 ISOGEOMETRIC ANALYSIS - IGA

The Finite Element Analysis (FEA) is one of the most established methodology to find approximate solution of partial differential equations and has been used for decades by many numerical analysis researchers. Hughes et al. (2005) presented a new method for the analysis of problems governed by differential equations called IsoGeometric Analysis (IGA). The isogeometric analysis has similarities with the FEA, but with surprising computational gains. The main objective of isogeometric analysis is to connect engineering projects, usually produced by a Computer Aided Design (CAD) program and the analysis/simulation processes of these projects.

Most of the engineering fields use CAD-type tools to create and design their projects, but the analysis of these projects did not enjoy all the geometric precision that these tools provide. However, the numerical analysis and simulations of the projects are usually done using the finite element method, which in their calculations use meshes with approximations for the real curved domain, while the representation of the domain by a CAD tool is considered "exact". By using the same base functions in domain creation and numerical simulation, IGA paves the way for greater integration between design and analysis, helping to overcome some bottleneck issues that plagued computer-aided engineering for decades (Lu et al., 2013).

Isogeometric analysis uses Non-Uniform Rational B-Splines (NURBS), which are piecewise rational functions, and are used both to describe the problem domain and to represent its approximate solution as base functions. These functions can accurately represent smooth curves, conic sections, solids, and smooth surfaces. In addition, there are numerous optimized algorithms and efficient implementation that can generate much more complex geometries (Hughes et al., 2005). NURBS are formed by B-Splines functions, which are an alternative to build simpler domains without losing the quality of representation.

Several areas of engineering have successfully used IGA in their research, such as: *Structural Vibrations* (Cottrell et al., 2006), *Incompressibility* (Elguedj et al., 2008; Taylor, 2011), *Plates and Shells* (Echter and Bischoff, 2010; Benson et al., 2010; Benson et al., 2013), *Fluid-Structure Interaction* (Bazilevs et al., 2006; Bazilevs et al., 2011; Bazilevs et al., 2012), *Fluids and Turbulence* (Bazilevs et al., 2007; Akkerman et al., 2007), *Phase Field Analysis* (Gomez et al., 2008; Borden et al., 2012; Liu et al., 2013; Gomez and Zee, 2017), and many others.

In the context of tumor growth, Vilanova et al. (2013) showed a hybrid model of angiogenesis – initially presented by Travasso et al. (2011) – implemented in IGA, where the blood vessels are modeled by a Cahn-Hilliard equation in a continuous manner and

the advancement of the tip cells discretely, operating between time steps of the time discretization. The IGA method context, allowed the discretization of the fourth-order differential operator using a primal formulation, without adding auxiliary variables.

3.1 B-splines functions

The basis functions chosen to be used in IGA are the *B-splines* basis functions, that are piecewise polynomial functions with controlled smoothness. The following definitions and properties have been taken from (Piegl and Tiller, 1997).

To generate a B-splines function we need to specify the number of base functions n, the degree of the polynomial p, and provide a *knot vector* Ξ that is a finite sequence of non-decreasing real numbers

$$\Xi = \{\xi_0, \xi_1, \ldots, \xi_{n+p+1}\}, \tag{3.1}$$

where $\xi_i \in \mathbb{R}$ is called the i^{th} *knot*, i is its *knot* index, and $\xi_i \leqslant \xi_{i+1}$. Once the set Ξ can have repeated *knots*, it is introduced the vector $\boldsymbol{\zeta} = \{\zeta_0, \ldots, \zeta_m\}$ of *knots* without repetitions, and the vector $\boldsymbol{\varrho} = \{r_0, \ldots, r_m\}$ of their corresponding multiplicities with $\sum_{i=0}^{m} r_i = n + p + 1$.

The i^{th} B-spline basis function of degree p, denoted by $N_{i,p}(\xi)$, is constructed using the Cox-de Boor recurrence formulas (Piegl and Tiller, 1997), defined as follows.

For $p = 0$

$$N_{i,0}(\xi) = \begin{cases} 1, & \text{if} \quad \xi_i \leqslant \xi < \xi_{i+1}, \\ 0, & \quad otherwise, \end{cases} \tag{3.2}$$

and for $p = 1, 2, \ldots,$

$$N_{i,p}(\xi) = \frac{\xi - \xi_i}{\xi_{i+p} - \xi_i} N_{i,p-1}(\xi) + \frac{\xi_{i+p+1} - \xi}{\xi_{i+p+1} - \xi_{i+1}} N_{i+1,p-1}(\xi). \tag{3.3}$$

Every time that Eq.(3.3) produces indefinite forms (division by zero) or indeterminate (zero divided by zero) the B-spline basis functions will be zero, $N_{i,p}(\xi) = 0$. The scheme presented in Fig. 3.1 describes the recursion mechanism, which must be truncated when it reaches the desired degree. For $p > 0$, $N_{i,p}(\xi)$ is a linear combination of two $(p-i)$-degree basis functions.

The main properties of the B-spline functions, presented in (Piegl and Tiller, 1997), are:

(1) (Compact support) $N_{i,p}(\xi) = 0$ for ξ outside of interval $[\xi_i, \xi_{i+p+1})$.

(2) In a given interval $[\xi_j, \xi_{j+1})$, at most $p+1$ of $N_{i,p}(\xi)$ are nonzero. Namely $N_{j-p,p}, \ldots, N_{j,p}$.

(3) (Partition of unity) Given an arbitrary interval, $[\xi_i, \xi_{i+1})$, $\sum_{j=i-p}^{i} N_{j,p}(\xi) = 1$, $\forall \xi \in [\xi_i, \xi_{i+1})$.

(4) (Non-negative) $N_{i,p}(\xi) \geqslant 0$ for all i, p and ξ.

(5) (Smoothness) All derivatives of $N_{i,p}(\xi)$ exist within the interval. About *knot* ξ, $N_{i,p}(\xi)$ is $p - k$ times continuously differentiable, where r is the multiplicity of *knot*.

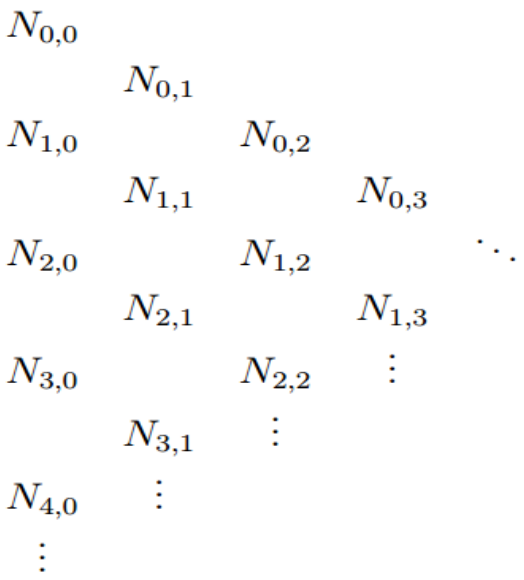

Figure 3.1 – Schematic representation of the recursion mechanism to generate the B-spline basis functions.

The derivative of the B-spline basis function is given by the recursive formula (Piegl and Tiller, 1997)

$$N'_{i,p}(\xi) = \frac{p}{\xi_{i+p} - \xi_i} N_{i,p-1}(\xi) - \frac{p}{\xi_{i+p+1} - \xi_{i+1}} N_{i+1,p-1}(\xi). \tag{3.4}$$

Denoting by $N_{i,p}^{(k)}$ the k^{th} derivative, one obtains

$$N_{i,p}^{(k)}(\xi) = p \left(\frac{N_{i,p-1}^{(k-1)}(\xi)}{\xi_{i+p} - \xi_i} - \frac{N_{i+1,p-1}^{(k-1)}(\xi)}{\xi_{i+p+1} - \xi_{i+1}} \right). \tag{3.5}$$

In the following examples, we show the procedure for finding the expressions for the B-splines functions of degrees 0, 1 and 2. Figures 3.2, 3.3 and 3.4 show their respective graphics. In each example that follows we highlight in red one of the functions and their respective graph.

Example 1. *B-spline functions $N_{i,0}$ of degree $p = 0$, constructed from a vector of non-uniform knots vector*

$$\Xi = \{\xi_0, \xi_1, \xi_2, \xi_3, \xi_4, \xi_5, \xi_6, \xi_7, \xi_8, \xi_9, \xi_{10}\} = \{0, 0, 0, 1, 2, 3, 4, 4, 5, 5, 5\}.$$

$$\begin{aligned}
N_{0,0}(\xi) &= 0 \text{ for } -\infty < \xi < \infty;\\
N_{1,0}(\xi) &= 0 \text{ for } -\infty < \xi < \infty;\\
N_{2,0}(\xi) &= \begin{cases} 1, \text{ if } 0 \leqslant \xi < 1,\\ 0, \text{ otherwise;} \end{cases}\\
N_{3,0}(\xi) &= \begin{cases} 1, \text{ if } 1 \leqslant \xi < 2,\\ 0, \text{ otherwise;} \end{cases}\\
N_{4,0}(\xi) &= \begin{cases} 1, \text{ if } 2 \leqslant \xi < 3,\\ 0, \text{ otherwise;} \end{cases}\\
N_{5,0}(\xi) &= \begin{cases} 1, \text{ if } 3 \leqslant \xi < 4,\\ 0, \text{ otherwise;} \end{cases}\\
N_{6,0}(\xi) &= 0 \text{ for } -\infty < \xi < \infty;\\
N_{7,0}(\xi) &= \begin{cases} 1, \text{ if } 4 \leqslant \xi < 5,\\ 0, \text{otherwise;} \end{cases}\\
N_{8,0}(\xi) &= 0 \text{ for } -\infty < \xi < \infty;\\
N_{9,0}(\xi) &= 0 \text{ for } -\infty < \xi < \infty.
\end{aligned}$$

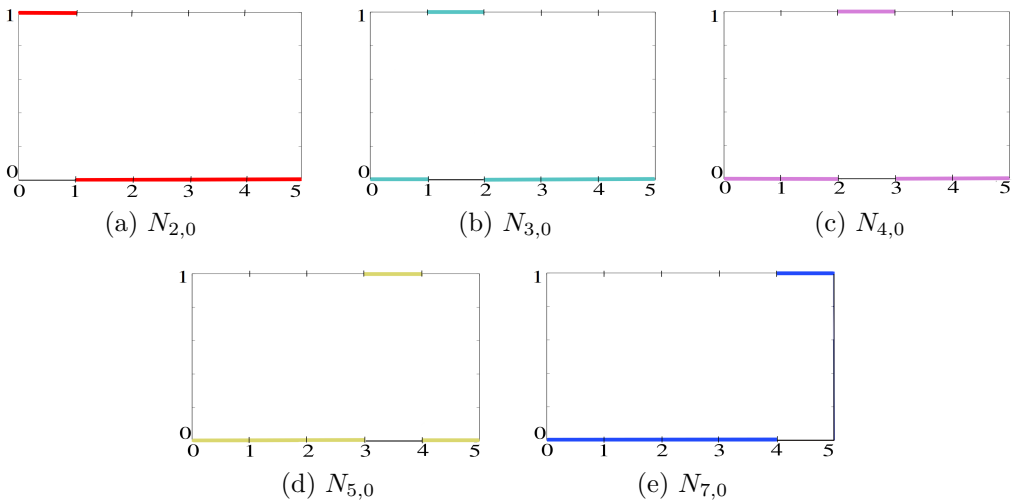

(a) $N_{2,0}$ (b) $N_{3,0}$ (c) $N_{4,0}$

(d) $N_{5,0}$ (e) $N_{7,0}$

Figure 3.2 – The nonzero zeroth degree basis functions.

Example 2. *B-spline functions $N_{i,1}$ of degree $p = 1$, constructed from a vector of non-uniform knots vector*

$$\Xi = \{\xi_0, \xi_1, \xi_2, \xi_3, \xi_4, \xi_5, \xi_6, \xi_7, \xi_8, \xi_9, \xi_{10}\} = \{0, 0, 0, 1, 2, 3, 4, 4, 5, 5, 5\}.$$

$$N_{0,1}(\xi) = \frac{\xi - 0}{0 - 0} N_{0,0}(\xi) + \frac{0 - \xi}{0 - 0} N_{1,0}(\xi) = 0 \quad -\infty < \xi < \infty;$$

$$N_{1,1}(\xi) = \frac{\xi - 0}{0 - 0} N_{1,0}(\xi) + \frac{1 - \xi}{1 - 0} N_{2,0}(\xi) = \begin{cases} 1 - \xi, & 0 \leqslant \xi < 1, \\ 0, & \text{otherwise;} \end{cases}$$

$$N_{2,1}(\xi) = \frac{\xi - 0}{1 - 0} N_{2,0}(\xi) + \frac{2 - \xi}{2 - 1} N_{3,0}(\xi) = \begin{cases} \xi, & 0 \leqslant \xi < 1, \\ 2 - \xi, & 1 \leqslant \xi < 2, \\ 0, & \text{otherwise;} \end{cases}$$

$$N_{3,1}(\xi) = \frac{\xi - 1}{2 - 1} N_{3,0}(\xi) + \frac{3 - \xi}{3 - 2} N_{4,0}(\xi) = \begin{cases} \xi - 1, & 1 \leqslant \xi < 2, \\ 3 - \xi, & 2 \leqslant \xi < 3, \\ 0, & \text{otherwise;} \end{cases}$$

$$N_{4,1}(\xi) = \frac{\xi - 2}{3 - 2} N_{4,0}(\xi) + \frac{4 - \xi}{4 - 3} N_{5,0}(\xi) = \begin{cases} \xi - 2, & 2 \leqslant \xi < 3, \\ 4 - \xi, & 3 \leqslant \xi < 4, \\ 0, & \text{otherwise;} \end{cases}$$

$$N_{5,1}(\xi) = \frac{\xi - 3}{4 - 3} N_{5,0}(\xi) + \frac{4 - \xi}{4 - 4} N_{6,0}(\xi) = \begin{cases} \xi - 3, & 3 \leqslant \xi < 4, \\ 0, & \text{otherwise;} \end{cases}$$

$$N_{6,1}(\xi) = \frac{\xi - 4}{4 - 4} N_{6,0}(\xi) + \frac{5 - \xi}{5 - 4} N_{6,0}(\xi) = \begin{cases} 5 - \xi, & 4 \leqslant \xi < 5, \\ 0, & \text{otherwise;} \end{cases}$$

$$N_{7,1}(\xi) = \frac{\xi - 4}{5 - 4} N_{7,0}(\xi) + \frac{5 - \xi}{5 - 5} N_{8,0}(\xi) = \begin{cases} \xi - 4, & 4 \leqslant \xi < 5, \\ 0, & \text{otherwise;} \end{cases}$$

$$N_{8,1}(\xi) = \frac{\xi - 5}{5 - 5} N_{8,0}(\xi) + \frac{5 - \xi}{5 - 5} N_{9,0}(\xi) = 0 \quad -\infty < \xi < \infty.$$

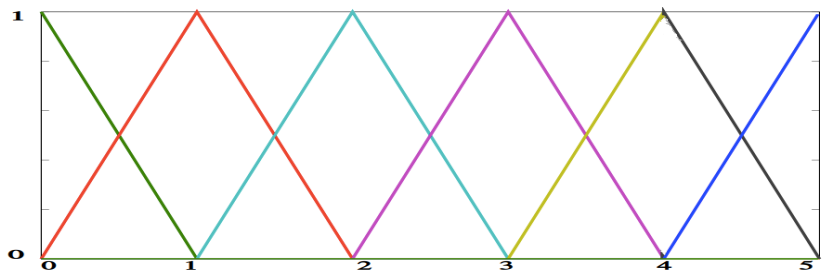

Figure 3.3 – The nonzero first-degree basis functions.

Example 3. *B-spline functions $N_{i,2}$ of degree $p = 2$, constructed from a vector of non-uniform knots vector*

$$\Xi = \{\xi_0, \xi_1, \xi_2, \xi_3, \xi_4, \xi_5, \xi_6, \xi_7, \xi_8, \xi_9, \xi_{10}\} = \{0, 0, 0, 1, 2, 3, 4, 4, 5, 5, 5\}.$$

$$N_{0,2}(\xi) = \frac{\xi - 0}{0 - 0} N_{0,1}(\xi) + \frac{1 - \xi}{1 - 0} N_{1,1}(\xi) = (1 - \xi)^2, \quad 0 \leqslant \xi < 1;$$

$$N_{1,2}(\xi) = \frac{\xi - 0}{1 - 0} N_{1,1}(\xi) + \frac{2 - \xi}{2 - 0} N_{2,1}(\xi) = \begin{cases} 2\xi - (3/2)\xi^2, & 0 \leqslant \xi < 1, \\ (1/2)(2 - \xi)^2, & 1 \leqslant \xi < 2; \end{cases}$$

$$N_{2,2}(\xi) = \frac{\xi - 0}{2 - 0} N_{2,1}(\xi) + \frac{3 - \xi}{3 - 1} N_{3,1}(\xi) = \begin{cases} (1/2)\xi^2, & 0 \leqslant \xi < 1, \\ -(3/2) + 3\xi - \xi^2, & 1 \leqslant \xi < 2, \\ (1/2)(3 - \xi)^2, & 2 \leqslant \xi < 3; \end{cases}$$

$$N_{3,2}(\xi) = \frac{\xi - 1}{3 - 1} N_{3,1}(\xi) + \frac{4 - \xi}{4 - 2} N_{4,1}(\xi) = \begin{cases} (1/2)(\xi - 1)^2, & 1 \leqslant \xi < 2, \\ -(11/2) + 5\xi - \xi^2, & 2 \leqslant \xi < 3, \\ (1/2)(4 - \xi)^2, & 3 \leqslant \xi < 4; \end{cases}$$

$$N_{4,2}(\xi) = \frac{\xi - 2}{4 - 2} N_{4,1}(\xi) + \frac{4 - \xi}{4 - 3} N_{5,1}(\xi) = \begin{cases} (1/2)(\xi - 2)^2, & 2 \leqslant \xi < 3, \\ -16 + 10\xi - (3/2)\xi^2, & 3 \leqslant \xi < 4; \end{cases}$$

$$N_{5,2}(\xi) = \frac{\xi - 3}{4 - 3} N_{5,1}(\xi) + \frac{5 - \xi}{5 - 4} N_{6,1}(\xi) = \begin{cases} (\xi - 3)^2, & 3 \leqslant \xi < 4, \\ (5 - \xi)^2, & 4 \leqslant \xi < 5; \end{cases}$$

$$N_{6,2}(\xi) = \frac{\xi - 4}{5 - 4} N_{6,1}(\xi) + \frac{5 - \xi}{5 - 4} N_{7,1}(\xi) = 2(\xi - 4)(5 - \xi), \quad 4 \leqslant \xi < 5;$$

$$N_{7,2}(\xi) = \frac{\xi - 4}{5 - 4} N_{7,1}(\xi) + \frac{5 - \xi}{5 - 5} N_{8,1}(\xi) = (\xi - 4)^2, \quad 4 \leqslant \xi < 5.$$

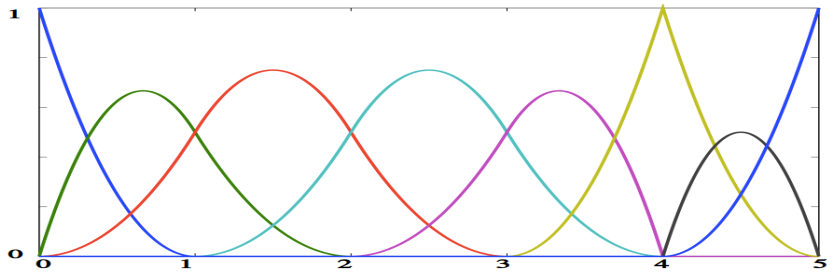

Figure 3.4 – The nonzero second-degree basis functions.

Note that the multiplicity 2 of *knot* 4 reduces the continuity of the function at this point and only continuity C^0 can be achieved at this *knot*. In the other points we have continuity C^1.

3.2 B-splines Curves

Let $\Xi = \{\underbrace{a, \ldots, a}_{p+1}, \xi_{p+1}, \xi_{p+2}, \ldots, \xi_{m-p-1}, \underbrace{b, \ldots, b}_{p+1}\}$ be the vector of *knots* and $N_{i,p}(\xi)$ the B-spline basis functions. A p^{th}-degree B-spline curve is defined by

$$C(\xi) = \sum_{i=0}^{n} N_{i,p}(\xi)\mathbf{P}_i, \tag{3.6}$$

where $\mathbf{P}_i$ represents the control points. Since $N_{i,p}(\xi)$ are piecewise polynomials, the curve $C(\xi)$ will be a piecewise polynomial curve. The polygon formed by the $\{\mathbf{P}_i\}$ is called the *control polygon*, see Fig.3.5 . The degree, p, number of control points, $n+1$, and number of *knots*, $m+1$, are related by $m = n + p + 1$ (Piegl and Tiller, 1997).

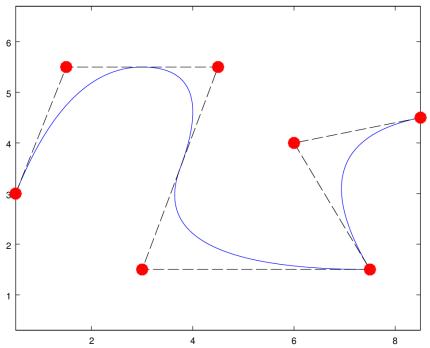

Figure 3.5 – B-spline curve, its control points and the control polygon.

3.3 B-splines surfaces

Let $\{N_{i,p}\}_{i=0}^{n}$ and $\{N_{j,q}\}_{j=0}^{m}$ B-spline basis functions, with degrees p and q, and their respective *knot* vectors

$$\Xi = \{\underbrace{0, \ldots, 0}_{p+1}, \xi_{p+1}, \ldots, \xi_{r-p-1}, \underbrace{1, \ldots, 1}_{p+1}\}, \tag{3.7}$$

and

$$\mathcal{H} = \{\underbrace{0, \ldots, 0}_{q+1}, \eta_{q+1}, \ldots, \eta_{s-q-1}, \underbrace{1, \ldots, 1}_{q+1}\}, \tag{3.8}$$

a B-spline surface is given by the parametrization

$$\mathbf{S}(\xi, \eta) = \sum_{i=0}^{n}\sum_{j=0}^{m} N_{i,p}(\xi)N_{j,q}(\eta)\mathbf{P}_{i,j}, \tag{3.9}$$

where Ξ has $r+1$ *knots*, and $\mathcal{H}$ has $s+1$. The degree, the number of control points and the number of *knots* are related by the equations $r = n + p + 1$ and $s = m + q + 1$.

3.4 Non-Uniform Rational B-Splines

A *Non-Uniform Rational B-Splines* (NURBS) entity in $\mathbb{R}^d$ is obtained by the projective transformation of a B-spline entity in $\mathbb{R}^{d+1}$. With NURBS functions we gain the ability to exactly represent a wide array of objects that cannot be exactly represented by polynomials, in particular, conic sections, such as circles and ellipses.

A p^{th}-degree NURBS curve is defined by

$$\mathbf{C}(\xi) = \frac{\sum_{i=0}^{n} N_{i,p}(\xi) w_i \mathbf{P}_i}{\sum_{i=0}^{n} N_{i,p}(\xi) w_i}, \quad a \leqslant \xi \leqslant b, \tag{3.10}$$

where $\{\mathbf{P}_i\}$ are the control points, the $\{w_i\}$ are weights (positive real numbers), and $\{N_{i,p}(\xi)\}$ the B-spline basis functions defined on the nonperiodic (and nonuniform) knot vector

$$\Xi = \{\underbrace{a, \ldots, a}_{p+1}, \xi_{p+1}, \ldots, \xi_{m-p-1}, \underbrace{b, \ldots, b}_{p+1}\}.$$

We can rewrite (3.10) as

$$\mathbf{C}(\xi) = \sum_{i=0}^{n} R_{i,p}(\xi) \mathbf{P}_i, \quad a \leqslant \xi \leqslant b, \tag{3.11}$$

where $R_{i,p}(\xi)$ are the rational basis functions

$$R_{i,p}(\xi) = \frac{N_{i,p}(\xi) w_i}{\sum_{j=0}^{n} N_{j,p}(\xi) w_j}.$$

Similarly, we can define a NURBS surface of degree p

$$\mathbf{S}(\xi, \eta) = \frac{\sum_{i=0}^{n} \sum_{j=0}^{m} N_{i,p}(\xi) N_{j,q}(\eta) w_{i,j} \mathbf{P}_{i,j}}{\sum_{i=0}^{n} \sum_{j=0}^{m} N_{i,p}(\xi) N_{j,q}(\eta) w_{i,j}} = \sum_{i=0}^{n} \sum_{j=0}^{m} R_{i,j}(\xi, \eta) \mathbf{P}_{i,j}, \quad 0 \leqslant \xi, \eta \leqslant 1 \tag{3.12}$$

where $R_{i,j}(\xi, \eta)$ are the piecewise rational basis functions

$$R_{i,j}(\xi, \eta) = \frac{N_{i,p}(\xi) N_{j,q}(\eta) w_{i,j}}{\sum_{k=0}^{n} \sum_{l=0}^{m} N_{k,p}(\xi) N_{l,q}(\eta) w_{k,l}},$$

defined on the knot vectors

$$\begin{aligned} \Xi &= \{\underbrace{0, \ldots, 0}_{p+1}, \xi_{p+1}, \ldots, \xi_{r-p-1}, \underbrace{1, \ldots, 1}_{p+1}\}, \\ \mathcal{H} &= \{\underbrace{0, \ldots, 0}_{q+1}, \eta_{q+1}, \ldots, \eta_{s-q-1}, \underbrace{1, \ldots, 1}_{q+1}\}. \end{aligned}$$

Figure 3.6 shows a NURBS surface and its control points.

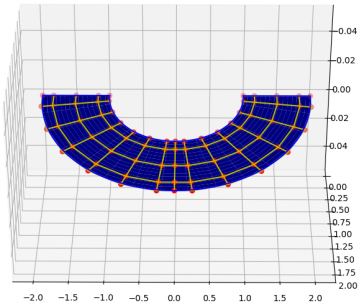

Figure 3.6 – NURBS surface and its control points.

For more details on the construction of the NURBS basis functions, see Piegl and Tiller (1997) and Cottrell et al. (2009).

3.5 Geometric mapping

In the IGA we define a parametric domain, which in $\mathbb{R}^2$ is given by the square $[0,1] \times [0,1]$, and a physical domain, which represents the real domain of the problem. The mesh described at the parametric domain is the tensor product between two *knots* vectors, one in each direction. Each element of the parametric domain is taken into a element of the physical domain by an $\boldsymbol{F}$ mapping, see Fig. 3.7. For purposes of numerically integrating arrays constructed from B-splines, "elements" are taken to be knot spans, namely, $[\xi_i, \xi_{i+1}] \times [\eta_j, \eta_{j+1}]$ (Hughes et al., 2005). Integrals are pulled back to the element of integration by the classical change-of-variables formula and standard Gaussian quadrature rules are employed.

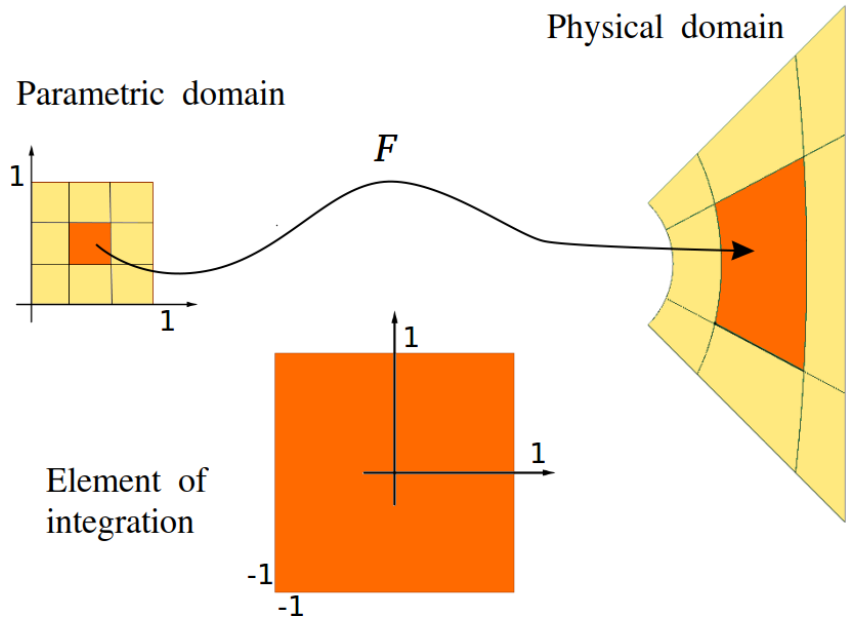

Figure 3.7 – Parametric domain, physical domain and element of integration in a two-dimensional problem.

3.6 PetIGA

The software framework PetIGA (Dalcin et al., 2016) implements the IGA method on top of PETSc, the Portable, Extensible Toolkit for Scientific Computation (Balay et al., 2016), that is, a library (a collection of algorithms and data structures) for the solution of scientific problems modeled by partial differential equations.

The possibility to access the codes for customization and extension gives PETSc a flexibility capable of adapting to the most varied of projects. The codes found in PETSc deal with objects like: Matrices (Mat), Vectors (Vec), Krylov subspace methods (KSP), preconditioners (PC), Nonlinear solvers (SNES) and Time stepping algorithms (TS). Figure 3.8 shows the control flow of petsc.

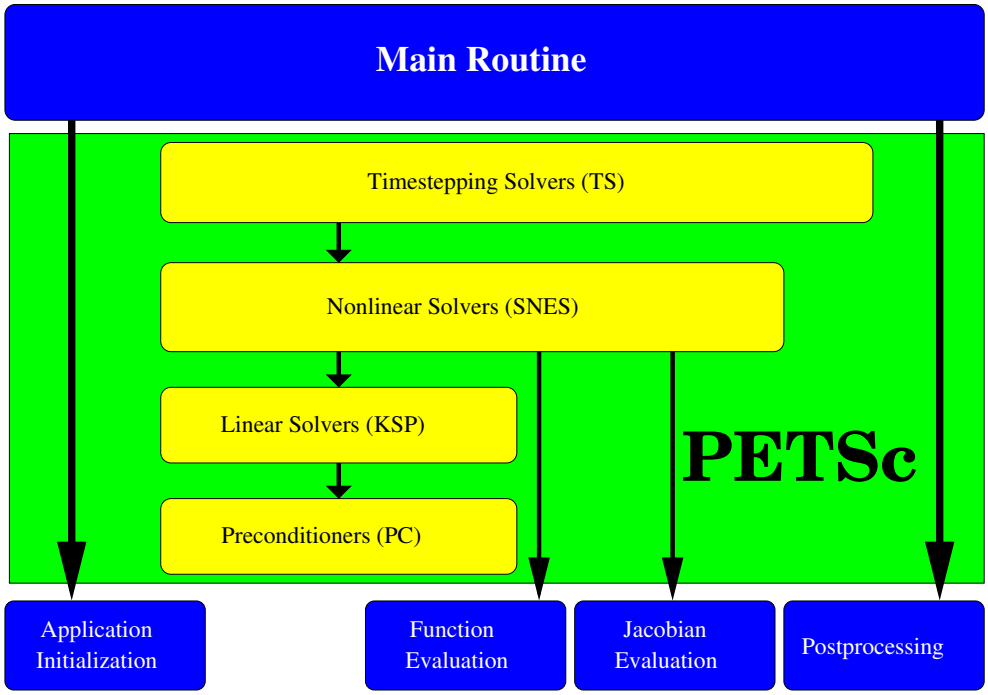

Figure 3.8 – PETSc Framework - Flow of Control for PDE Solution, adapted from (Balay et al., 2016)

PetIGA adds to this library its own collection of objects, preserving all its flexibility and parallelism. Some frequently accessed objects in code using the PetIGA are:

- IGA - The context containing all the discretization information;
- IGAAxis - An axis in one parametric direction of the B-spline space;
- IGABoundary - A edge/face of the B-spline space;
- IGAPoint - A quadrature/collocation point.

For the implementation of a model based on differential equations using the PetIGA tools, we first need to determine the domain and its geometry. For rectangular domain,

it is only required to describe the dimensions of each side. More complex geometries are produced separately with the package igakit, and called from the command line. The igakit implements many of the NURBS routines in Piegl and Tiller (1997) using Fortran. Using the Python language, it facilitates access to the control of a class of NURBS functions, providing the manual and simplified creation of geometries for use in IGA.

To exemplify the use of the igakit package, we describe the creation of a surface, generated with some of its resources. First we load the igakit.cad and igakit.nurbs modules. The plotting features are in the igakit.plot module. For the creation of our surface we will use two semi-circles, c1 and c2, with radius 1 and 2 respectively. The srf surface, annular region between curves c1 and c2, was generated using the ruled function of the cad module. The srf surface has degree 1 in direction 1 and degree 2 in direction 2.

```
from igakit.cad import *
from igakit.nurbs import NURBS
from igakit.plot import plt
c1 = circle(radius=1, angle=(0,pi))
c2 = circle(radius=2,angle=(0,pi))
srf = ruled(c1,c2).transpose()
```

Once created, the surface must be prepared for use in an analysis problem. The inclusion of nodes and the elevation of degree are options to adapt the surface to the problem. With the command refine, we include nodes in both directions and raise the degree of direction 1.

```
srf1 = refine(srf, factor=[3,6], degree=2)
```

The plotting of the graphs is done with the commands

```
plt.plot(srf, color='b')
plt.show()
```

Figure 3.9 shows the steps of the construction process of the srf and srf1 surfaces.

PetIGA was designed with the philosophy that the user do not need to care about anything else besides the discrete approximation of the differential equations system. All the parallelism, that is, domain decomposition, load balance, data communication, quadrature, vector and matrix assembly, etc, are no overhead workload imposed on the user. The main user's task is to code the Residual vector and, for some problems, the Jacobian matrix of the discrete scheme. The assembly of the Jacobian residue and matrix is made using the basis functions and their derivatives, which are provided by PetIGA.

In addition to the domain geometry, the residue and the Jacobian matrix, we need to provide the boundary conditions to be applied to the problem. The choice of base function used, its order and continuity, plus refinement of the mesh in each direction, can be provided internally or at the command line itself.

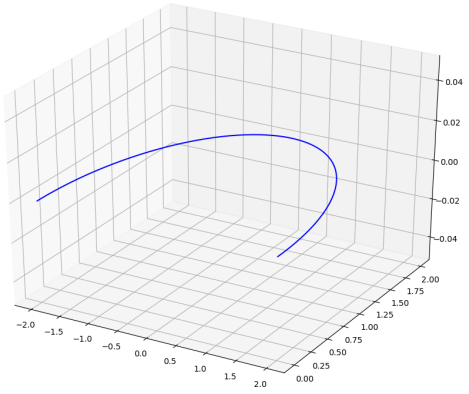

(a) Semi-circle c1.

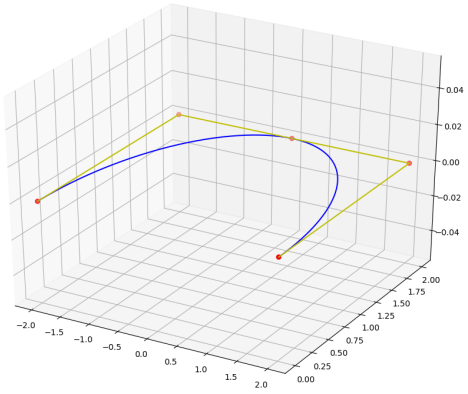

(b) Semi-circle c1, control points and control polygon.

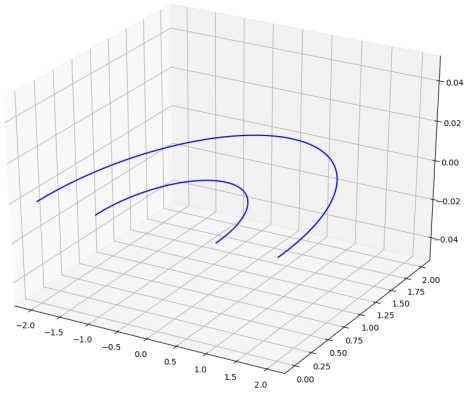

(c) Semi-circles c1 and c2.

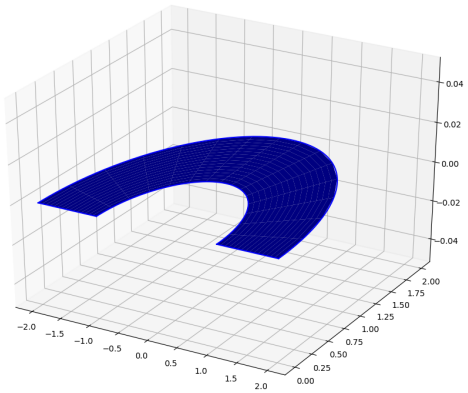

(d) Surface srf.

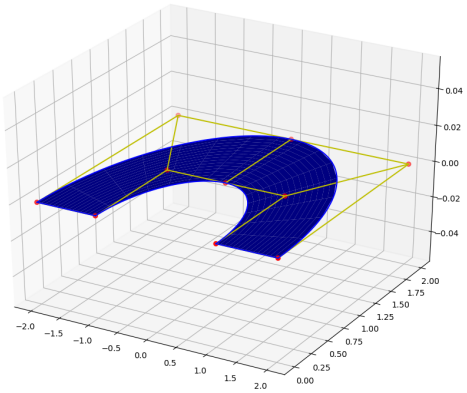

(e) Surface srf and control mesh.

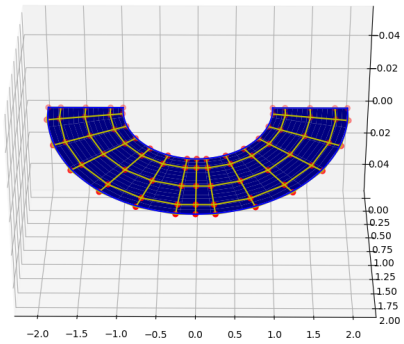

(f) Surface srf1 and control mesh.

Figure 3.9 – Process for building a NURBS surface, using the igakit tool.

All resources produced by PETSc are available for a PetIGA user, such as the various solvers and preconditioners, which, together with strategies of temporal discretization and other resources, contribute to an appropriate solution. The accuracy of the final solution are influenced by all choice of possibilities and also are managed with the efficiency and high capacity of the PETSc parallelism to obtain the the best as possible final solution of the problem.

To solve non-linear systems, PetIGA/PETSc provides several options of resolution methods and we chose to use Newton's method in our implementation. This method requires the specification of the Jacobian matrix of the system. The automatic generation of an approximate Jacobian matrix is one of the facilities found in PetIGA/PETSc, just describing the system residue. We opted for the analytical derivation of the residue for the exact formulation of this matrix. For the solution of the resulting linear system we use the GMRES method (Saad and Schultz, 1986) with 30 vectors to restart and classical Gram-Schmidt orthogonalization, in addition to the ILU preconditioner with tolerance to the zero pivot (2.22045×10^{-14}). The generalized-α method is used for the time integration of the semi-implicit scheme. The adaptive control of the time step is performed by the basic method (the default), where the user provides a desired absolute TolA or a relative TolR error tolerance by invoking TSSetTolerances(). Operates with error estimation based on the local truncation error, and we start the process using the step $\Delta t = 10^{-11}$. For the treatment and visualization of the solution we use igakit, which transforms the *.dat* files generated by PetIGA into *.vtk* files to be used by the multi-platform data analysis and visualization application Paraview (Moreland et al., 2016).

4 PHENOMENOLOGICAL MODEL

The phenomenological model considered in this chapter is of multiscale nature, particularly in the interaction between the tissue and cellular scales within the process of angiogenesis, marking the transition from avascular to vascular phases. Because of this transition, we also call it a hybrid model of tumor growth. Presented by (Xu et al., 2016), the model describes some biological events related to tumor cells, nutrients, endothelial cells and angiogenic factors. The growth and decrease of the tumor, according to the availability of nutrients, and the activation of angiogenesis, triggered by the angiogenic factor, are some of these events. We discuss the implementation of this model, which is based on a system of partial differential equations coupled to an agent-based model that requires extensive computational resources. We use the high performance isogeometric analysis framework, PetIGA (Dalcin et al., 2016), presented in Chapter 3.

The system of partial differential equations models the dynamics of the tumor and of the endothelial cells, and the diffusion of tumor angiogenic factor (TAF) and nutrient, as well as the interaction between them. This system is called the continuous part of the model. An agent-based model, fully coupled to the system, that describes the activation, deactivation, and migration of endothelial cells with tip phenotype is called the discrete part of the model. The discrete part of the model presented by Xu et al. (2016) is based on the work o Travasso et al. (2011), where they describe a model of tumor angiogenesis involving endothelial cells and TAF. The ideas presented by Travasso et al. (2011) were also used by Lima et al. (2014) in their ten species model to describe the interaction between hypoxic and endothelial cells, in the activation of angiogenesis.

4.1 Continuous part

The continuous system of PDEs is nonlinear, of fourth order, and time dependent equations, where the unknowns are ϕ (presence or absence of tumor cells), c (presence or absence of endothelial cells), f(TAF) and σ(nutrients). The continuous phase-field $0 \leqslant \phi \leqslant 1$ describes the host tissue ($\phi \approx 0$) and the tumor ($\phi \approx 1$) phases; the phase-field $-1 \leqslant c \leqslant 1$ describes the avascular tissue ($c \approx -1$) and the capillaries ($c \approx 1$) phases; the field $0 \leqslant f \leqslant 1$ determines the balance concentration between pro- and anti-angiogenic substances; and $0 \leqslant \sigma \leqslant 1$ determines the concentration of available nutrients. Phase-field models have their origin in the material science community, and its application to tumor growth models is discussed in Cristini et al. (2009) and Oden et al. (2010). In Figure 4.1 we have a three-dimensional representation of two phase-fields with the characteristics of fields ϕ and c in $\mathbb{R}^2$ domain.

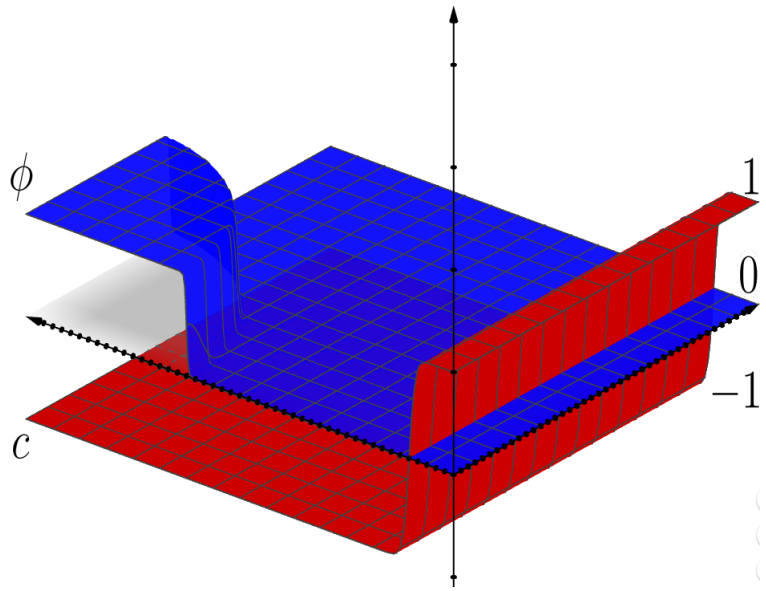

Figure 4.1 – Representation for the phase fields ϕ (blue) and c (red), where $0 \leqslant \phi \leqslant 1$ and $-1 \leqslant c \leqslant 1$.

The layers of the tumor are defined by the amount of nutrients available in the tumor regions. When $\phi \approx 1$, the amount of nutrients defines three types of cells inside the tumor: proliferative ($\sigma \geqslant 0.4$), necrotic ($\sigma \leqslant 0.2$) and hypoxic ($0.2 < \sigma < 0.4$), according to Xu et al. (2016).

The system of differential equations is defined over $\Omega \times (0, T)$, where $\Omega \subset \mathbb{R}^2$ is a rectangular domain and boundary Γ with an outward unit normal $\mathbf{n}$ and $(0, T)$ is the time interval. The problem can be formulated as
Find ϕ, c, f and σ such that

$$\frac{\partial \phi}{\partial t} = M_\phi(\lambda_\phi^2 \Delta\phi - \mu_\phi), \tag{4.1}$$

$$\frac{\partial c}{\partial t} = \nabla \cdot (M_c \nabla(\mu_c - \lambda_c^2 \Delta c)) + \mathcal{B}_p(f) c \mathcal{H}(c), \tag{4.2}$$

$$\frac{\partial f}{\partial t} = \nabla \cdot (D_f \nabla f) + \phi(1 - f)\mathcal{G}(\sigma) - B_u f c \mathcal{H}(c), \tag{4.3}$$

$$\frac{\partial \sigma}{\partial t} = \nabla \cdot (D_\sigma \nabla \sigma) + V_p^c (1 - \sigma) c \mathcal{H}(c) \mathcal{S} - V_u^T \sigma \phi - V_u^H \sigma \mathcal{H}(1 - \phi), \tag{4.4}$$

considering a set of known initial and boundary conditions in $\Gamma \times (0, T)$ such as:

$$\nabla\phi \cdot \mathbf{n} = 0\ , \quad \nabla(\mu_c(c) - \lambda_c^2 \Delta c) \cdot \mathbf{n} = 0\ , \quad \Delta c = 0\ , \quad \nabla f \cdot \mathbf{n} = 0\ , \quad \nabla\sigma \cdot \mathbf{n} = 0\ , \tag{4.5}$$

where (4.1) is an Allen-Cahn equation, which is nonconservative, and (4.2) is a Cahn-Hilliard equation, which is conservative, plus a reative term $\mathcal{B}_p(f) c \mathcal{H}(c)$. M_ϕ represents the tumor mobility and M_c is the mobility for the endothelial cells, the parameter λ_ϕ is a length scale that defines the thickness of the diffuse interface between the tumor and the host tissue, and λ_c is a length scale that defines the thickness of the capillary wall. These

equations are derivable from appropriate "total free energy" functionals

$$\Psi_\phi(\phi, \nabla\phi, \sigma) = \int_\Omega \psi_\phi^s(\nabla\phi) + \psi_\phi^{ch}(\phi, \sigma) d\mathbf{x}, \tag{4.6}$$

$$\Psi_c(c, \nabla c) = \int_\Omega \psi_c^s(\nabla c) + \psi_c^{ch}(c) d\mathbf{x}, \tag{4.7}$$

where ψ_ϕ^s and ψ_c^s are the surface free energy, ψ_ϕ^{ch} and ψ_c^{ch} are the chemical free energy, given by

$$\psi_\phi^s(\nabla\phi) = \frac{1}{2}\lambda_\phi^2 |\nabla\phi|^2, \tag{4.8}$$

$$\psi_c^s(\nabla c) = \frac{1}{2}\lambda_c^2 |\nabla c|^2, \tag{4.9}$$

$$\psi_\phi^{ch}(\phi, \sigma) = g(\phi) + m(\sigma)h(\phi), \tag{4.10}$$

$$\psi_c^{ch}(c) = \frac{c^4}{4} - \frac{c^2}{2}, \tag{4.11}$$

where

$$g(\phi) = \phi^2(1-\phi)^2, \tag{4.12}$$

$$h(\phi) = \phi^2(3-2\phi), \tag{4.13}$$

$$m(\sigma) = \frac{-2}{3.01\pi}\arctan(15(\sigma - \sigma^{h-v})). \tag{4.14}$$

The function ψ_c^{ch} is symmetric, with minima at $c = -1$ and $c = 1$. The function $g(\phi)$ is symmetric with minima at $\phi = 0$ and $\phi = 1$, and the product $m(\sigma)h(\phi)$ is a function that, according to the variation of σ, disturbs the symmetry of ψ_ϕ^{ch}. The coefficient $\frac{2}{3.01\pi}$ $\left(< \frac{2}{3\pi}\right)$ was chosen so that $|m| < 3$ for every σ value. Thus, the function ψ_ϕ^{ch} assumes local minimums at $\phi = 0$ and $\phi = 1$. Figure 4.2 shows how the σ values modify the symmetry of the ψ_ϕ^{ch} function.

The variational derivative of $\Psi_\phi(\phi, \nabla\phi, \sigma)$ and $\Psi_c(c, \nabla c)$ provide fundamental parts of equations (4.1) and (4.2), and are given by

$$\frac{\delta\Psi_\phi}{\delta\phi} = \lambda_\phi^2\Delta\phi + \frac{\partial\psi_\phi^{ch}}{\partial\phi} = \lambda_\phi^2\Delta\phi + \mu_\phi, \tag{4.15}$$

$$\frac{\delta\Psi_c}{\delta c} = \lambda_c^2\Delta c + \frac{\partial\psi_c^{ch}}{\partial c} = \lambda_c^2\Delta c + \mu_c. \tag{4.16}$$

The function μ_ϕ and μ_c are the chemical potentials of the tumor and capillaries (Cristini et al., 2009; Oden et al., 2010), given by

$$\mu_\phi(\phi, \sigma) = \frac{\partial\psi_\phi^{ch}}{\partial\phi} = 2\phi(1-\phi)(1-2\phi) - \frac{12}{3.01\pi}\phi(1-\phi)\arctan(15(\sigma - \sigma^{h-v})) \tag{4.17}$$

$$\mu_c(c) = \frac{\partial\psi_c^{ch}}{\partial c} = c^3 - c, \tag{4.18}$$

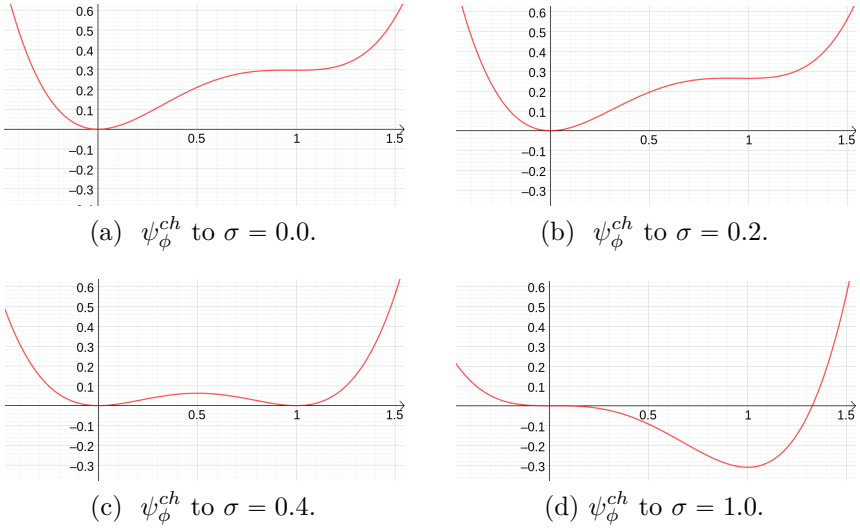

(a) ψ_ϕ^{ch} to $\sigma = 0.0$. (b) ψ_ϕ^{ch} to $\sigma = 0.2$.

(c) ψ_ϕ^{ch} to $\sigma = 0.4$. (d) ψ_ϕ^{ch} to $\sigma = 1.0$.

Figure 4.2 – Graph of ψ_ϕ^{ch}, considering $\sigma^{h-v} = 0.4$, and the following constant values for σ: (a) $\sigma = 0.0$, (b) $\sigma = 0.2$, (c) $\sigma = 0.4$, and (d) $\sigma = 1.0$.

where σ^{h-v} is constant and represent the value of the nutrient concentration that defines the threshold between hypoxic tumor and viable-cell.

The proliferation rate of the endothelial cells is given by the function $\mathcal{B}_p(f)$, defined as follows

$$\mathcal{B}_p(f) = \begin{cases} B_p f & \text{if} \quad f < f_p \\ B_p f_p & \text{if} \quad f \geqslant f_p \end{cases}, \tag{4.19}$$

where B_p and f_p are constants. For numerical reasons, $\mathcal{H}$ is a smoothed-out Heaviside step function, given by

$$\mathcal{H}(x) = \frac{1}{2}\left[1 + \frac{1}{\sqrt{\pi}}\int_{-kx}^{kx} e^{-t^2} dt\right] = \frac{1}{2}\left[1 + \operatorname{erf}(kx)\right], \tag{4.20}$$

where k is a positive constant, that controls the thickness of the interface, and $\operatorname{erf}(\cdot)$ is the error function.

Equations (4.3) and (4.4) are reaction–diffusion equations and control the distribution of angiogenic factor and nutrient. D_f and D_σ represent the diffusion coefficients of f and σ, respectively. The proliferation rate of the f is given by the constant B_u. The function $\mathcal{G}$ is the secretion rate of tumor angiogenic factor released by tumor cells, defined as follows

$$\mathcal{G}(\sigma) = 0.008 \exp\left[-125\left(\sigma - \frac{\sigma^{n-h} + \sigma^{h-v}}{2}\right)^2\right], \tag{4.21}$$

where σ^{n-h} is constant and represent the value of the nutrient concentration that defines the threshold between necrotic and hypoxic tumor. The graphs of functions $\mathcal{B}_p$ and $\mathcal{G}$ are shown in Figure 4.3.

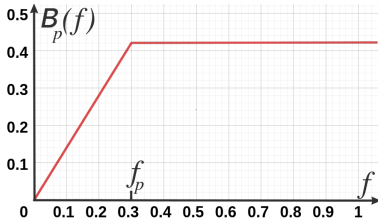

(a) Graph of $\mathcal{B}_p$, considering $f_p = 0.3$ and $B_p = 1.401$.

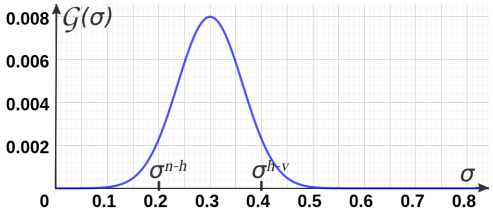

(b) Graph of $\mathcal{G}$, considering $\sigma^{n-h} = 0.2$ and $\sigma^{h-v} = 0.4$.

Figure 4.3 – Graphs of $\mathcal{B}_p$ and $\mathcal{G}$, considering the constant values used in the experiments.

The function $\mathcal{S}$ is a crude measure of the structure and density of the capillary network. The length of each capillary is represented by l_i and, in a vasculature with n capillaries, $\mathcal{S}$ is given by

$$\mathcal{S} = \frac{l_{\max}}{\sum_{i=1}^{n} l_i}, \tag{4.22}$$

where $l_{\max} = \max_{i \leqslant i \leqslant n}(l_i)$. The constant values V_p^c, V_u^T and V_u^H represent, respectively, the production rate of nutrient, uptake rate of nutrient by tumor and uptake rate of nutrient by host tissue.

4.2 Discrete part

The discrete part controls, between a time step and another, the activation and advancement of the tip cell. Travasso et al. (2011) considers the advancement of the tip cell according to the vector $\mathbf{v}$, which is a multiple of the gradient of the angiogenic factor f. To describe the resistance of the movement in some directions Lima et al. (2014) used the same vector $\mathbf{v}$ multiplied by a random tensor $\mathbf{K}$, called conductivity tensor. Xu et al. (2016) incorporated into the cell's movement a change in the speed of advancement upon contact with the tumor. The ideas considered by Lima et al. (2014) provided a more realistic shape to the created capillaries, whereas the Xu et al. (2016) considerations prevented the new capillary from crossing the tumor with the same speed achieved in the extracellular matrix. In this work, we consider the ideas from Xu et al. (2016) and Lima et al. (2014) for assembly the tip cell velocity vector in the discrete part of the model.

When the discrete part is activated, the points of the domain are evaluated regarding the conditions for activation of a tip cell. The conditions for a new tip cell to be activated are:

(i) the point is inside a capillary;

(ii) the nearby concentration of TAF is above a threshold level;

(iii) the distance to any other active tip endothelial cell is larger than a fixed distance – named δ_4.

These conditions couple the continuous and the discrete parts. When an activated tip cell fails to satisfy one of the three conditions above, it is deactivated. Given an $\mathbf{x}$ point in the domain, we can mathematically represent (i), (ii) and (iii) as follows:

$$c(\mathbf{x}) \geqslant c_{act}, \tag{4.23}$$

$$f(\mathbf{x}) \geqslant f_{act}, \tag{4.24}$$

$$\|\mathbf{x} - \mathbf{x}_{tip}^j\| \geqslant \delta_4, \quad \forall j = 1, ..., N_{tip}(t_n), \tag{4.25}$$

where $\mathbf{x}_{tip}^j$ is the center of Ω_{tip}^j, a subdomain that represents one of the $N_{tip}(t_n)$ active tip endothelial cells at instant t_n. The constant c_{act} represents the minimum value for the domain point to be considered an endothelial cell and the constant f_{act} represents the minimum necessary value of TAF to modify the phenotype of an endothelial cell to become a tip cell. The minimum distance between an activated tip cell and a new tip cell is given by the constant δ_4.

To track the domain a finer subgrid is created in each element of the discretized domain as shown in Fig. 4.4.

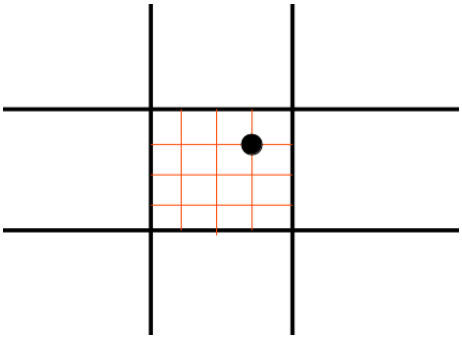

Figure 4.4 – A point highlighted in a subgrid of the discretized domain.

Among the points that satisfy all those conditions one of them, namely $\mathbf{x}_{tip}^k$, is randomly chosen to be activated, generating a new tip Ω_{tip}^k subdomain (cell). A subdomain Ω_{tip}^j will be deactivated if the center $\mathbf{x}_{tip}^j$ does not satisfy any of the conditions (4.23), (4.24) or (4.25). In Fig. 4.5 (a) a point of the domain satisfying the conditions is detected and called $\mathbf{x}_{tip}$ and in Fig. 4.5 (b) a subdomain Ω_{tip} with center $\mathbf{x}_{tip}$ is created.

Subdomains created between the time steps must be introduced into the problem in the following time step to calculate the solution. In Xu et al. (2016) the new subdomains, created in the discrete part, were incorporated into the continuous part with the aid of the *model functions*, smooth representations of the phase changes. In our code we considered a projection of the discontinuous function, which has value 1 on the subdomain and c value over other domain points. The projection was very efficient, smoothing and eliminating the discontinuity of the function.

Additionally, the current active tip endothelial cell migrates according to

$$\mathbf{x}_{tip}^j := \mathbf{x}_{tip}^j + \Delta t_n \mathbf{v}_{tip}^j, \tag{4.26}$$

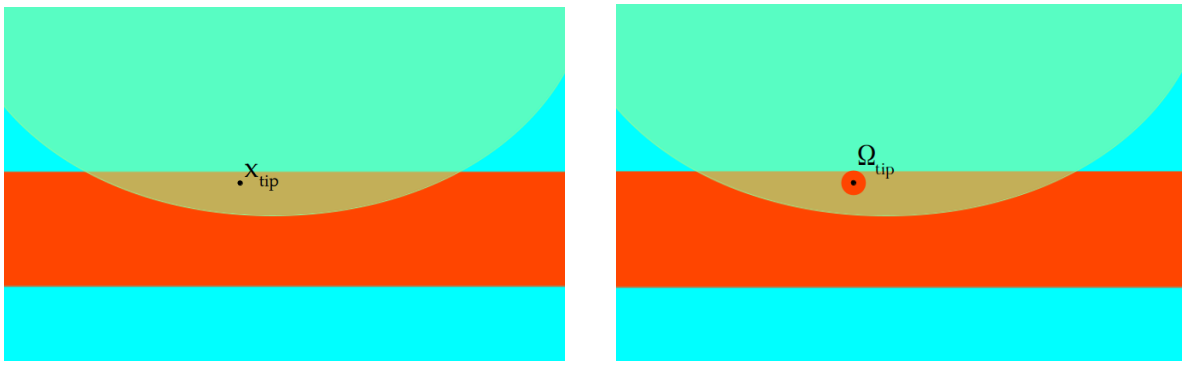

(a) A point of the domain satisfying the conditions is detected and called $\mathbf{x}_{tip}$.

(b) A subdomain Ω_{tip} with center $\mathbf{x}_{tip}$ is created.

Figure 4.5 – Detection of a tip cell $\mathbf{x}_{tip}$ and creation of an Ω_{tip} subdomain. In red the vessel and in green the concentration of the angiogenic factor.

where the vector $\mathbf{v}_{tip}^{j}$ defines the direction and intensity of propagation for the advance of the tip cell Ω_{tip}^{j}. The direction of movement of a tip cell is represented in Fig. 4.6(a) by vector $\mathbf{v}_{tip}^{j}$, and its new position is represented in Fig. 4.6(b).

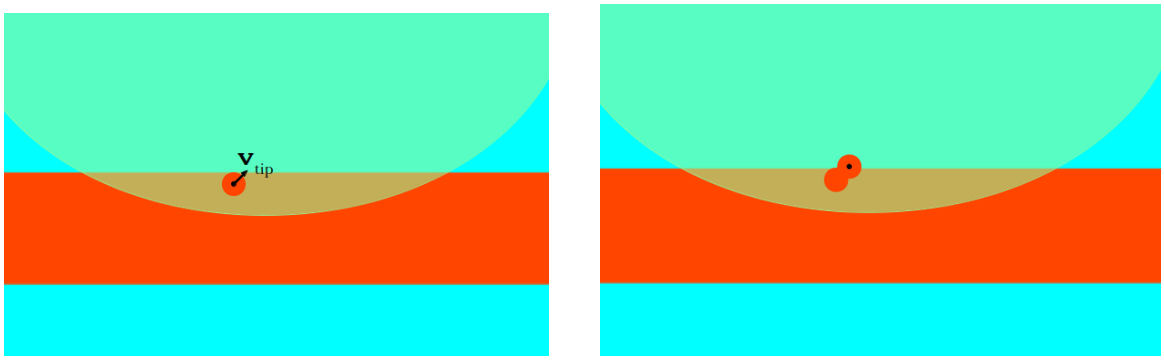

(a) Vector $\mathbf{v}_{tip}$, originated in $\mathbf{x}_{tip}$, giving direction to advance the tip cell.

(b) New position of the tip cell, adding a new region occupied by the capillaries.

Figure 4.6 – Movement of a domain Ω_{tip}, direction and advance of a tip cell. In red the vessel and in green the angiogenic factor.

The advance of the tip cell according to a multiple of the gradient of the angiogenic factor concentration within this agent-based model was first introduced by Travasso et al. (2011). However the gradient direction does not incorporate in the modeling process some anisotropy introduced by the extracelullar matrix (ECM). Indeed, this resistance is due to the composition of the ECM, formed by a scaffolding of fibers (collagen, elastin, fibronectin, etc.) embedded in a mixture of water and glycoproteins (Cristini and Lowengrub, 2010), which influences the direction of capillary growth. To describe the resistance of the movement in some directions, given by the heterogeneity of the extracellular matrix, Lima et al. (2014), inspired by Sun et al. (2005), introduced the random tensor $\mathbf{K}$. The conductivity tensor of the extracellular matrix is defined in two and three dimensions by

$$K_{2d} = k_h \begin{bmatrix} v_x^2 & v_x v_y \\ v_x v_y & v_y^2 \end{bmatrix} + \frac{k_h}{k_a} \begin{bmatrix} v_y^2 & -v_x v_y \\ -v_x v_y & v_x^2 \end{bmatrix} \tag{4.27}$$

$$K_{3d} = k_h \begin{bmatrix} v_x^2 & v_x v_y & v_x v_z \\ v_x v_y & v_y^2 & v_y v_z \\ v_x v_z & v_y v_z & v_z^2 \end{bmatrix} + \frac{k_h}{k_a} \begin{bmatrix} v_y^2 & -v_x v_y & v_y v_z \\ -v_x v_y & v_x^2 & -v_x v_z \\ v_y v_z & -v_x v_z & v_z^2 \end{bmatrix} \tag{4.28}$$

where $\mathbf{v}_2 = (v_x, v_y)$ in 2D, or $\mathbf{v}_3 = (v_x, v_y, v_z)$ in 3D, is a unitary and random vector, k_h and k_a are a measures of heterogeneity and anisotropy, respectively. In this work we consider $k_h = 1$ and $k_a = 5$, in Lima et al. (2014) k_a varies randomly between 1 and 10.

Finally, Xu et al. (2016) incorporated into the cell's movement a change in the speed of advancement upon contact with the tumor. The function

$$\mathcal{I}(\phi) = 0.45[\tanh(50(0.5 - \phi)) + 1.0] + 0.1, \tag{4.29}$$

incorporates the observation that once the capillaries penetrate into the tumor, their movements are constrained. Indeed, for large ϕ (inside the tumor) $\mathcal{I}(\phi)$ is close to 0.1, while for small ϕ (outside the tumor) it is approximately equal to 1.0. In other cases, $\mathcal{I}(\phi)$ takes values in the interval $(0, 1)$ providing a quick, but a smooth transition between 0.1 and 1 (Xu et al., 2016).

In this work we consider $\mathbf{v}_{tip}^j$ inspired by definitions of Sun et al. (2005), Lima et al. (2014), Xu et al. (2016) as

$$\mathbf{v}_{tip}^j = \mathbf{K} \left[\chi \frac{\nabla f(\mathbf{x}_{tip}^j)}{\| \nabla f(\mathbf{x}_{tip}^j) \|} \mathcal{I}(\phi) \right], \tag{4.30}$$

where χ is a chemotactic constant.

We implemented the agent-based model in C/C++ using STL (Standard Template Library) data structures coupling it with the discretization of the continuous part. We set the activation of the discrete part only every 4 time steps. For more details on the formulation of the discrete part, please see Travasso et al. (2011), Vilanova et al. (2013), Lima et al. (2014), Xu et al. (2016).

4.3 Computational method

The numerical solution of the continuous system (4.1)-(4.4) and the discrete part described in Section 4 is challenging since the model presents strong non-linearities, besides fourth-order differential operators in space. We used spline-based isogeometric analysis method (IGA) (Hughes et al., 2005) to discretize the system, and implemented it in PetIGA (Dalcin et al., 2016). The easy generation of quadratic basis functions with

continuous derivative within the context of the IGA method allowed to discretize the fourth-order differential operator using a primal formulation without adding auxiliary variables. Similar problems are usually solved using finite differences, as in the case of Travasso et al. (2011) , or creating new unknowns to reduce the order of the equations, as in Lima et al. (2014).

4.3.1 The weak form

We seek the solution of the weak form of the problem in space $\mathcal{V} \subset \mathcal{H}^2$, where $\mathcal{H}^2$ is the Sobolev space of square-integrable functions with square-integrable first and second derivatives. We find the weak form of the problem by multiplying the equations (4.1)-(4.4) by the respective test functions $w_\phi,\ w_c,\ w_f$ e w_σ, integrating over the domain Ω, applying the integration rules by parts, and considering the boundary conditions (4.5). The test functions also belong to the set $\mathcal{V}$. Thus we can write the problem in the following way:

Given the initial conditions, find $\phi,\ c,\ f,\ \sigma \in \mathcal{V}$ *such that for all* $w_\phi,\ w_c,\ w_f, w_\sigma \in \mathcal{V}$

$$\left(w_\phi, \frac{\partial \phi}{\partial t}\right)_\Omega + \left(\nabla w_\phi\ ,\ M_\phi \lambda_\phi^2 \nabla \phi\right)_\Omega + \left(w_\phi,\ M_\phi \mu_\phi(\phi, \sigma)\right)_\Omega = 0, \tag{4.31}$$

$$\left(w_c, \frac{\partial c}{\partial t}\right)_\Omega + \left(\nabla w_c,\ M_c \nabla \mu_c(c)\right)_\Omega + \left(\Delta w_c, M_c \lambda_c^2 \Delta c\right)_\Omega - \left(w_c, \mathcal{B}_p(f) c \mathcal{H}(c)\right)_\Omega = 0, \tag{4.32}$$

$$\left(w_f, \frac{\partial f}{\partial t}\right)_\Omega + \left(\nabla w_f,\ D_f \nabla f\right)_\Omega - \left(w_f\ ,\ \phi(1-f)\mathcal{G}(\sigma)\right)_\Omega + \left(w_f\ , B_u f c \mathcal{H}(c)\right)_\Omega = 0, \tag{4.33}$$

$$\left(w_\sigma, \frac{\partial \sigma}{\partial t}\right)_\Omega + \left(\nabla w_\sigma, D_\sigma \nabla \sigma\right)_\Omega + \left(w_\sigma, V_u^T \sigma \phi + V_u^H \sigma \mathcal{H}(1-\phi) - V_p^c (1-\sigma) c \mathcal{H}(c) \mathcal{S}\right)_\Omega = 0, \tag{4.34}$$

where $(\cdot\ ,\ \cdot)_\Omega$ is the $L^2(\Omega)$ inner product. Boundary conditions (4.5) were used to cancel the following terms:

$$\begin{aligned}
\left(M_\phi \lambda_\phi^2 w_\phi \nabla \phi\ , \mathbf{n}\right)_\Gamma &= 0, \\
\left(M_c w_c \nabla(\mu_c(c) - \lambda_c^2 \Delta c)\ , \mathbf{n}\right)_\Gamma &= 0, \\
\left(D_f w_f \nabla f\ , \mathbf{n}\right)_\Gamma &= 0, \\
\left(D_\sigma w_\sigma \nabla \sigma\ , \mathbf{n}\right)_\Gamma &= 0.
\end{aligned}$$

4.3.2 Spatial discretization

For a spatial discretization of the weak form of the problem, we use the Galerkin method. We now look for the solution to the problem in a finite-dimensional space $\mathcal{V}^h \subset \mathcal{V}$, generated by the basic functions $\{N_A\}_{A=1,\ldots,n_b}$, where the N_A functions are B-splines of degree 2, an thus are of class $C^1(\Omega)$, and n_b is the dimension of the discrete subspace $\mathcal{V}^h$. Class C^1 functions are required to solve the Cahn-Hilliard equation, which is of the fourth

order, in a primal variational framework. We define the discrete fields as

$$\phi^h(x,t) = \sum_{A=1}^{n_b} \phi_A(t) N_A(x), \tag{4.35}$$

$$c^h(x,t) = \sum_{A=1}^{n_b} c_A(t) N_A(x), \tag{4.36}$$

$$f^h(x,t) = \sum_{A=1}^{n_b} f_A(t) N_A(x), \tag{4.37}$$

$$\sigma^h(x,t) = \sum_{A=1}^{n_b} \sigma_A(t) N_A(x), \tag{4.38}$$

where the coefficients $\phi_A(t),\ c_A(t),\ f_A(t),\ \sigma_A(t)$ are the control variables, which are the degrees of freedom, are located at the control points. The non-interpolatory nature of the basis prevents strictly interpreting the control variables as we can do with nodal values in FEA (Cottrell et al., 2009).

We define $\boldsymbol{\phi}, \boldsymbol{c}, \boldsymbol{f}, \boldsymbol{\sigma}$ the vectors formed by the sequences of control variables as,

$$\boldsymbol{\phi} = \left[\phi_1(t), \cdots, \phi_{n_b}(t)\right]^T, \tag{4.39}$$

$$\boldsymbol{c} = \left[c_1(t), \cdots, c_{n_b}(t)\right]^T, \tag{4.40}$$

$$\boldsymbol{f} = \left[f_1(t), \cdots, f_{n_b}(t)\right]^T, \tag{4.41}$$

$$\boldsymbol{\sigma} = \left[\sigma_1(t), \cdots, \sigma_{n_b}(t)\right]^T. \tag{4.42}$$

The finite-dimensional problem can then be formulated as:

Find $\phi^h,\ c^h,\ f^h,\ \sigma^h \in \mathcal{V}^h$ *such that for all* $w_\phi^h,\ w_c^h,\ w_f^h, w_\sigma^h \in \mathcal{V}^h$

$$\begin{aligned}
&\left(w_\phi^h, \frac{\partial \phi^h}{\partial t}\right)_\Omega + \left(\nabla w_\phi^h, M_\phi \lambda_\phi^2 \nabla \phi^h\right)_\Omega + \left(w_\phi^h, M_\phi \mu_\phi(\phi^h, \sigma^h)\right)_\Omega = 0,\\
&\left(w_c^h, \frac{\partial c^h}{\partial t}\right)_\Omega + \left(\nabla w_c^h, M_c \nabla \mu_c(c^h)\right)_\Omega + \left(\Delta w_c^h\ ,\ M_c \lambda_c^2 \Delta c^h\right)_\Omega - \left(w_c^h, \mathcal{B}_p(f^h) c^h \mathcal{H}(c^h)\right)_\Omega = 0,\\
&\left(w_f^h, \frac{\partial f^h}{\partial t}\right)_\Omega + \left(\nabla w_f^h,\ D_f \nabla f^h\right)_\Omega - \left(w_f^h,\ \phi^h(1-f^h)\mathcal{G}(\sigma^h)\right)_\Omega + \left(w_f^h, B_u f^h c^h \mathcal{H}(c^h)\right)_\Omega = 0,\\
&\left(w_\sigma^h, \frac{\partial \sigma^h}{\partial t}\right)_\Omega + \left(\nabla w_\sigma^h, D_\sigma \nabla \sigma^h\right)_\Omega +\\
&\qquad + \left(w_\sigma^h, V_u^T \sigma^h \phi^h + V_u^H \sigma^h \mathcal{H}(1-\phi^h) - V_p^c (1-\sigma^h) c^h \mathcal{H}(c^h) \mathcal{S}\right)_\Omega = 0.
\end{aligned}$$

4.3.3 Time discretization

For the time integration of the mathematical model, we use a semi-implicit scheme based on the generalized-α method (Chung and Hulbert, 1993), with adaptive time

stepping provided by PETSc (Balay et al., 2016), which operates with error estimation based on the local truncation error (LTE). The time interval $(0, T)$ is divided into time intervals of size $\Delta t_n = t_{n+1} - t_n$. We consider the notation $\phi_n^h, c_n^h, f_n^h, \sigma_n^h$ to represent $\phi^h(x, t_n), c^h(x, t_n), f^h(x, t_n), \sigma^h(x, t_n)$ and the respective vectors of control variables are

$$\boldsymbol{\phi}_n = \left[\phi_1(t_n), \cdots, \phi_{n_b}(t_n)\right]^T, \tag{4.43}$$

$$\boldsymbol{c}_n = \left[c_1(t_n), \cdots, c_{n_b}(t_n)\right]^T, \tag{4.44}$$

$$\boldsymbol{f}_n = \left[f_1(t_n), \cdots, f_{n_b}(t_n)\right]^T, \tag{4.45}$$

$$\boldsymbol{\sigma}_n = \left[\sigma_1(t_n), \cdots, \sigma_{n_b}(t_n)\right]^T, \tag{4.46}$$

that will form the solution vector $\mathbf{U}$ and the vector $\dot{\mathbf{U}}$

$$\mathbf{U}_n = \begin{bmatrix} \boldsymbol{\phi}_n \\ \boldsymbol{c}_n \\ \boldsymbol{f}_n \\ \boldsymbol{\sigma}_n \end{bmatrix}, \qquad \dot{\mathbf{U}}_n = \begin{bmatrix} \dot{\boldsymbol{\phi}}_n \\ \dot{\boldsymbol{c}}_n \\ \dot{\boldsymbol{f}}_n \\ \dot{\boldsymbol{\sigma}}_n \end{bmatrix}. \tag{4.47}$$

The residual vector are

$$\begin{aligned} \mathbf{R}(\dot{\mathbf{U}}_n, \mathbf{U}_n) &= \left\{ \mathbf{R}_A(N_A; \dot{\mathbf{U}}_n, \mathbf{U}_n) \right\}_{A=1,\cdots,n_b} \\ &= \left\{ \begin{bmatrix} R_A^{\phi}(N_A; \dot{\mathbf{U}}_n, \mathbf{U}_n) \\ R_A^{c}(N_A; \dot{\mathbf{U}}_n, \mathbf{U}_n) \\ R_A^{f}(N_A; \dot{\mathbf{U}}_n, \mathbf{U}_n) \\ R_A^{\sigma}(N_A; \dot{\mathbf{U}}_n, \mathbf{U}_n) \end{bmatrix} \right\}_{A=1,\cdots,n_b} \\ &= \left\{ \begin{bmatrix} R_A^{\phi} \\ R_A^{c} \\ R_A^{f} \\ R_A^{\sigma} \end{bmatrix} \right\}_{A=1,\cdots,n_b} \end{aligned} \tag{4.48}$$

and the residual for each field:

$$R_A^{\phi} = \left(N_A, \dot{\phi}_n^h\right)_{\Omega} + \left(\nabla N_A, M_{\phi}\lambda_{\phi}^2 \nabla \phi_n^h\right)_{\Omega} + \left(N_A, M_{\phi}\mu_{\phi}(\phi_n^h, \sigma_n^h)\right)_{\Omega}, \tag{4.49}$$

$$\begin{aligned} R_A^{c} = \left(N_A, \dot{c}_n^h\right)_{\Omega} &+ \left(\nabla N_A, M_c \nabla \mu_c(c_n^h)\right)_{\Omega} + \left(\Delta N_A, M_c \lambda_c^2 \Delta c_n^h\right)_{\Omega} - \\ &- \left(N_A, \mathcal{B}_p(f_n^h) c_n^h \mathcal{H}(c_n^h)\right)_{\Omega}, \end{aligned} \tag{4.50}$$

$$\begin{aligned} R_A^{f} = \left(N_A, \dot{f}_n^h\right)_{\Omega} &+ \left(\nabla N_A, D_f \nabla f_n^h\right)_{\Omega} - \left(N_A, \phi_n^h (1 - f_n^h)\mathcal{G}(\sigma_n^h)\right)_{\Omega} + \\ &+ \left(N_A, B_u f_n^h c_n^h \mathcal{H}(c_n^h)\right)_{\Omega}, \end{aligned} \tag{4.51}$$

$$\begin{aligned} R_A^{\sigma} = \left(N_A, \dot{\sigma}_n^h\right)_{\Omega} &+ \left(\nabla N_A, D_{\sigma} \nabla \sigma_n^h\right)_{\Omega} + \\ &+ \left(N_A, V_u^T \sigma_n^h \phi_n^h + V_u^H \sigma_n^h \mathcal{H}(1 - \phi_n^h) - V_p^c (1 - \sigma_n^h) c_n^h \mathcal{H}(c_n^h) \mathcal{S}\right)_{\Omega}. \end{aligned} \tag{4.52}$$

In the implementation a residual function is created for the assembly of the vector $\mathbf{R}(\dot{\mathbf{U}}_n, \mathbf{U}_n)$.

When we choose to use the generalized-α method, a new problem must be solved and can be described as follows:

Given $\dot{\mathbf{U}}_n, \mathbf{U}_n$ and Δt_n, find $\dot{\mathbf{U}}_{n+1}$ and $\mathbf{U}_{n+1}$ such that

$$\mathbf{R}(\dot{\mathbf{U}}_{n+\alpha_m}, \mathbf{U}_{n+\alpha_f}) = \mathbf{0}, \tag{4.53}$$

where

$$\dot{\mathbf{U}}_{n+\alpha_m} = \dot{\mathbf{U}}_n + \alpha_n \left(\dot{\mathbf{U}}_{n+1} - \dot{\mathbf{U}}_n\right), \tag{4.54}$$

$$\mathbf{U}_{n+\alpha_f} = \mathbf{U}_n + \alpha_f \left(\mathbf{U}_{n+1} - \mathbf{U}_n\right), \tag{4.55}$$

$$\mathbf{U}_{n+1} = \mathbf{U}_n + \Delta t_n \left(\gamma \dot{\mathbf{U}}_{n+1} + (1-\gamma)\dot{\mathbf{U}}_n\right) \tag{4.56}$$

and the parameters α_m, α_f and γ define the method,

$$\alpha_m = \frac{1}{2}\left(\frac{3-\rho_\infty}{1+\rho_\infty}\right), \tag{4.57}$$

$$\alpha_f = \frac{1}{1+\rho_\infty}, \tag{4.58}$$

$$\gamma = \frac{1}{2} + \alpha_m - \alpha_f, \tag{4.59}$$

the spectral radius $\rho_\infty \in [0, 1]$ (Chung and Hulbert, 1993).

In all experiments we used $\rho_\infty = 0.5$. The choice of $\rho_\infty = 0.5$, and consequently the values α_m , α_f and γ, guarantees the method a second-order accuracy and unconditional A-stability (Chung and Hulbert, 1993; Xu et al., 2016).

The system described in Eq. (4.53) is non-linear and the options of resolution methods in PetIGA/PETSc are varied. We chose to use Newton's method, which requires the specification of the Jacobian matrix of the system. One of the facilities of PetIGA/PETSc is the automatic generation of an approximate Jacobian matrix, and the user has to supply only the residue. We opted for the analytical derivation of the residue for the formulation of this matrix.

The adaptive time step used operates with the error estimate, which is based on the local truncation error, so for every step the algorithm verifies that the estimated local truncation error satisfies the tolerances provided by the user and computes a new step size to be taken (Balay et al., 2016). In all simulations performed here, we set $\Delta t = 10^{-11}$ the initial time step.

5 MECHANICAL MODEL

Mechanical models consider the laws of momentum and the energy balance to determine the movements of the components in response to the physical driving forces involved. In addition, the Clausius-Duhem inequality, in conjunction with Coleman-Noll argument, provides the constraints to find constitutive equations accounting for different mechanical responses. In our study, we consider all processes to be isothermal[1].

Our main references to describe a mechanical model of tumor growth are Oden et al. (2010) and Faghihi et al. (2018). Oden et al. (2010) present a broad theoretical study, providing a framework that attempts to generalize most of the models that describe tumor growth using mixture theory, and describing the interface through phase-field models. Faghihi et al. (2018), following same lines of Oden et al. (2010), incorporate the microforces balance law, introduced by Gurtin (1996), to this theory in order to justify in a thermodynamically consistent way the *ad hoc* interfacial terms introduced in Oden et al. (2010) to give rise to the phase-field models.

We organized this chapter as follows. In the first section, we present the forms of the constitutive equations for the specific materials involved in the model. In the second section, we present a model for four species and the related constitutive equations. Remarks on the mechanical model are presented in the last section.

5.1 Forms of constitutive equations

For the composition of our model, in addition to the mass balance and momentum equations for the constituents, we need the constitutive equations, which characterize the particularity of each specific component of the mixture. The first step is to determine the characteristic of the mixture components and to find which variables will be considered in the Helmholtz free energy composition.

Among the N constituents, we consider M solid constituents and $M - N$ fluid constituents. Solid constituents are considered, as in Oden et al. (2010): (i) heterogeneous isotropic – the material properties are independent of the direction (Reddy, 2013), (ii) hyperelastic materials – capable of undergoing large deformations. On the other hand, fluid constituents are considered heterogeneous, but pointwise isotropic (Oden et al., 2010).

The form adopted for Helmholtz free energy and the choice of its input variables have a huge influence on the associated constitutive equations. Faghihi et al. (2018) uses

[1] The temperature is constant and homogeneous.

the general form of Helmholtz free energy for the mixture

$$\Psi = \Psi(\mathbf{F}_1, ..., \mathbf{F}_N, \rho_1, ..., \rho_N, \phi_1, ..., \phi_N, \nabla\phi_1, ..., \nabla\phi_N, \mu_1, \ldots, \mu_N, \nabla\mu_1, \ldots, \nabla\mu_N) \quad (5.1)$$

considering that the energy initially depends on $\mathbf{F}_\alpha, \rho_\alpha, \phi_\alpha, \nabla\phi_\alpha, \mu_\alpha, \nabla\mu_\alpha$ for $1 \leqslant \alpha \leqslant N$. Oden et al. (2010), in turn, considers the energy of the constituent $\Psi_\alpha(\boldsymbol{\Lambda}_\alpha)$, where

$$\boldsymbol{\Lambda}_\alpha = \begin{cases} (X_\alpha;\ \theta, \nabla\theta, \mathbf{C}_\alpha, \phi_1, \cdots, \phi_N, \nabla\phi_1, \cdots, \nabla\phi_N, m_1\phi_\alpha, \cdots, m_L\phi_\alpha,) & \alpha \leqslant M, \\ (x_\alpha;\ \theta, \nabla\theta, \mathbf{F}_\alpha, \phi_1, \cdots, \phi_N, \nabla\phi_1, \cdots, \nabla\phi_N, m_1\phi_\alpha, \cdots, m_L\phi_\alpha,) & M < \alpha \leqslant N, \end{cases} \quad (5.2)$$

$\mathbf{C}_\alpha = \mathbf{F}_\alpha^T\mathbf{F}_\alpha$, and $m_\beta\phi_\alpha$ defines the reaction between various nutrients in the mixture and the constituent ϕ_α. This configuration uses reference position for solid constituents and spatial position for fluid constituents.

Here we adopt the general form of the free energy for each individual species

$$\Psi_\alpha = \Psi_\alpha(\mathbf{F}_\alpha, \rho_\alpha, \phi_1, ..., \phi_N, \nabla\phi_1, ..., \nabla\phi_N, \mu_\alpha, \nabla\mu_\alpha)\ . \quad (5.3)$$

The material time-derivative of Ψ_α using the chain rule can be written as

$$\frac{d^\alpha\Psi_\alpha}{dt} = \frac{\partial\Psi_\alpha}{\partial\mathbf{F}_\alpha} : \frac{d^\alpha\mathbf{F}_\alpha}{dt} + \frac{\partial\Psi_\alpha}{\partial\rho_\alpha}\frac{d^\alpha\rho_\alpha}{dt} + \sum_{\beta=1}^{N}\frac{\partial\Psi_\alpha}{\partial\phi_\beta}\frac{d^\alpha\phi_\beta}{dt} + \sum_{\beta=1}^{N}\frac{\partial\Psi_\alpha}{\partial(\nabla\phi_\beta)}\cdot\frac{d^\alpha(\nabla\phi_\beta)}{dt} + \frac{\partial\Psi_\alpha}{\partial\mu_\alpha}\frac{d^\alpha\mu_\alpha}{dt} + \frac{\partial\Psi_\alpha}{\partial(\nabla\mu_\alpha)}\cdot\frac{d^\alpha(\nabla\mu_\alpha)}{dt} \quad (5.4)$$

Aiming at an Eulerian treatment, we added in the model formulation an equation for the transport of the deformation gradient

$$\frac{\partial\mathbf{F}_\alpha}{\partial t} + \mathbf{v}_\alpha\cdot\nabla\mathbf{F}_\alpha = \nabla\mathbf{v}_\alpha\mathbf{F}_\alpha \quad (5.5)$$

$$\frac{d^\alpha\mathbf{F}_\alpha}{dt} = \nabla\mathbf{v}_\alpha\mathbf{F}_\alpha\ . \quad (5.6)$$

The choice of Lagrangian coordinates for the implementation of finite strain elastic deformation processes generally results in excessive grid distortion. The schemes used to eliminate these distortions are computationally expensive and, more importantly, inaccurate and complicated (Duddu et al., 2010).

In the first term of Eq. (5.4) we separate the terms containing the α^{th} term from the summation indexed by β, which yields

$$\frac{d^\alpha \Psi_\alpha}{dt} = \frac{\partial \Psi_\alpha}{\partial \mathbf{F}_\alpha} : \mathbf{L}_\alpha \mathbf{F}_\alpha + \frac{\partial \Psi_\alpha}{\partial \rho_\alpha}\frac{d^\alpha \rho_\alpha}{dt} + \frac{\partial \Psi_\alpha}{\partial \phi_\alpha}\frac{d^\alpha \phi_\alpha}{dt} + \sum_{\substack{\beta=1 \\ \beta\neq\alpha}}^{N} \frac{\partial \Psi_\alpha}{\partial \phi_\beta}\frac{d^\alpha \phi_\beta}{dt} + \frac{\partial \Psi_\alpha}{\partial (\nabla \phi_\alpha)} \cdot \frac{d^\alpha (\nabla \phi_\alpha)}{dt} + \sum_{\substack{\beta=1 \\ \beta\neq\alpha}}^{N} \frac{\partial \Psi_\alpha}{\partial (\nabla \phi_\beta)} \cdot \frac{d^\alpha (\nabla \phi_\beta)}{dt} + \frac{\partial \Psi_\alpha}{\partial \mu_\alpha}\frac{d^\alpha \mu_\alpha}{dt} + \frac{\partial \Psi_\alpha}{\partial (\nabla \mu_\alpha)} \cdot \frac{d^\alpha (\nabla \mu_\alpha)}{dt} \,. \tag{5.7}$$

Based on the choices generally used for Ψ_α, as in (Hawkins et al., 2011), (Lima et al., 2014) and (Faghihi et al., 2018), we consider $\dfrac{\partial \Psi_\alpha}{\partial \phi_\beta} = f_\alpha(\phi_\alpha)$ as a function of α only. Although it is a simplifying assumption, is the most used in the literature. This choice leads to

$$\sum_{\substack{\beta=1 \\ \beta\neq\alpha}}^{N} \frac{\partial \Psi_\alpha}{\partial \phi_\beta}\frac{d^\alpha \phi_\beta}{dt} = f_\alpha(\phi_\alpha) \sum_{\substack{\beta=1 \\ \beta\neq\alpha}}^{N} \frac{d^\alpha \phi_\beta}{dt} = f_\alpha(\phi_\alpha)\frac{d^\alpha}{dt}\left(\sum_{\substack{\beta=1 \\ \beta\neq\alpha}}^{N} \phi_\beta\right) = f_\alpha(\phi_\alpha)\frac{d^\alpha}{dt}(c - \phi_\alpha)$$

$$\sum_{\substack{\beta=1 \\ \beta\neq\alpha}}^{N} \frac{\partial \Psi_\alpha}{\partial \phi_\beta}\frac{d^\alpha \phi_\beta}{dt} = -f_\alpha(\phi_\alpha)\frac{d^\alpha \phi_\alpha}{dt} \tag{5.8}$$

where $\displaystyle\sum_{\beta=1,\beta\neq\alpha}^{N} \phi_\beta = 1 - \phi_\alpha$ is the saturation property of the mixture. Therefore,

$$\frac{d^\alpha \Psi_\alpha}{dt} = \frac{\partial \Psi_\alpha}{\partial \mathbf{F}_\alpha} : \mathbf{L}_\alpha \mathbf{F}_\alpha + \frac{\partial \Psi_\alpha}{\partial \rho_\alpha}\frac{d^\alpha \rho_\alpha}{dt} + \frac{\partial \Psi_\alpha}{\partial \phi_\alpha}\frac{d^\alpha \phi_\alpha}{dt} - f_\alpha(\phi_\alpha)\frac{d^\alpha \phi_\alpha}{dt} + \frac{\partial \Psi_\alpha}{\partial (\nabla \phi_\alpha)} \cdot \frac{d^\alpha (\nabla \phi_\alpha)}{dt} + \sum_{\substack{\beta=1 \\ \beta\neq\alpha}}^{N} \frac{\partial \Psi_\alpha}{\partial (\nabla \phi_\beta)} \cdot \frac{d^\alpha (\nabla \phi_\beta)}{dt} + \frac{\partial \Psi_\alpha}{\partial \mu_\alpha}\frac{d^\alpha \mu_\alpha}{dt} + \frac{\partial \Psi_\alpha}{\partial (\nabla \mu_\alpha)} \cdot \frac{d^\alpha (\nabla \mu_\alpha)}{dt} \,. \tag{5.9}$$

To obtain consistent relations between the constitutive functions, and the kinetic and thermodynamic variables that define the system, we must require Eq. (5.9) to satsfy the second law of thermodynamics for the mixture given in Eq. (2.103). Thus, replacing Eq. (5.9) in Eq. (2.103) we find

$$\sum_{\alpha}\Bigg\{-\frac{\partial\Psi_\alpha}{\partial\mathbf{F}_\alpha}\mathbf{F}_\alpha^T:\mathbf{L}_\alpha-\frac{\partial\Psi_\alpha}{\partial\rho_\alpha}\frac{d^\alpha\rho_\alpha}{dt}-\frac{\partial\Psi_\alpha}{\partial\phi_\alpha}\frac{d^\alpha\phi_\alpha}{dt}+f_\alpha(\phi_\alpha)\frac{d^\alpha\phi_\alpha}{dt}-\frac{\partial\Psi_\alpha}{\partial(\nabla\phi_\alpha)}\cdot\frac{d^\alpha(\nabla\phi_\alpha)}{dt}$$
$$-\sum_{\substack{\beta=1\\\beta\neq\alpha}}^{N}\frac{\partial\Psi_\alpha}{\partial(\nabla\phi_\beta)}\cdot\frac{d^\alpha(\nabla\phi_\beta)}{dt}-\frac{\partial\Psi_\alpha}{\partial\mu_\alpha}\frac{d^\alpha\mu_\alpha}{dt}-\frac{\partial\Psi_\alpha}{\partial(\nabla\mu_\alpha)}\cdot\frac{d^\alpha(\nabla\mu_\alpha)}{dt}-\Psi_\alpha\,\mathrm{tr}(\mathbf{L}_\alpha)$$
$$+\mathbf{T}_\alpha:\mathbf{D}_\alpha-\pi_\alpha\frac{d^\alpha\phi_\alpha}{dt}+\boldsymbol{\xi}_\alpha\cdot\nabla\left(\frac{d^\alpha\phi_\alpha}{dt}\right)+\mu_\alpha\frac{d^\alpha\rho_\alpha\phi_\alpha}{dt}$$
$$-\mathbf{J}_\alpha\cdot\nabla\mu_\alpha+\mu_\alpha\rho_\alpha\phi_\alpha\nabla\cdot\mathbf{v}_\alpha\Bigg\}\geqslant 0 \quad (5.10)$$

Oden et al. (2010) assume that the partial stresses for the fluid phases consist of the sum of an equilibrium stress $\mathbf{T}_\alpha^e$, which is characterized as that of a simple fluid, and a nonequilibrium thermoviscous stress $\mathbf{T}_\alpha^v$. In Faghihi et al. (2018), a similar decomposition occurs, with the partial Cauchy tensor written as the sum of an energetic part $\mathbf{T}_\alpha^{en}$ and a dissipative part $\mathbf{T}_\alpha^{dis}$. In this work we consider as in Faghihi et al. (2018)

$$\mathbf{T}_\alpha=\mathbf{T}_\alpha^{en}+\mathbf{T}_\alpha^{dis}\ . \quad (5.11)$$

Using the identity found in Oden et al. (2010),

$$\nabla\left(\frac{d^\alpha\phi_\alpha}{dt}\right)=\frac{d^\alpha(\nabla\phi_\alpha)}{dt}+\nabla\phi_\alpha\cdot\nabla\mathbf{v}_\alpha,$$
$$=\frac{d^\alpha(\nabla\phi_\alpha)}{dt}+\nabla\phi_\alpha\cdot\mathbf{L}_\alpha \quad (5.12)$$

we can rewrite the term

$$\boldsymbol{\xi}_\alpha\cdot\nabla\left(\frac{d^\alpha\phi_\alpha}{dt}\right)=\boldsymbol{\xi}_\alpha\cdot\left(\frac{d^\alpha(\nabla\phi_\alpha)}{dt}+\nabla\phi_\alpha\cdot\mathbf{L}_\alpha\right)=\boldsymbol{\xi}_\alpha\cdot\frac{d^\alpha(\nabla\phi_\alpha)}{dt}+(\boldsymbol{\xi}_\alpha\otimes\nabla\phi_\alpha):\mathbf{L}_\alpha\ . \quad (5.13)$$

Considering Eqs. (5.11), (5.13) and applying the product rule to the derivative $\dfrac{d^\alpha\rho_\alpha\phi_\alpha}{dt}$, we can rewrite

$$\sum_{\alpha}\Bigg\{-\frac{\partial\Psi_\alpha}{\partial\mathbf{F}_\alpha}\mathbf{F}_\alpha^T:\mathbf{L}_\alpha-\frac{\partial\Psi_\alpha}{\partial\rho_\alpha}\frac{d^\alpha\rho_\alpha}{dt}-\frac{\partial\Psi_\alpha}{\partial\phi_\alpha}\frac{d^\alpha\phi_\alpha}{dt}+f_\alpha(\phi_\alpha)\frac{d^\alpha\phi_\alpha}{dt}-\frac{\partial\Psi_\alpha}{\partial(\nabla\phi_\alpha)}\cdot\frac{d^\alpha(\nabla\phi_\alpha)}{dt}$$
$$-\sum_{\substack{\beta=1\\\beta\neq\alpha}}^{N}\frac{\partial\Psi_\alpha}{\partial(\nabla\phi_\beta)}\cdot\frac{d^\alpha(\nabla\phi_\beta)}{dt}-\frac{\partial\Psi_\alpha}{\partial\mu_\alpha}\frac{d^\alpha\mu_\alpha}{dt}-\frac{\partial\Psi_\alpha}{\partial(\nabla\mu_\alpha)}\cdot\frac{d^\alpha(\nabla\mu_\alpha)}{dt}-[\Psi_\alpha\mathbf{I}]:\mathbf{L}_\alpha$$
$$+\left[\mathbf{T}_\alpha^{en}+\mathbf{T}_\alpha^{dis}\right]:\mathbf{L}_\alpha-\pi_\alpha\frac{d^\alpha\phi_\alpha}{dt}+\boldsymbol{\xi}_\alpha\cdot\frac{d^\alpha(\nabla\phi_\alpha)}{dt}+(\boldsymbol{\xi}_\alpha\otimes\nabla\phi_\alpha):\mathbf{L}_\alpha$$
$$+\mu_\alpha\left(\rho_\alpha\frac{d^\alpha\phi_\alpha}{dt}+\phi_\alpha\frac{d^\alpha\rho_\alpha}{dt}\right)-\mathbf{J}_\alpha\cdot\nabla\mu_\alpha+\mu_\alpha\rho_\alpha\phi_\alpha\nabla\cdot\mathbf{v}_\alpha\Bigg\}\geqslant 0 \quad (5.14)$$

Some factors can be placed in evidence, resulting in

$$\sum_{\alpha}\Bigg\{\left(\mathbf{T}_{\alpha}^{en}-\Psi_{\alpha}\mathbf{I}-\frac{\partial\Psi_{\alpha}}{\partial\mathbf{F}_{\alpha}}\mathbf{F}_{\alpha}^{T}+\boldsymbol{\xi}_{\alpha}\otimes\nabla\phi_{\alpha}\right):\mathbf{L}_{\alpha}+\left(\mu_{\alpha}\rho_{\alpha}-\pi_{\alpha}-\frac{\partial\Psi_{\alpha}}{\partial\phi_{\alpha}}+f_{\alpha}(\phi_{\alpha})\right)\frac{d^{\alpha}\phi_{\alpha}}{dt}$$
$$+\left(\boldsymbol{\xi}_{\alpha}-\frac{\partial\Psi_{\alpha}}{\partial(\nabla\phi_{\alpha})}\right)\cdot\frac{d^{\alpha}(\nabla\phi_{\alpha})}{dt}+\left(\phi_{\alpha}\mu_{\alpha}-\frac{\partial\Psi_{\alpha}}{\partial\rho_{\alpha}}\right)\frac{d^{\alpha}\rho_{\alpha}}{dt}-\sum_{\substack{\beta=1\\\beta\neq\alpha}}^{N}\frac{\partial\Psi_{\alpha}}{\partial(\nabla\phi_{\beta})}\cdot\frac{d^{\alpha}(\nabla\phi_{\beta})}{dt}$$
$$-\frac{\partial\Psi_{\alpha}}{\partial(\nabla\mu_{\alpha})}\cdot\frac{d^{\alpha}(\nabla\mu_{\alpha})}{dt}-\frac{\partial\Psi_{\alpha}}{\partial\mu_{\alpha}}\frac{d^{\alpha}\mu_{\alpha}}{dt}+\mathbf{T}_{\alpha}^{dis}:\mathbf{L}_{\alpha}-\mathbf{J}_{\alpha}\cdot\nabla\mu_{\alpha}$$
$$+\mu_{\alpha}\rho_{\alpha}\phi_{\alpha}\nabla\cdot\mathbf{v}_{\alpha}\Bigg\}\geqslant 0 \tag{5.15}$$

Only constitutive equations that are consistent with the second law of thermodynamics in all processes are considered physically viable (Gurtin et al., 2010). For this, we invoke the classic Coleman-Noll procedure (Coleman and Noll, 1964), eliminating terms that can vary arbitrarily and compromise inequality (5.15). Gurtin (1996) clarifies that this may seem artificial, but it is no more artificial than theories based on virtual work or minimum "energy", as these require arbitrary variations of the fields, even though such variations are generally inconsistent with the resulting balance laws. When using the Coleman-Noll procedure, considering some coefficients of (5.15) equal to zero, we obtain the following thermodynamic restrictions

$$\mathbf{T}_{\alpha}^{en}=\frac{\partial\Psi_{\alpha}}{\partial\mathbf{F}_{\alpha}}\mathbf{F}_{\alpha}^{T}-\boldsymbol{\xi}_{\alpha}\otimes\nabla\phi_{\alpha}+\Psi_{\alpha}\mathbf{I}, \tag{5.16}$$
$$\mu_{\alpha}\rho_{\alpha}=\pi_{\alpha}+\frac{\partial\Psi_{\alpha}}{\partial\phi_{\alpha}}-f_{\alpha}(\phi_{\alpha}), \tag{5.17}$$
$$\boldsymbol{\xi}_{\alpha}=\frac{\partial\Psi_{\alpha}}{\partial\left(\nabla\phi_{\alpha}\right)}, \tag{5.18}$$
$$\frac{\partial\Psi_{\alpha}}{\partial\rho_{\alpha}}=\phi_{\alpha}\mu_{\alpha}, \tag{5.19}$$

$$\frac{\partial\Psi_{\alpha}}{\partial(\nabla\phi_{\beta})}=\mathbf{0}\qquad(\alpha\neq\beta), \tag{5.20}$$
$$\frac{\partial\Psi_{\alpha}}{\partial(\nabla\mu_{\alpha})}=\mathbf{0}, \tag{5.21}$$
$$\frac{\partial\Psi_{\alpha}}{\partial\mu_{\alpha}}=0. \tag{5.22}$$

From Eqs. (5.17) and (2.53), we can write

$$\rho_{\alpha}\mu_{\alpha}=\frac{\partial\Psi_{\alpha}}{\partial\phi_{\alpha}}-\nabla\cdot\boldsymbol{\xi}_{\alpha}-\tau_{\alpha}-f_{\alpha}(\phi_{\alpha})\ . \tag{5.23}$$

With those restrictions, we find out that Ψ_α is independent of μ, $\nabla\mu$ and $\nabla\phi_\beta$, for $\beta \neq \alpha$, and takes the form

$$\Psi_\alpha = \Psi_\alpha(\mathbf{F}_\alpha, \rho_\alpha, \phi_1, ..., \phi_N, \nabla\phi_\alpha) \ . \tag{5.24}$$

Some of the energy dissipates and is described as

$$\begin{aligned} D &= \sum_\alpha \left\{ \mu_\alpha \rho_\alpha \phi_\alpha \nabla \cdot \mathbf{v}_\alpha + \mathbf{T}_\alpha^{dis} : \mathbf{D}_\alpha - \mathbf{J}_\alpha \cdot \nabla\mu_\alpha \right\} \geqslant 0 \\ &= \sum_\alpha \left\{ \mu_\alpha \rho_\alpha \phi_\alpha \mathbf{I} : \mathbf{D}_\alpha + \mathbf{T}_\alpha^{dis} : \mathbf{D}_\alpha - \mathbf{J}_\alpha \cdot \nabla\mu_\alpha \right\} \geqslant 0, \end{aligned} \tag{5.25}$$

$$\frac{\partial D}{\partial \mathbf{D}_\alpha} = \mathbf{T}_\alpha^{dis} + \mu_\alpha \rho_\alpha \phi_\alpha \mathbf{I}, \tag{5.26}$$

$$\frac{\partial D}{\partial \nabla\mu_\alpha} = -\mathbf{J}_\alpha. \tag{5.27}$$

In Faghihi et al. (2018), dissipative terms are divided into two types, those resulting from viscosity, reserved for constituents of fluids, and those resulting from diffusion, i.e.,

$$D = D^{vis} + D^{diff} = \sum_{\alpha=M+1}^{N} \frac{1}{2} A_\alpha |\mathbf{D}_\alpha|^2 + \sum_{\alpha=1}^{N} \nabla\mu_\alpha \cdot \mathbf{M}_\alpha \nabla\mu_\alpha. \tag{5.28}$$

where A_α is the shear viscosity of fluid species, μ_α is the chemical potential and $\mathbf{M}_\alpha$ is the positive semi-definite[2] mobility tensor. The term describing diffusion dissipation is also used by Gurtin (1996) in the formulation of Generalized Cahn-Hilliard equations.

With this formulation we have

$$\mathbf{T}_\alpha^{dis} = A_\alpha \mathbf{D}_\alpha - \mu_\alpha \rho_\alpha \phi_\alpha \mathbf{I}, \tag{5.29}$$

$$\mathbf{J}_\alpha = -\mathbf{M}_\alpha \nabla\mu_\alpha \ . \tag{5.30}$$

5.1.1 Cauchy tensor

In addition to separating the Cauchy tensor into solid and fluid components the tensor

$$\mathbf{T}_\alpha = \begin{cases} \mathbf{T}_\alpha^{en}, & \alpha \leqslant M, \\ \mathbf{T}_\alpha^{en} + \mathbf{T}_\alpha^{dis}, & M < \alpha \leqslant N, \end{cases} \tag{5.31}$$

can be written according to the particular properties of these components. An important property about the derivation of scalar functions of a tensor variable is presented in (Gurtin et al., 2010), and here we present it as the following proposition:

[2] $w^T M w \geqslant 0, \ \forall w \in R^n$

Proposition 1. *Let H be defined on the space of symmetric tensors, and consider the function $h(\mathbf{F})$ defined on the space of all tensors through the requirement that $H(\mathbf{C}) = H(\mathbf{F}^T\mathbf{F}) = H(f(\mathbf{F})) = h(\mathbf{F})$ for all tensors $\mathbf{F}$, then*

$$2\mathbf{F}\frac{\partial H(\mathbf{C})}{\partial \mathbf{C}} = \frac{\partial h(\mathbf{F})}{\partial \mathbf{F}} \tag{5.32}$$

The mechanical part of the tensor

$$\mathbf{T}_\alpha^{en} = \frac{\partial \Psi_\alpha}{\partial \mathbf{F}_\alpha}\mathbf{F}_\alpha^T - \boldsymbol{\xi}_\alpha \otimes \nabla\phi_\alpha + \Psi_\alpha \mathbf{I} \tag{5.33}$$

will be denoted by

$$\hat{\mathbf{T}}_\alpha^{en} = \frac{\partial \Psi_\alpha}{\partial \mathbf{F}_\alpha}\mathbf{F}_\alpha^T \ . \tag{5.34}$$

Mechanical part of the $\mathbf{T}_\alpha^{en}$ tensor for the solid components of the mixture

For the solid part of the mixture, $\alpha \leqslant M$, we can write $\hat{\mathbf{T}}_\alpha^{en}$ as a function of Piola-Kirchhoff second partial tensor, $\mathbf{S}_\alpha$, by the relation

$$\hat{\mathbf{T}}_\alpha^{en} = \frac{1}{\det(\mathbf{F}_\alpha)}\mathbf{F}_\alpha \mathbf{S}_\alpha \mathbf{F}_\alpha^T \tag{5.35}$$

where

$$\mathbf{S}_\alpha = \det(\mathbf{F}_\alpha)\mathbf{F}_\alpha^{-1}\hat{\mathbf{T}}_\alpha^{en}\mathbf{F}_\alpha^{-T} \ . \tag{5.36}$$

Using Eq. (5.32), we can rewrite Eq. (5.34) of the form

$$\hat{\mathbf{T}}_\alpha^{en} = 2\mathbf{F}_\alpha \frac{\partial \Psi_\alpha}{\partial \mathbf{C}_\alpha}\mathbf{F}_\alpha^T \ , \tag{5.37}$$

and considering that the portion of energy Ψ_α that depends on $\mathbf{C}_\alpha$ is the portion Ψ_α^{els}, we have

$$\hat{\mathbf{T}}_\alpha^{en} = 2\mathbf{F}_\alpha \frac{\partial \Psi_\alpha^{els}}{\partial \mathbf{C}_\alpha}\mathbf{F}_\alpha^T. \tag{5.38}$$

The isotropic elastic properties of a hyperelastic material model can be described in terms of a scalar function W, called strain-energy or stored-energy (Hackett, 2016). According to Belytschko et al. (2014), hyperelastic materials are characterized by the relation

$$\mathbf{S}_\alpha = 2\frac{\partial W_\alpha}{\partial \mathbf{C}_\alpha} \tag{5.39}$$

where $W_\alpha = W_\alpha(\mathbf{C}_\alpha, \phi_\alpha)$ is a strain energy related to the α constituent. We consider $W_\alpha = \hat{\rho}_{\alpha_0}\psi_\alpha$, as in (Oden et al., 2010) and (Ateshian and Humphrey, 2012).

Noting that $W_\alpha = W_\alpha(\mathbf{C}_\alpha, \phi_\alpha) = W_\alpha(\mathbf{F}_\alpha^T\mathbf{F}_\alpha, \phi_\alpha) = W_\alpha(f(\mathbf{F}_\alpha), \phi_\alpha)$ and using Eq. (5.32), a relationship between the derivatives of W_α with respect to $\mathbf{C}_\alpha$ and $\mathbf{F}_\alpha$ is given by

$$2\frac{\partial W_\alpha}{\partial \mathbf{C}_\alpha} = (\mathbf{F}_\alpha)^{-1}\frac{\partial W_\alpha}{\partial \mathbf{F}_\alpha} \ , \tag{5.40}$$

thus,

$$\mathbf{S}_\alpha = (\mathbf{F}_\alpha)^{-1}\frac{\partial W_\alpha}{\partial \mathbf{F}_\alpha} \ . \tag{5.41}$$

Replacing Eq. (5.41) in Eq. (5.35) we can write

$$\begin{aligned}\hat{\mathbf{T}}^{en}_\alpha &= \frac{1}{\det(\mathbf{F}_\alpha)}\mathbf{F}_\alpha\left((\mathbf{F}_\alpha)^{-1}\frac{\partial W_\alpha}{\partial \mathbf{F}_\alpha}\right)\mathbf{F}^T_\alpha \\ &= \frac{1}{\det(\mathbf{F}_\alpha)}\left(\frac{\partial W_\alpha}{\partial \mathbf{F}_\alpha}\right)\mathbf{F}^T_\alpha \ .\end{aligned} \tag{5.42}$$

Mechanical part of the $\mathbf{T}^{en}_\alpha$ tensor for the fluid components of the mixture

For the fluid components, $M < \alpha \leqslant N$, we have

$$\hat{\mathbf{T}}^{en}_\alpha = \frac{\partial \Psi^{els}_\alpha}{\partial \mathbf{F}_\alpha}\mathbf{F}^T_\alpha = -p_\alpha \mathbf{I} \ , \tag{5.43}$$

where p is the thermodynamic pressure

$$p = -\hat{\rho}^2_\alpha \frac{\partial \psi_\alpha}{\partial \hat{\rho}}, \tag{5.44}$$

as presented in (Oden et al., 2010) and (Faghihi et al., 2018).

Cauchy tensor for the mixture

For the αth constituent of the mixture, the tensor $\hat{\mathbf{T}}^{en}_\alpha$ is determined by Eqs. (5.42) and (5.43) as

$$\hat{\mathbf{T}}^{en}_\alpha = \begin{cases} \dfrac{1}{\det(\mathbf{F}_\alpha)}\dfrac{\partial W_\alpha}{\partial \mathbf{F}_\alpha}\mathbf{F}^T_\alpha \ , & \alpha \leqslant M, \\ -p_\alpha \mathbf{I}, & M < \alpha \leqslant N, \end{cases} \tag{5.45}$$

and replacing (5.45) in (5.33), we have

$$\mathbf{T}^{en}_\alpha = \begin{cases} \dfrac{1}{\det(\mathbf{F}_\alpha)}\dfrac{\partial W_\alpha}{\partial \mathbf{F}_\alpha}\mathbf{F}^T_\alpha & -\boldsymbol{\xi}_\alpha \otimes \nabla\phi_\alpha + \Psi_\alpha \mathbf{I}, \quad \alpha \leqslant M, \\ -p_\alpha \mathbf{I} & -\boldsymbol{\xi}_\alpha \otimes \nabla\phi_\alpha + \Psi_\alpha \mathbf{I}, \quad M < \alpha \leqslant N, \end{cases} \tag{5.46}$$

that can be rewritten as

$$\mathbf{T}^{en}_\alpha = \begin{cases} \dfrac{1}{\det(\mathbf{F}_\alpha)}\dfrac{\partial W_\alpha}{\partial \mathbf{F}_\alpha}\mathbf{F}^T_\alpha & -\boldsymbol{\xi}_\alpha \otimes \nabla\phi_\alpha + \Psi_\alpha \mathbf{I}, \quad \alpha \leqslant M, \\ (\Psi_\alpha - p_\alpha)\mathbf{I} & -\boldsymbol{\xi}_\alpha \otimes \nabla\phi_\alpha, \quad M < \alpha \leqslant N, \end{cases} \tag{5.47}$$

where the difference $\Psi_\alpha - p_\alpha$ is called the *hydrostatic pressure* (Oden et al., 2010).

The dissipative part $\mathbf{T}^{dis}_\alpha$ of the Cauchy tensor $\mathbf{T}_\alpha$ will be given by Eq. (5.29), thus completing the tensor

$$\mathbf{T}_\alpha = \begin{cases} \mathbf{T}^{en}_\alpha, & \alpha \leqslant M, \\ \mathbf{T}^{en}_\alpha + \mathbf{T}^{dis}_\alpha, & M < \alpha \leqslant N, \end{cases}$$

thus

$$\mathbf{T}_\alpha = \begin{cases} \dfrac{1}{\det(\mathbf{F}_\alpha)} \dfrac{\partial W_\alpha}{\partial \mathbf{F}_\alpha} \mathbf{F}_\alpha^T - \boldsymbol{\xi}_\alpha \otimes \nabla \phi_\alpha + \Psi_\alpha \mathbf{I}, & \alpha \leqslant M, \\ (\Psi_\alpha - p_\alpha)\mathbf{I} - \boldsymbol{\xi}_\alpha \otimes \nabla \phi_\alpha + A_\alpha \mathbf{D}_\alpha - \mu_\alpha \rho_\alpha \phi_\alpha \mathbf{I}, & M < \alpha \leqslant N. \end{cases} \tag{5.48}$$

5.1.2 Constraint of the constitutive equations to a four species model

From now on we consider the model composed by 4 species: tumor cells ϕ_T, healthy cells ϕ_C, nutrient-rich extracellular fluid ϕ_σ and nutrient poor extracellular fluid ϕ_{σ_0}, that also were considered by Oden et al. (2010) and Faghihi et al. (2018). In the model, the total concentration of liquid components, and also the total concentration of solid components, remain constant throughout the domain, i.e., $\phi_\sigma + \phi_{\sigma_0} = s$ and $\phi_T + \phi_C = w$. Thus, the saturation condition of the mixture can be written as $s + w = c$.

5.1.3 Free energy

The free energy of the αth constituent will be given by the sum

$$\Psi_\alpha = \Psi_\alpha^{els} + \Psi_\alpha^{chm} + \Psi_\alpha^{int} + \Psi_\alpha^{taxis}, \tag{5.49}$$

where Ψ_α^{els} is the elastic energy, Ψ_α^{chm} is the chemical energy, Ψ_α^{int} is the interfacial energy, and Ψ_α^{taxis} is the energy due to taxis-inducing chemical and molecular species (Faghihi et al., 2018). Considering the following energies for the tumor

$$\Psi_T^{chm}(\phi_T) = \kappa \phi_T^2 (1 - \phi_T)^2, \tag{5.50}$$

$$\Psi_T^{int}(\nabla \phi_T) = \frac{\epsilon}{2} |\nabla \phi_T|^2, \tag{5.51}$$

$$\Psi_T^{taxis}(\phi_T, \phi_\sigma) = -\chi \phi_T \phi_\sigma, \tag{5.52}$$

and for the nutrients

$$\Psi_\sigma^{chm}(\phi_\sigma) = \frac{1}{2\delta_\sigma} \phi_\sigma^2, \tag{5.53}$$

$$\Psi_\sigma^{int}(\nabla \phi_\sigma) = 0, \tag{5.54}$$

$$\Psi_\sigma^{taxis}(\phi_T, \phi_\sigma) = -\chi \phi_T \phi_\sigma \ . \tag{5.55}$$

From Eqs. (5.18) and (5.51) the micro stress energy for the tumor will be

$$\boldsymbol{\xi}_T = \frac{\partial \Psi_T}{\partial (\nabla \phi_T)} = \frac{\partial \Psi_T^{int}}{\partial (\nabla \phi_T)} = \frac{\partial \left[\frac{\epsilon}{2} |\nabla \phi_T|^2 \right]}{\partial (\nabla \phi_T)} = \epsilon \nabla \phi_T \ . \tag{5.56}$$

5.1.4 The multiplicative decomposition of the deformation gradient

The multiplicative decomposition of the deformation gradient was established in the plasticity theory (Lee, 1969), but only in Rodriguez et al. (1994) it was applied to describe

the volumetric growth of biological tissues. Several authors have used the multiplicative decomposition of the deformation gradient to describe the biological growth (Taber, 2008; Ambrosi et al., 2010) and tumor growth (Mpekris et al., 2015; Ambrosi and Mollica, 2002). We use here the decomposition as presented in Faghihi et al. (2018):

$$\mathbf{F}_T = \mathbf{F}_T^S \mathbf{F}_T^G, \tag{5.57}$$

where the growth tensor $\mathbf{F}_T^G$ describes the mass change, and the elastic deformation tensor $\mathbf{F}_T^S$ describes the mechanical interaction with other constituents. Figure 5.1 attempts to describe the action of tensors $\mathbf{F}_T^G$ and $\mathbf{F}_T^S$ on body $\boldsymbol{B}$.

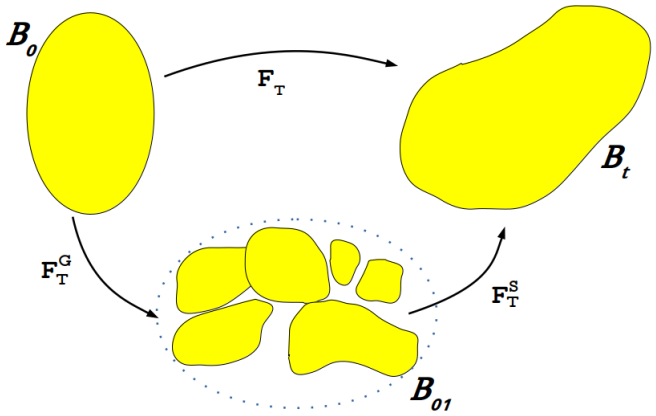

Figure 5.1 – The reference body $\boldsymbol{B}_0$, intermediate state $\boldsymbol{B_{01}}$, and deformed body $\boldsymbol{B}_t$. Figure inspired by (Rodriguez et al., 1994).

The growth tensor $\mathbf{F}_T^G$ causes the tissue to expand locally, resulting in a hypothetical unstressed intermediate state $\boldsymbol{B_{01}}$. The elastic deformation $\mathbf{F}_T^S$ then corrects the growth tensor to ensure the integrity of the material. The accumulation of internal stress results from the correction performed by $\mathbf{F}_T^S$ (MacLaurin et al., 2012). The tensor $\mathbf{F}_T^G$ is not compatible in the sense that it is not the gradient of a vector field. Compatibility of $\mathbf{F}$, however, is guaranteed by its definition. In this sense $\mathbf{F}_T^S$ is a "compatibility-restoring" field but is itself incompatible (Garikipati, 2009). Therefore, incompatible growth fields lead to residual stress that arises as a direct result of the elastic deformations required to maintain continuity of the body (Rodriguez et al., 1994).

Using Eq. (5.56), the Cauchy tensor for the tumor takes the following form

$$\mathbf{T}_T = \frac{1}{\det(\mathbf{F}_T)} \frac{\partial W_T}{\partial \mathbf{F}_T} \mathbf{F}_T^T - \epsilon \nabla \phi_T \otimes \nabla \phi_T + \Psi_T \mathbf{I}, \tag{5.58}$$

and considering the decomposition in Eq. (5.57), the derivation of W_T as a function of $\mathbf{F}_T^S$ gives us a new face for the tensor defined in Eq. (5.58)

$$\begin{aligned}\mathbf{T}_T &= \frac{1}{\det(\mathbf{F}_T^S\mathbf{F}_T^G)}\frac{\partial W_T}{\partial \mathbf{F}_T^S}(\mathbf{F}_T^G)^{-T}\mathbf{F}_T^T - \epsilon\nabla\phi_T\otimes\nabla\phi_T \ + \Psi_T\mathbf{I}\\ &= \frac{1}{\det(\mathbf{F}_T^S)\det(\mathbf{F}_T^G)}\frac{\partial W_T}{\partial \mathbf{F}_T^S}(\mathbf{F}_T^G)^{-T}\left(\mathbf{F}_T^S\mathbf{F}_T^G\right)^T - \epsilon\nabla\phi_T\otimes\nabla\phi_T \ + \Psi_T\mathbf{I}\\ &= \frac{1}{\det(\mathbf{F}_T^S)\det(\mathbf{F}_T^G)}\frac{\partial W_T}{\partial \mathbf{F}_T^S}(\mathbf{F}_T^G)^{-T}\left(\mathbf{F}_T^G\right)^T\left(\mathbf{F}_T^S\right)^T - \epsilon\nabla\phi_T\otimes\nabla\phi_T \ + \Psi_T\mathbf{I}\\ &= \frac{1}{\det(\mathbf{F}_T^S)\det(\mathbf{F}_T^G)}\frac{\partial W_T}{\partial \mathbf{F}_T^S}\left(\mathbf{F}_T^S\right)^T - \epsilon\nabla\phi_T\otimes\nabla\phi_T \ + \Psi_T\mathbf{I}. \end{aligned} \tag{5.59}$$

The incorporation of Eq. (5.5) in the system allows the full description of $\mathbf{F}_T$, but when using the multiplicative decomposition described in Eq. (5.57), the description of $\mathbf{F}_T^S$ and $\mathbf{F}_T^G$ is no longer possible. To circumvent this difficulty, $\mathbf{F}_T^G$ can be described in a purely phenomenological way or by including it as a new degree of freedom in the problem (Ambrosi et al., 2010).

5.1.5 Strain energy function

There are a variety of strain-energy formulations, each trying to describe characteristics and properties of distinct elastic materials. According to Chagnon et al. (2017) most strain energy functions were not developed for soft tissues, but for rubber-like materials. Soft tissues often present a larger strain hardening than rubber-like materials. Among the most commonly used formulations for biological tissues are the Blatz–Ko and Neo-Hookean models (Jain et al., 2014). Following (Faghihi et al., 2018), we use the compressible Neo-Hookean model, given by

$$W = \frac{G_T}{2}(\bar{I}_C^S - 3) + \frac{K_T}{2}(J_T^S - 1)^2, \tag{5.60}$$

where K_T and G_T are shear and bulk modulus, and

$$\begin{aligned} J_T^S &= \sqrt{\det[\mathbf{C}_T^S]} = \sqrt{\det[(\mathbf{F}_T^S)^T\mathbf{F}_T^S]} = \sqrt{\det[(\mathbf{F}_T^S)^T]\det[\mathbf{F}_T^S]}\\ &= \sqrt{\det[\mathbf{F}_T^S]\det[\mathbf{F}_T^S]} = \sqrt{(\det[\mathbf{F}_T^S])^2} = \det[\mathbf{F}_T^S], \end{aligned} \tag{5.61}$$

$$\bar{I}_C^S = (J_T^S)^{-\frac{2}{3}}\,\mathrm{tr}[C_T^S] = (J_T^S)^{-\frac{2}{3}}\,\mathrm{tr}[(\mathbf{F}_T^S)^T\mathbf{F}_T^S]\ . \tag{5.62}$$

We also consider $J_T^G = \det[\mathbf{F}_T^G]$, to simplify the notation. Substituting the strain-energy Eq. (5.60) in Eq. (5.59) we find the Cauchy tensor shape for the solid part of the tumor.

Proposition 2. *Given the Neo-Hookean strain energy function (5.60), the Cauchy tensor to the solid constituents will be*

$$\mathbf{T}_T = \frac{1}{J_T^G}\left\{\frac{G_T}{(J_T^S)^{\frac{5}{3}}}\left[\mathbf{B}_T^S - \frac{1}{3}\,\mathrm{tr}[\mathbf{B}_T^S]\mathbf{I}\right] + K_T(J_T^S - 1)\mathbf{I}\right\} - \epsilon\nabla\phi_T \otimes \nabla\phi_T \quad + \Psi_T\mathbf{I} \tag{5.63}$$

where $\mathbf{B}_T^S = \mathbf{F}_T^S(\mathbf{F}_T^S)^T$.

The demonstration of the Prop. 2 is shown in Appendix A.1.

For two-dimensional experiments we use the following Neo-Hookean version

$$W_2 = \frac{G_T}{2}(\bar{\bar{I}}_C^S - 2) + \frac{K_T}{2}(J_T^S - 1)^2, \tag{5.64}$$

where

$$\bar{\bar{I}}_C^S = (J_T^S)^{-1}\,\mathrm{tr}[\mathbf{C}_T^S] = (J_T^S)^{-1}\,\mathrm{tr}[(\mathbf{F}_T^S)^T\mathbf{F}_T^S], \tag{5.65}$$

and the tensor is defined as

$$\mathbf{T}_T = \frac{1}{J_T^G}\left[\frac{G_T}{(J_T^S)^2}\left[\mathbf{B}_T^S - \frac{1}{2}\,\mathrm{tr}[\mathbf{B}_T^S]\mathbf{I}\right] + K_T(J_T^S - 1)\mathbf{I}\right] - \epsilon\nabla\phi_T \otimes \nabla\phi_T + \Psi_T\mathbf{I}. \tag{5.66}$$

5.1.6 Chemical potential

The free energy given in Eq. (5.23) together with Eq. (5.49) gives us a general expression for the chemical potential for the α constituent:

$$\rho_\alpha\mu_\alpha = \frac{\partial\Psi_\alpha^{els}}{\partial\phi_\alpha} + \frac{\partial\Psi_\alpha^{chm}}{\partial\phi_\alpha} + \frac{\partial\Psi_\alpha^{taxis}}{\partial\phi_\alpha} + \frac{\partial\Psi_\alpha^{int}}{\partial\phi_\alpha} - \nabla\cdot\boldsymbol{\xi}_\alpha - \tau_\alpha - f_\alpha(\phi_\alpha)\ , \tag{5.67}$$

and for the tumor phase we have

$$\rho_T\mu_T = \frac{\partial\Psi_T^{els}}{\partial\phi_T} + \frac{\partial\Psi_T^{chm}}{\partial\phi_T} + \frac{\partial\Psi_T^{taxis}}{\partial\phi_T} + \frac{\partial\Psi_T^{int}}{\partial\phi_T} - \nabla\cdot\boldsymbol{\xi}_T - \tau_T - \frac{\partial\Psi_T}{\partial\phi_\sigma}\ . \tag{5.68}$$

Using Eq. (5.56) we can write

$$\nabla\cdot\boldsymbol{\xi}_T = \epsilon\Delta\phi_T. \tag{5.69}$$

Considering the definitions on Eqs. (5.50), (5.51), and (5.52), some derivatives present in Eq. (5.68) can be defined as

$$\frac{\partial\Psi_T^{chm}}{\partial\phi_T} = 2\kappa\phi_T(2\phi_T^2 - 3\phi_T + 1) \tag{5.70}$$

$$\frac{\partial\Psi_T^{taxis}}{\partial\phi_T} = -\chi\phi_\sigma \tag{5.71}$$

$$\frac{\partial\Psi_T^{int}}{\partial\phi_T} = 0 \tag{5.72}$$

$$\frac{\partial\Psi_T}{\partial\phi_\sigma} = \frac{\partial\Psi_T^{taxis}}{\partial\phi_\sigma} = -\chi\phi_T\ . \tag{5.73}$$

Applying the chain rule to the Ψ_T^{els} function and considering the deformation gradient decomposition:

$$\frac{\partial \Psi_T^{els}}{\partial \phi_T} = \frac{\partial \Lambda_T^G}{\partial \phi_T}\left(\hat{\mathbf{T}}_T^{en}\mathbf{F}_T^{-T} : \mathbf{F}_T^S\right). \tag{5.74}$$

The demonstration of Eq. (5.74) is shown in Appendix A.2. Thus, the chemical potential for the tumor will be

$$\rho_T\mu_T = \frac{\partial \Lambda_T^G}{\partial \phi_T}\left(\hat{\mathbf{T}}_T^{en}\mathbf{F}_T^{-T} : \mathbf{F}_T^S\right) + 2\kappa\phi_T(2\phi_T^2 - 3\phi_T + 1) - \chi\phi_\sigma - \epsilon\Delta\phi_T - \tau_T + \chi\phi_T. \tag{5.75}$$

From the general expression

$$\rho_\sigma\mu_\sigma = \frac{\partial \Psi_\sigma^{els}}{\partial \phi_\sigma} + \frac{\partial \Psi_\sigma^{chm}}{\partial \phi_\sigma} + \frac{\partial \Psi_\sigma^{taxis}}{\partial \phi_\sigma} + \frac{\partial \Psi_\sigma^{int}}{\partial \phi_\sigma} - \nabla\cdot\boldsymbol{\xi}_\sigma - \tau_\sigma - \frac{\partial \Psi_\sigma}{\partial \phi_T} \tag{5.76}$$

and

$$\frac{\partial \Psi_\sigma^{els}}{\partial \phi_\sigma} = 0 \tag{5.77}$$

$$\frac{\partial \Psi_\sigma^{chm}}{\partial \phi_\sigma} = \frac{1}{\delta_\sigma}\phi_\sigma \tag{5.78}$$

$$\frac{\partial \Psi_\sigma^{taxis}}{\partial \phi_\sigma} = -\chi\phi_T \tag{5.79}$$

$$\frac{\partial \Psi_\sigma^{int}}{\partial \phi_\sigma} = 0 \tag{5.80}$$

$$\frac{\partial \Psi_\sigma}{\partial \phi_T} = \frac{\partial \Psi_\sigma^{taxis}}{\partial \phi_T} = -\chi\phi_\sigma \tag{5.81}$$

we have the chemical potential for the nutrient

$$\rho_\sigma\mu_\sigma = \frac{1}{\delta_\sigma}\phi_\sigma - \chi\phi_T - \tau_\sigma + \chi\phi_\sigma\ . \tag{5.82}$$

Neglecting the external microforce in Eq. (5.75) and (5.82) we can writen

$$\rho_T\mu_T = \frac{\partial \Lambda_T^G}{\partial \phi_T}\left(\hat{\mathbf{T}}_T^{en}\mathbf{F}_T^{-T} : \mathbf{F}_T^S\right) + 2\kappa\phi_T(2\phi_T^2 - 3\phi_T + 1) - \chi\phi_\sigma - \epsilon\Delta\phi_T + \chi\phi_T \tag{5.83}$$

$$\rho_\sigma\mu_\sigma = \frac{1}{\delta_\sigma}\phi_\sigma - \chi\phi_T + \chi\phi_\sigma\ . \tag{5.84}$$

5.1.7 Other constitutive relations: mass flow, mobility, mass exchange and $\mathbf{F}^G$

Based on (5.24) we postulate that the mass flow depends on $\mathbf{F}_T, \phi_T$ and $\nabla\mu_T$

$$\mathbf{J}_T = \mathbf{J}_T(\mathbf{F}_T, \phi_T, \nabla\mu_T). \tag{5.85}$$

Using the principle of indifference, Faghihi et al. (2018) shows that the mass flow can also be written as a function of $\mathbf{C}_T, \phi_T$ and $\nabla\mu_T$

$$\mathbf{J}_T = \mathbf{J}_T(\mathbf{C}_T, \phi_T, \nabla\mu_T) \ . \tag{5.86}$$

Equations (5.30) and (5.86) indicate that tumor mobility is a tensor function that depends on $\mathbf{C}_T$ and ϕ_T

$$\mathbf{M}_T = \mathbf{M}_T(\mathbf{C}_T, \phi_T)$$

which is written by Faghihi et al. (2018) as

$$\mathbf{M}_T(\mathbf{C}_T, \phi_T) = M_T(\mathbf{C}_T, \phi_T)\mathbf{I} = \lambda_T^{mob}\phi_T^2(1-\phi_T)^2\mathbf{I} \ , \tag{5.87}$$

where λ_T^{mob} is an exponential decay that simulates the effects of tumor growth/deformation, generating greater resistance of the surrounding tissue,

$$\lambda_T^{mob} = \alpha_T^{mob} exp[-\gamma_T^{mob} J_T] = \alpha_T^{mob} exp[-\gamma_T^{mob}\sqrt{\det(C_T)}]$$

with α_T^{mob} and γ_T^{mob} constant.

An exponential decay was also used to form tumor mobility in Weis et al. (2013) and Lima et al. (2016), but using Von Mises stress as a metric of energy instead of J_T.

The nutrient mobility can be express as

$$\mathbf{M}_\sigma = \frac{1}{\delta_\sigma} M_\sigma \mathbf{I} \ , \tag{5.88}$$

where M_σ is a constant describing the mobility of extracellular water (Faghihi et al., 2018).

The responsible for the mass exchange between constituents is described by

$$S_T = \lambda_T^{pa}\phi_T(1-\phi_T)\phi_\sigma = -S_\sigma, \tag{5.89}$$

where

$$\lambda_T^{pa} = \alpha_T^{pa} exp[-\gamma_T^{pa} J_T], \tag{5.90}$$

α_T^{pa} and γ_T^{pa} are constants controlling decay of the growth stretch with increasing tumor volume constant (Faghihi et al., 2018).

Araujo and McElwain (2005) decomposes the classical infinitesimal strain tensor as a sum of two tensors, one due to growth and the other due to stress. The tensor responsible for volumetric growth is given by the anisotropy tensor

$$\Lambda\Omega = \Lambda \begin{bmatrix} \lambda_1 & 0 & 0 \\ 0 & \lambda_2 & 0 \\ 0 & 0 & \lambda_3 \end{bmatrix} \quad , \quad \lambda_1 + \lambda_2 + \lambda_3 = 1 \tag{5.91}$$

where λ_1, λ_2 and λ_3 are anisotropic growth multipliers and Λ is the growth stretch ratio.

Assuming only dilatational growth and resorption, the $\mathbf{F}_T^G$ tensor will be isotropic (Rudraraju et al., 2013), so $\Omega = \mathbf{I}$ and

$$\mathbf{F}_T^G = \Lambda \mathbf{I}. \tag{5.92}$$

Evolution equations for the growth stretch ratio in terms of S_T can be found in the works of Ambrosi and Mollica (2002), Narayanan et al. (2009) and Mpekris et al. (2015).

In Faghihi et al. (2018), the evolution equation used is

$$\Lambda^2 \frac{\partial \Lambda}{\partial t} = \beta S_T \tag{5.93}$$

where β is a constant model parameter that must be calibrated against experimental observations.

5.2 Governing equations for the construction of a mechanical model for tumor growth

Neglecting body forces, the five main equations that make up the model and the related constitutive equations are: mass balance for tumor and nutrients, momentum balance for tumor and nutrients and transport of the deformation gradient.

$$\frac{\partial \rho_T \phi_T}{\partial t} + \nabla \cdot (\rho_T \phi_T \mathbf{v}_T) = S_T + \nabla \cdot [\mathbf{M}_T \cdot \nabla \mu_T] \tag{5.94}$$

$$\frac{\partial \rho_\sigma \phi_\sigma}{\partial t} + \nabla \cdot (\rho_\sigma \phi_\sigma \mathbf{v}_\sigma) = S_\sigma + \nabla \cdot [\mathbf{M}_\sigma \cdot \nabla \mu_\sigma] \tag{5.95}$$

$$\rho_T \phi_T \frac{\partial \mathbf{v}_T}{\partial t} + \rho_T \phi_T \nabla(\mathbf{v}_T)\mathbf{v}_T = \nabla \cdot \mathbf{T}_T - \mathbf{v}_T \left(S_T + \nabla \cdot [\mathbf{M}_T \cdot \nabla \mu_T]\right) \tag{5.96}$$

$$\rho_\sigma \phi_\sigma \frac{\partial \mathbf{v}_\sigma}{\partial t} + \rho_\sigma \phi_\sigma \nabla(\mathbf{v}_\sigma)\mathbf{v}_\sigma = \nabla \cdot \mathbf{T}_\sigma - \mathbf{v}_\sigma \left(S_\sigma + \nabla \cdot [\mathbf{M}_\sigma \cdot \nabla \mu_\sigma]\right) \tag{5.97}$$

$$\frac{\partial \mathbf{F}_T}{\partial t} + \mathbf{v}_T \cdot \nabla \mathbf{F}_T = \nabla \mathbf{v}_T \mathbf{F}_T \tag{5.98}$$

$$\Lambda^2 \frac{\partial \Lambda}{\partial t} = \beta S_T \tag{5.99}$$

where the constitutive equations for μ_T, μ_σ, $\mathbf{T}_T$ and $\mathbf{T}_\sigma$ are

$$\rho_T \mu_T = \frac{\partial \Lambda_T^G}{\partial \phi_T} \left(\hat{\mathbf{T}}_T^{en} \mathbf{F}_T^{-T} : \mathbf{F}_T^S \right) + 2\kappa\phi_T(2\phi_T^2 - 3\phi_T + 1) - \chi\phi_\sigma - \epsilon\Delta\phi_T + \chi\phi_T \tag{5.100}$$

$$\rho_\sigma \mu_\sigma = \frac{1}{\delta_\sigma}\phi_\sigma - \chi\phi_T + \chi\phi_\sigma \tag{5.101}$$

$$\mathbf{T}_T = \frac{1}{J_T^G}\left[\frac{G_T}{(J_T^S)^2}\left[\mathbf{B}_T^S - \frac{1}{2}\,\mathrm{tr}[\mathbf{B}_T^S]\mathbf{I}\right] + K_T(J_T^S - 1)\mathbf{I}\right] - \epsilon\nabla\phi_T \otimes \nabla\phi_T + \Psi_T\mathbf{I} \tag{5.102}$$

$$\mathbf{T}_\sigma = -p_\sigma\mathbf{I} + \Psi_\sigma\mathbf{I} + A_\sigma\mathbf{D}_\sigma - \mu_\alpha\rho_\alpha\phi_\alpha\mathbf{I} \tag{5.103}$$

The coefficients $\mathbf{M}_T$ and $\mathbf{M}_\sigma$ are mobilities, given by $\mathbf{M}_T = M_T\mathbf{I}$ and $\mathbf{M}_\sigma = \frac{1}{\delta_\sigma}M_\sigma\mathbf{I}$, where M_σ is constant, $M_T = \lambda_T^{mob}\phi_T^2(1-\phi_T)^2$ and $\lambda_T^{mob} = \alpha_T^{mob}exp[-\gamma_T^{mob}J_T]$. The terms S_T and S_σ (mass supplied to constituent by other constituents) are given by $S_T = -S_\sigma = \lambda_T^{pa}\phi_T(1-\phi_T)\phi_\sigma$, where $\lambda_T^{pa} = \alpha_T^{pa}exp[-\gamma_T^{pa}J_T]$.

The Equation (5.99) allows to know the growth tensor $\mathbf{F}_T^G = \Lambda\mathbf{I}$. With $\mathbf{F}_T$, $\mathbf{F}_T^G$ and the decomposition (5.57) we have the elastic deformation tensor $\mathbf{F}_T^S$.

We have the option of assembling the system with the first five equations, solving Eq. (5.99) between time steps, or we can choose to add this equation to the system. Thus, the formation of a system composed of the six suggested equations, with adequate initial and boundary conditions, integrates the phase-field and elastic deformation in a mechanical model of tumor growth of four species, containing solid and fluid species.

5.3 Remarks on the mechanical model

The balance of microforces was considered in the formulation of the model, generating a set of fourth order partial differential equations of the Cahn-Hilliard type, to describe the mass balances. The inclusion of a transport equation for the deformation gradient allows to treat it as an unknown factor and thus understand how it acts at each point in the domain. The deformation gradient is responsible for translate the effects of growth/deformation and its decomposition explains the contributions of growth and elastic deformation. The solid constituents are compressible and hyperelastic, because we use the neo-Hookian compressible model a strain energy, and hyperelastic properties for the calculation of the cauchy tensor. The constituents of the fluid are compressible, because of the use of the classic equilibrium pressure, and viscous, by the choice of the dissipation potential.

The set of equations, coefficients and parameters presented in this chapter are based on continuum mechanics, in particular the theory of mixture, theories that are already consolidated in the literature. This is a fundamental condition for the creation of a model, but it does not guarantee that the resulting model will be able to faithfully represent physical or biological phenomena, much less predict these phenomena. For the formulation

of the model and its improvement some other steps are necessary. We must first determine the particular characteristics of the physical or biological event that the model is intended to represent. Second, we need to calibrate the model, that is, determine its parameters by fitting model's predictions with laboratory test results. Finally, we have the validation of the model, which also involves a comparison of predictions of the model with experimental observations, but which are generally conducted in problem domains more complex than those of the calibration process (Oden et al., 2010).

Unfortunately, in this work, we do not include numerical experiments of the mechanical model presented in this chapter, that will be the foccus of our forthcoming efforts. Next chapter presents a set of numerical experiments for the phenomenological model.

6 NUMERICAL RESULTS

We now present some numerical experiments in order to answer some questions about the phenomenological model. First, we check if the implementation of the model can describe the main characteristics of the tumor environment, described in Xu et al. (2016), and the consequences of including the conductivity tensor in the movement of the tip cell. We also checked whether the model has the potential to represent the development of the tumor cord and its peculiarities.

Here we present seven experiments, 3 experiments being a domain in two dimensions and 4 experiments in a domain in three dimensions. In all experiments, the tumor and its necrotic nucleus initially occupy circular (or spherical) concentric regions, the radius of the necrotic part being equivalent to 45% of the tumor radius. Initially, there is a quantity $\sigma = 1.0$ in the capillaries, $\sigma = 0$ in the necrotic nucleus and $\sigma = 0.45$ in the other parts of the domain (Xu et al., 2016). The tumor angiogenic factor has an initial concentration of $f = 0.3$ in the tumor and $f = 0$ in the other points of the domain. The equations are not dimensionalized and we consider a scale of length L = 1.25μm and a time scale T = 1562.5s to find the values of the physical parameters, whose values in silico are given in Tab. 6.1, following Xu et al. (2016).

Table 6.1 – Simulation Parameters - *in silico* values

Symbol	Parameter	*In silico*
M_ϕ	Diffusion coefficient of the tumor	0.3
λ_ϕ	Interface width of tumor	$2\sqrt{2}$
M_c	Mobility of capillaries	1.0
λ_c	Interface width of capillaries	1.0
B_u	Uptake rate of f by capillaries	6.25
D_f	Diffusion coefficient of f	100.0
D_σ	Diffusion coefficient of the nutrient	30.0
V_p^c	Production rate of nutrient	1.0
V_u^T	Uptake rate of nutrient by tumor	0.006
V_u^H	Uptake rate of nutrient by host tissue	0.0006
B_p	Proliferation rate of endothelial cells	1.401
B_u	Uptake rate of TAF by capillaries	6.25
c_{act}	Condition (i) for activation	0.9
f_{act}	Condition (ii) for activation	0.0001
χ	Chemotactic constant	7.28
δ_4	Dll4 effective distance	80

All simulations were performed in parallel on the Lobo Carneiro supercomputer, located at COPPE/UFRJ. The generalized-α method is used for the time integration of

the semi-implicit scheme and the adaptive control of the time step is done by the basic method provided by PETSc library. Inside each time step, Newton's method is used to find the solution of the nonlinear system. For the solution of the resulting linear system we use the GMRES method (Saad and Schultz, 1986) with 30 vectors to restart and classical Gram-Schmidt orthogonalization, in addition to the ILU preconditioner.

6.1 Bidimensional configuration with one rectilinear vessel

In this first experiment, we present simulations in two dimensions to clarify the influence of the conductivity tensor **K** on the formation of the capillary network and on the development of the tumor. A circular tumor with a 625μm radius was placed in the center of a rectangle with the sides 2625μm and 2275μm. To decrease the computational effort, the computational domain is limited to the lower half of this rectangle. A blood vessel, rectilinear and horizontal, was placed 125μm away from the bottom boundary, and has a width constant of 25μm. The mesh consists of 512×128 C^1 quadratic elements. The domain and initial configuration of the vessel and tumor is shown in Fig. 6.1. Figure 6.2 shows a vertical section of the domain, passing through the tumor center ($x = 0$), giving a view of the initial fields distribution.

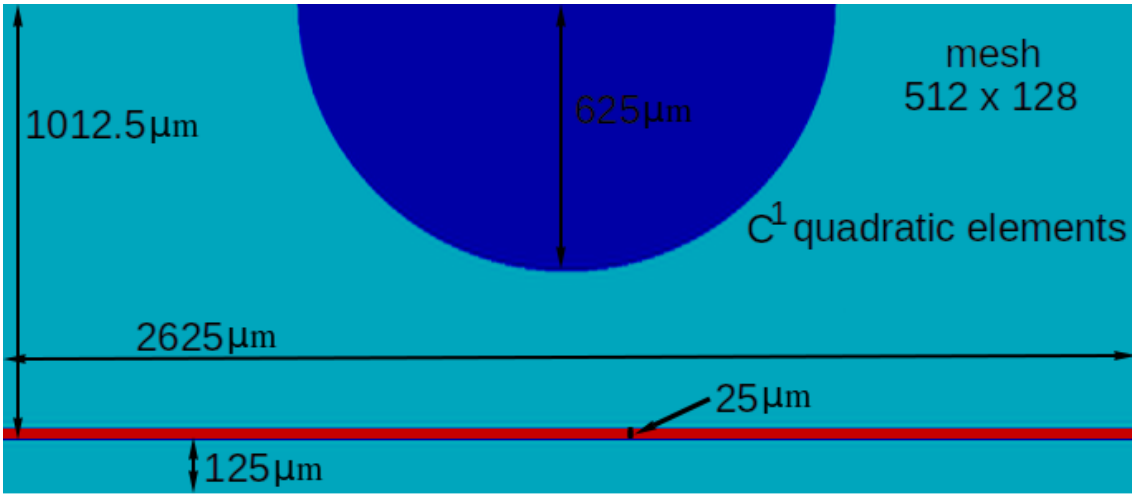

Figure 6.1 – Initial configuration of the vessel (red) at 125μm away from the bottom boundary and tumor (dark blue).

Initially two simulations are carried out, one uses the tip cell displacement according to Xu et al. (2016) and the other includes the conductivity tensor **K** in this process. A third simulation, where the angiogenesis process is blocked, is used as a reference to verify the influence of the new capillary network on tumor development. Blocking angiogenesis is done by inhibiting the discrete part of the code.

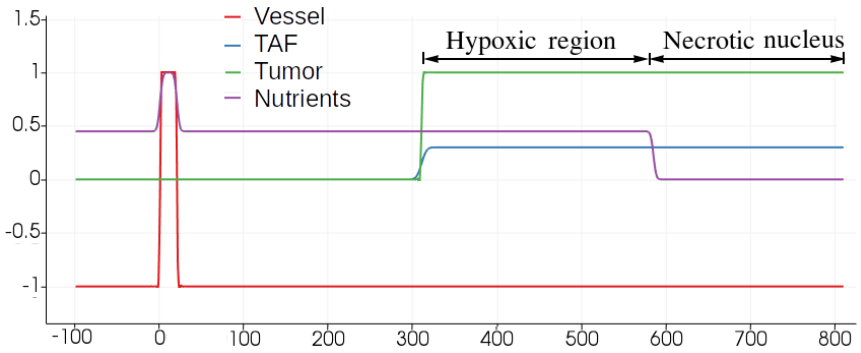

Figure 6.2 – Initial conditions on the fields on a vertical section at $x = 0$: vessel (red), TAF (blue), tumor (green) and nutrients (purple). The x axis refers to the dimensionless vertical length $(-100, 810)$, the equivalent interval in μm is $(-125, 1012.5)$.

Growth and decrease before the awakening of angiogenesis

Before the awakening of angiogenesis, the three simulations produced the same results. The simulation starts, the tumor consumes the nutrients available around it and grows. The tumor grows for 16.24 hours reaching a maximum area of $63.7 \times 10^4 \mu m^2$. At that time, the amount of nutrients is no longer sufficient to maintain growth, and the tumor begins to lose area. This is because μ_ϕ depends on ϕ and σ. Thus, for σ values near to 0.2, μ_ϕ assumes a format similar to that shown in Figure 4.2(b), causing the phase $\phi = 0$ to prevail in the phase-field (4.1). During this period, TAF diffuses through the environment, reaching the pre-existing vessel. At time $t = 30.10$ hours, the first tip cell is activated simultaneously in both simulations. As expected, at that time, the area of the region occupied by the tumor is the same in the three simulations ($61.3 \times 10^4 \mu m^2$). The variation in the area occupied by the tumor region until the moment when the first tip cell is activated is shown in Fig. 6.3.

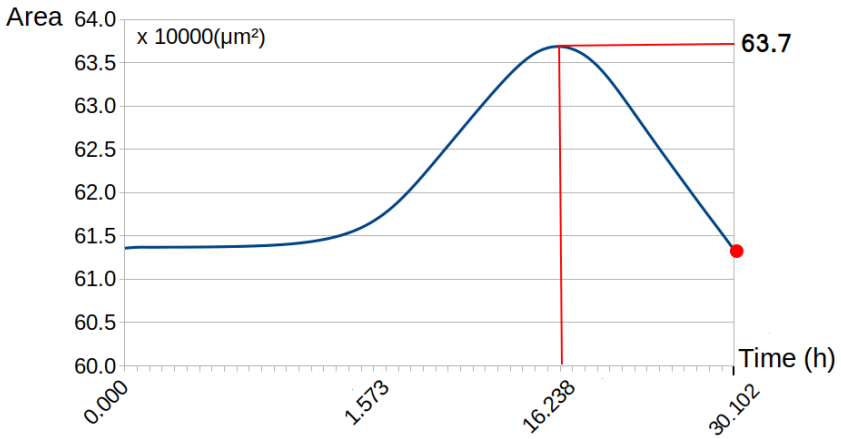

Figure 6.3 – The blue curve describes the variation in the area of the tumor region before the start of the new capillary network. The red line highlight the instant when the tumor area is maximum. The red dot on the curve shows the moment when the first tip cell is activated.

The arrival of the first capillary to the tumor.

The arrival of the first capillary to the tumor occurs at different times in the two simulations, Figs. 6.4(a) and (b) show these moments. The time taken for the first tip cell to reach the tumor was $t = 49.90$ hours for the simulation without conductivity tensor and $t = 56.41$ hours when using the conductivity tensor. This difference in time is due to the greater sinuosity of the capillaries when the conductivity tensor is used (Barbosa et al., 2017).

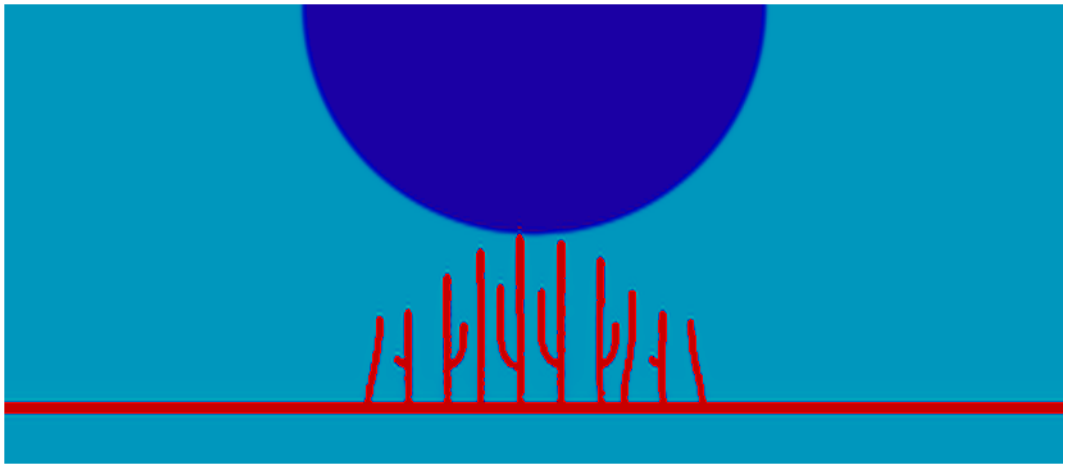

(a) Capillary network on arrival at the tumor, $t = 49.90$ hours. Simulation without conductivity tensor.

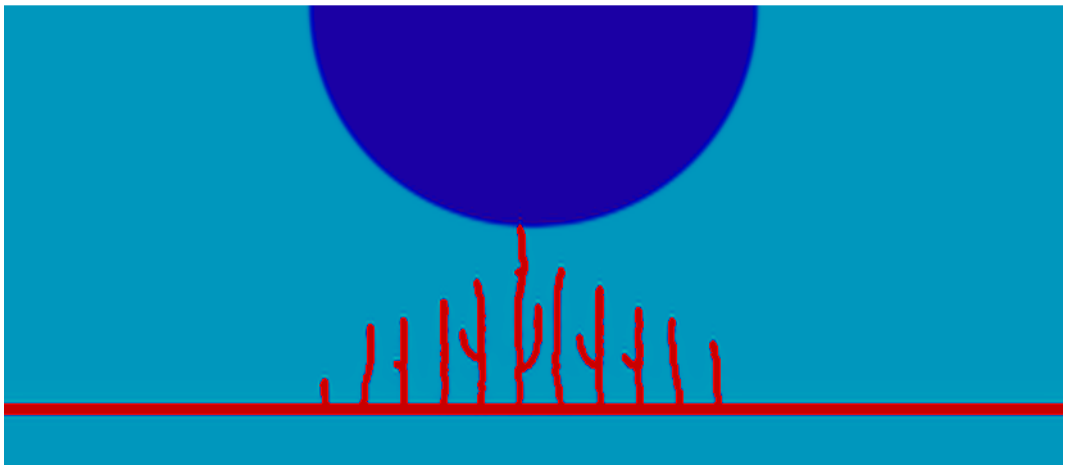

(b) Capillary network on arrival at the tumor, $t = 56.41$ hours. Simulation using the conductivity tensor.

Figure 6.4 – Tumor (dark blue) and blood vessels (red) at the instant of arrival of new tumor capillary network.

We observed a difference of 7.7% between the areas of the tumor regions in Figs. 6.4(a) and (b). This is because of the difference between the times for the new capillary network to reach the tumor ($t = 49.90$ and $t = 56.41$ hours). Figure 6.5 highlights the difference between the areas. The uniform distribution of nutrients in the host tissue contributes to the preservation of the symmetry of the tumor during growth and decrease, before the arrival of the capillary network.

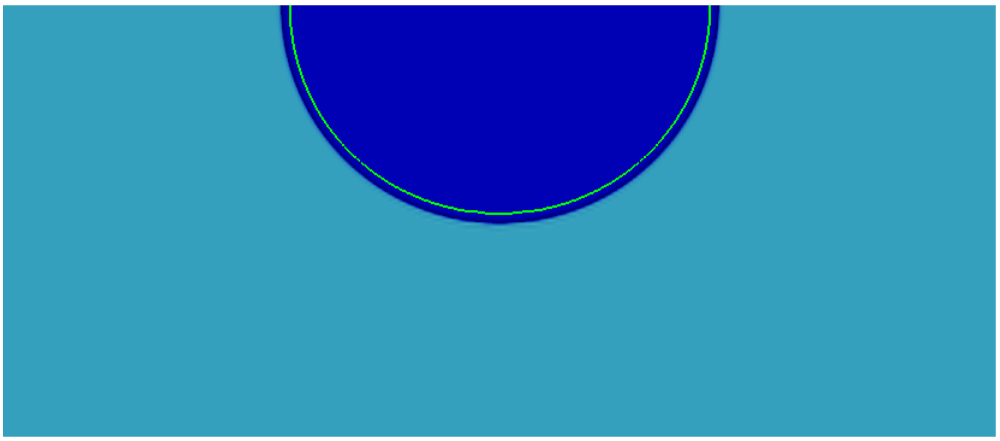

Figure 6.5 – Comparison between areas of the tumor region at the moment the first capillary reaches the tumor. In dark blue the tumor region referring to the simulation without conductivity tensor, in green, the border of the tumor region for the simulation with conductivity tensor.

Based on Xu et al. (2016), the tumor layers are identified by the amount of nutrients in each region. A region of the tumor will be considered necrotic when the amount of nutrients is less than 0.2, for values between 0.2 and 0.4 the region will be hypoxic and for values greater than 0.4 proliferative. When the capillary arrives, the tumor no longer has a proliferative layer, the necrotic nucleus occupies most of it and is surrounded by a thin hypoxic layer. This can be seen in Fig. 6.6, where the white curve describes the limits of the necrotic nucleus and the blue curve determines the outline of the tumor region and also the hypoxic layer.

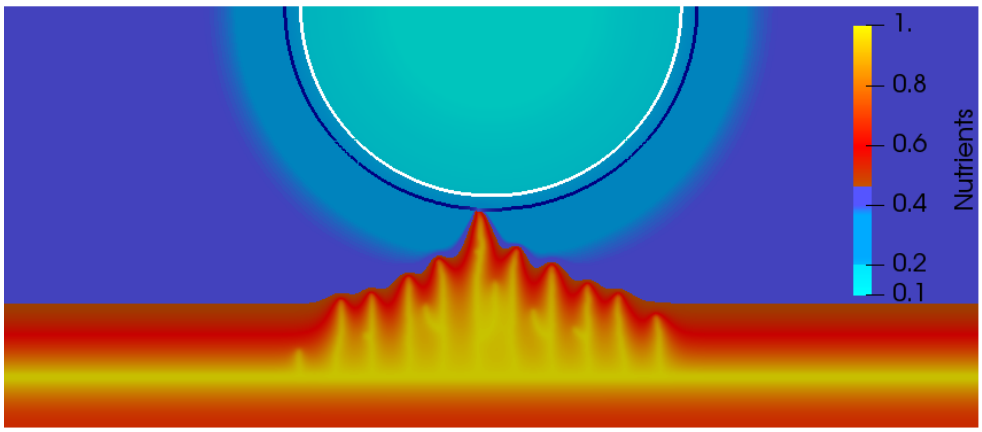

Figure 6.6 – Nutrient distribution at time $t = 56.41$ hours in the simulation using conductivity tensor. The colors determine the amounts of nutrients and the curves demarcate the layers. The white curve determines the border of the necrotic nucleus and the blue curve determines the border of the tumor region and the hypoxic layer.

An amount of TAF sufficient to activate a tip cell already reaches almost the entire vessel by the time the first capillary reaches the tumor. Figure 6.7 highlights, with a white curve, the points in the domain where $f = f_{act} = 0.0001$.

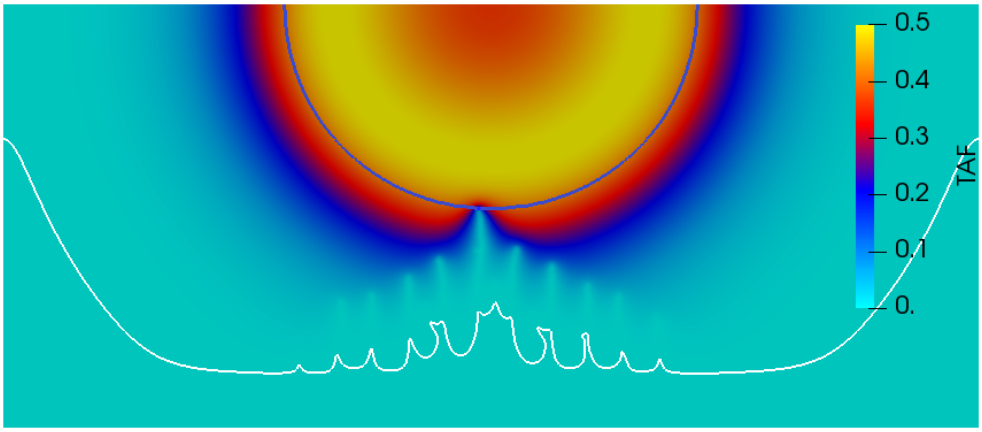

Figure 6.7 – TAF distribution at time $t = 56.41$ hours in the simulation using conductivity tensor. The colors determine the amounts of TAF, the blue curve determines the outline of the tumor and the white curve determines the level $f = f_{act} = 0.0001$ of TAF.

The influence of the new capillary network on tumor growth

In the simulation without conductivity tensor, a denser capillary network and larger tumor area are observed than in the simulation without conductivity tensor. Also, for both simulation, we verified that the part of the tumor furthest from the capillary continues to lose area, while the part in contact with the new capillaries gains area quickly. A graph describing the variation in the area of the tumor region in the three simulations is shown in Fig. 6.8.

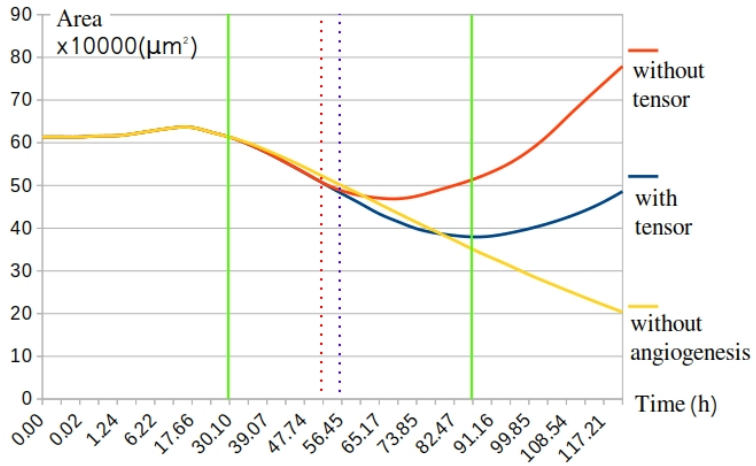

Figure 6.8 – Variations of the tumor areas in the three simulations: angiogenesis without conductivity tensor (red), angiogenesis with conductivity tensor (blue) and without angiogenesis (yellow). Vertical lines in green mark the times $t = 30.10$ hours, moment when the first tip cell is activated, and $t = 86.81$ hours, moment when the tumor reaches its smallest area in the simulation with conductivity tensor. The vertical dotted lines in red and blue demarcate the time when the first tip cell reaches the tumor in simulations without and with the conductivity tensor, respectively.

Figures 6.9(a) and (b) show the tumors and capillary networks after 86.81 hours, at which time the tumor area in the simulation using the conductivity tensor is minimal.

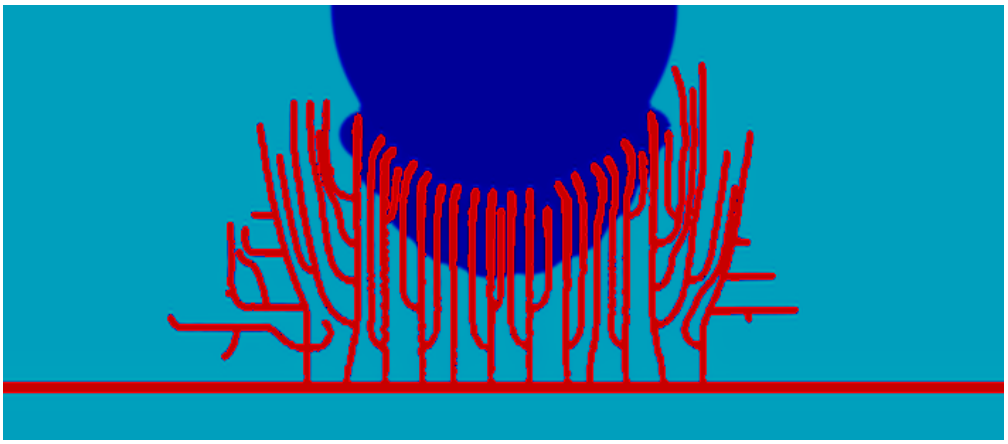

(a) Simulation without conductivity tensor, $t = 86.81$ h.

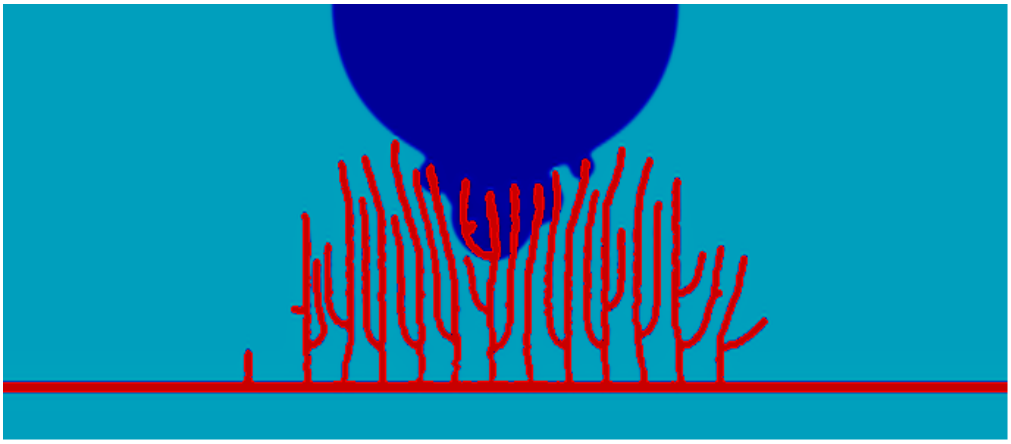

(b) Simulation using the conductivity tensor at the moment when the tumor assumed its smallest area, $t = 86.81$ h.

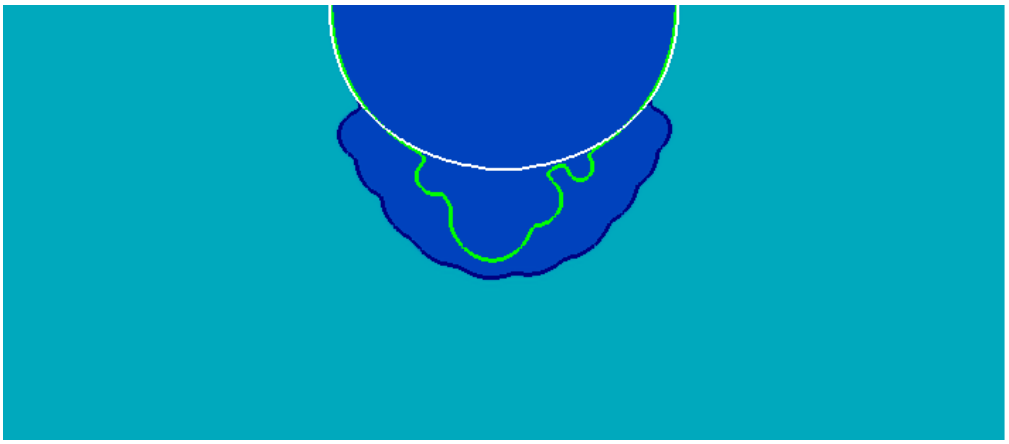

(c) Comparison between the areas of the tumor regions in the three simulations.

Figure 6.9 – Simulation at $t = 86.81$ hours. In (a) and (b) the capillary networks for simulations without and with conductivity tensor, respectively. In (c) comparison between the areas of the tumor regions in the three simulations: without conductivity tensor (blue), with conductivity tensor (green) and without angiogenesis (white).

In Figure 6.9(a), some lateral capillaries grew in a direction parallel to the main vessel, this is due to the fact that the lateral regions of the domain still have a large amount of TAF. The difference between the areas occupied by the tumor in the three simulations is shown in Fig. 6.9(c).

A graph containing the variation of the time step within the time adaptive scheme used is shown in Fig. 6.10. The most marked increase in the size of the time step occurs during the initial growth of the tumor, until time 16.24 hours. Simulations with angiogenesis, with and without conductivity tensor, have similar behavior. From now on, all experiments with angiogenesis will use the **K** conductivity tensor in their formulation.

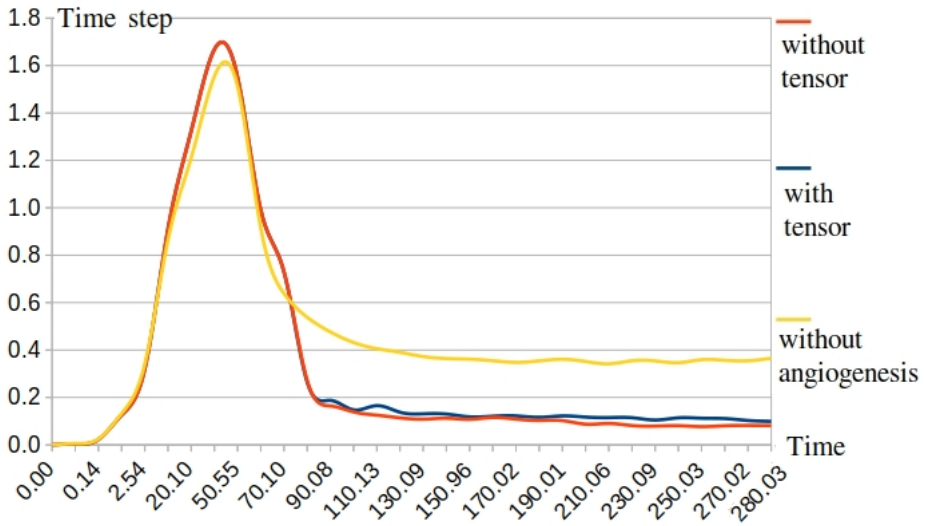

Figure 6.10 – Variation of time step in the three simulations. In red the simulation without conductivity tensor, in blue with conductivity tensor and in yellow the simulation without angiogenesis.

6.2 Bidimensional configuration with curvilinear vessel

In this experiment a circular tumor of 200μm radius placed at a distance of 80μm of a curvilinear vessel in a square domain with 1250μm side discretized by a mesh with 256×256 C^1 quadratic elements is considered. The curvilinear vessel has a cubic function configuration, with a maximum width of 25μm, as shown in Fig. 6.11(a). In this experiment, we did not record a decrease in the tumor area, only growth. The proximity between tumor and vessel facilitated the rapid arrival of the capillary network and the initial tumor area ($12.57 \times 10^4 \mu m^2$) increased by 260% at the end of 92.2 hours, reaching $33.42 \times 10^4 \mu m^2$. The first tip cell is activated after 1.52 hours of simulation arriving at the tumor after 10.65 hours.

After 13.7 hours of simulation, 8 capillaries were born from the main vessel, all separated by a distance of $\delta_4 = 100\mu$m, see Fig. 6.11(b). New tip cells may awaken between

these capillaries, as long as they meet the activation conditions. In Fig. 6.11(c) we see that the first tip cells have already moved more than 100μm away from the main vessel, allowing the birth of new tip cells between the capillaries.

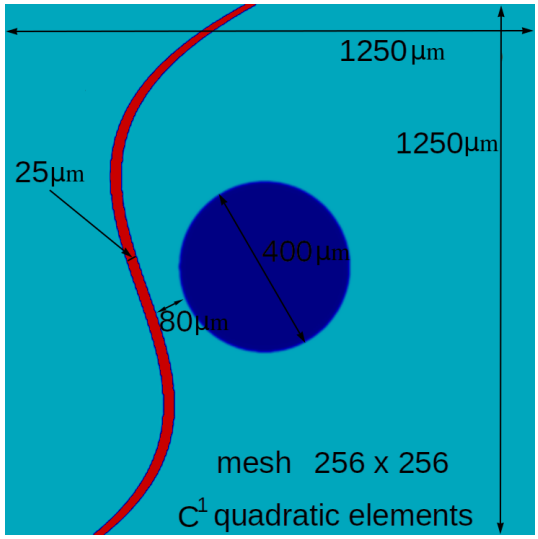

(a) Initial configuration of the vessel and tumor.

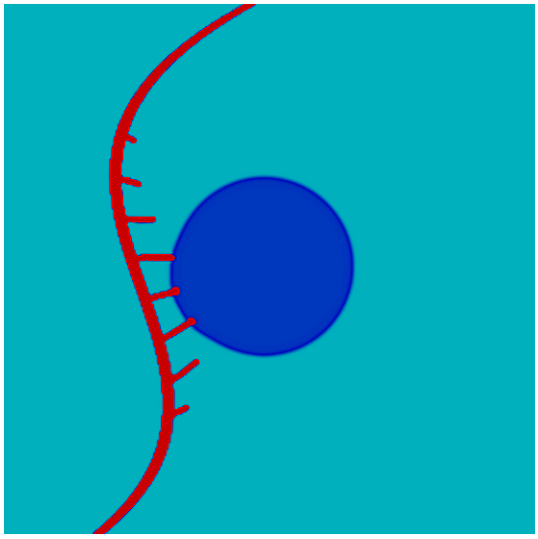

(b) At that moment, three capillaries feed the tumor (t = 13.7h).

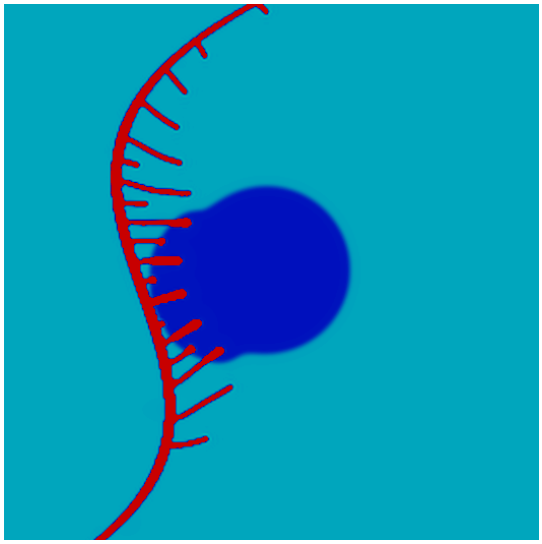

(c) New capillaries are born in the original vessel (t = 28.5h).

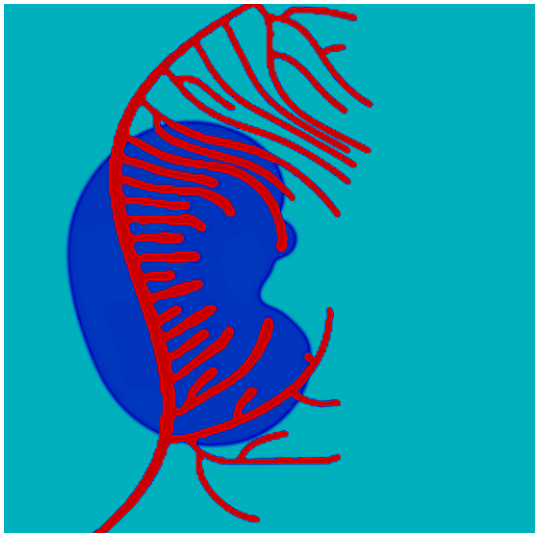

(d) The capillary network involves the tumor (92.2h) .

Figure 6.11 – The formation of the new capillary network.

It is important to point out that, in all experiments, after the new capillaries reached the tumor, they did not branch. On the other hand, capillaries that are born furthest from the tumor are more likely to branch out, as it can be seen in Fig. 6.11(d), where we have the final configuration of the experiment after 92.2 hours, with the capillaries surrounding almost the entire tumor.

The distribution of nutrients and TAF by the domain, after 92.2 hours, are shown in Fig. 6.12(a) and 6.12(b). In this instant, the tumor no longer has a necrotic nucleus and

the hypoxic layer has been reduced to a small region, while the proliferative layer occupies most of the tumor.

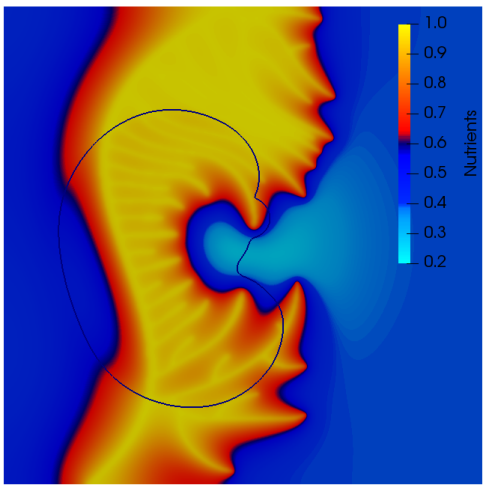

(a) Nutrients distributed in the domain in the instant 92.2h. The blue curve highlights the tumor boundaries.

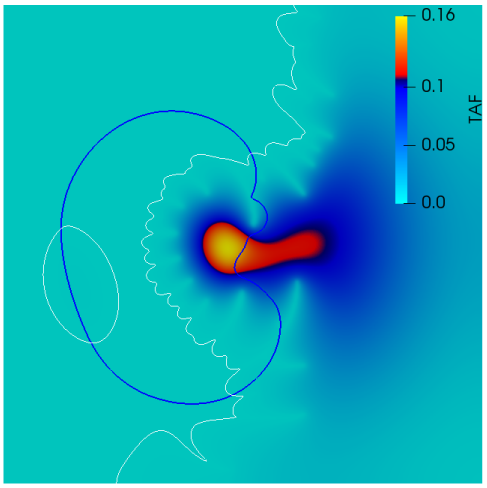

(b) TAF distributed in the domain at the instant 92.2h. The blue curve highlights the tumor boundaries and the white curve determines the level $f = f_{act} = 0.0001$.

Figure 6.12 – Configuration of nutrients and TAF after 92.2 hours.

Another experiment in two dimensions, with two pre-existing vessels, is presented in the B.1.

6.3 Tridimensional configuration with one rectilinear vessel

In this section we present an experiment in three dimensions, simulating the behavior of a spherical tumor placed in the vicinity of a straight circular cylinder blood vessel. We placed in a domain $625 \times 625 \times 750 \mu\text{m}^3$ a spherical tumor with a radius of 175μm and the vessel with a radius of 25μm. The initial distance between the vessel and tumor is 112.5μm. Figure 6.13(a) shows the initial tumor and vessel configuration.

Once, the experiments in three dimensions demand great computational resources, there is limitation of working with a fine mesh. Because of that, we consider a coarse mesh of $50 \times 50 \times 60$ C^1 quadratic elements. The radius of the tip cell is 12.5μm and the number of new capillaries is limited to just 6 to reduce computational burden. The discrete part of the model was activated every 2 time steps and the conductivity tensor used every 4 time steps. The maximum processing time was limited to 360 hours, using an exclusive node with 48 CPUs operating in parallel with 8 mpiprocs on the LoboC-UFRJ supercomputer.

Figure 6.13(c) and (d) show the 6 capillaries born after 27.4 hours of simulation, where 4 of them penetrated the tumor. The initial development of the tumor, driven by the consumption of available nutrients, increases its volume from $2.25 \times 10^7 \mu\text{m}^3$ to

$2.93 \times 10^7 \mu m^3$ in 15.3 hours. After initial growth, the tumor volume decreases until the end of the simulation, reaching $2.50 \times 10^7 \mu m^3$.

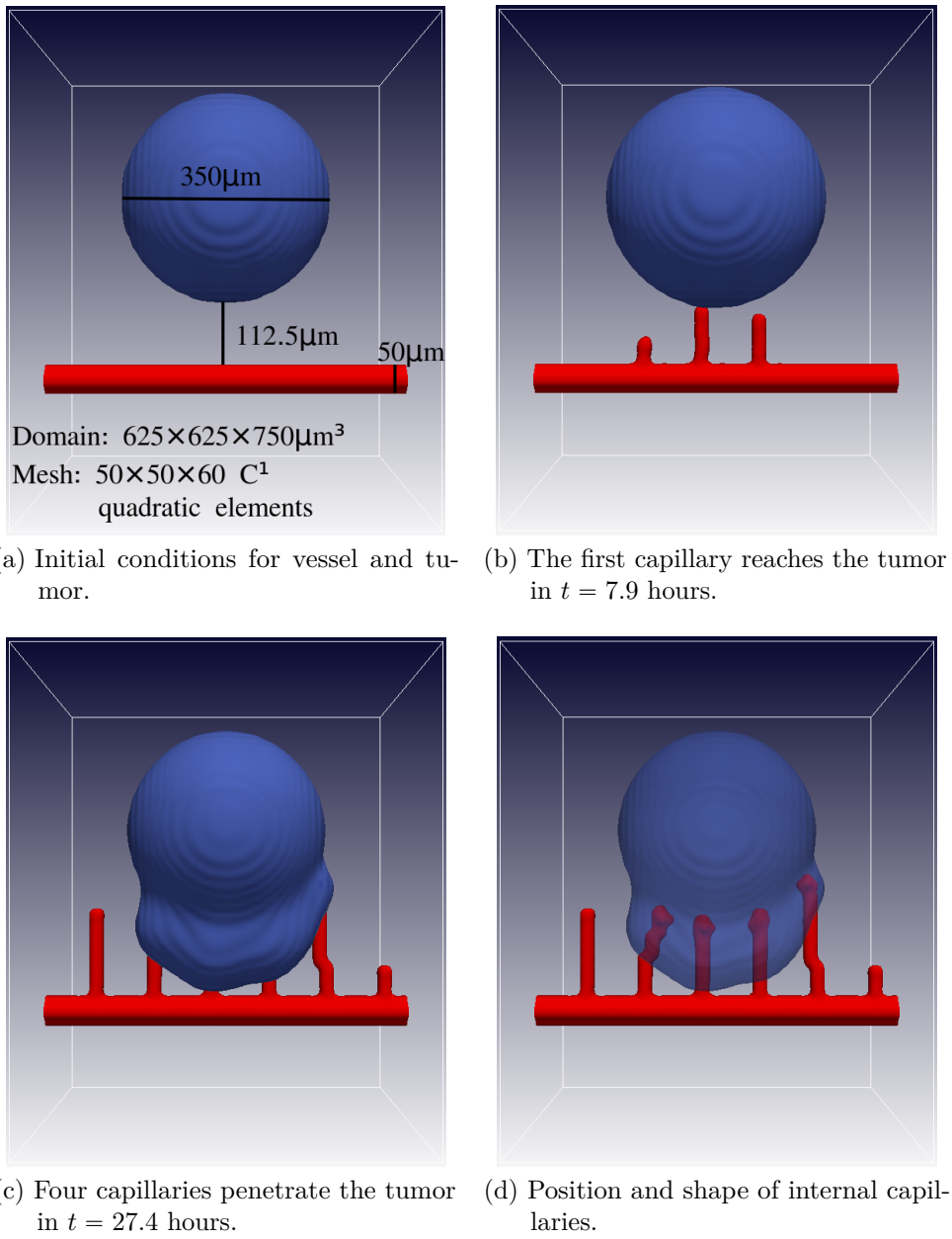

(a) Initial conditions for vessel and tumor.

(b) The first capillary reaches the tumor in $t = 7.9$ hours.

(c) Four capillaries penetrate the tumor in $t = 27.4$ hours.

(d) Position and shape of internal capillaries.

Figure 6.13 – Formation of the capillary network considering a spherical tumor and a straight cylindrical vessel. Tumor in blue and vessel in red.

Figure 6.14 show a section of the domain by a vertical plane at $y = 0$, determining the levels of nutrients and TAF concentrations on the plane. The amount of nutrients over the entire plane is greater than 0.2, indicating that there is no more necrotic nucleus after 27.4 hours of simulation, as can be seen in Fig. 6.14(a). The region in shades of blue indicates an amount of nutrients that determines the hypoxic layer on the tumor and the yellow and red region determines the proliferative layer. In Fig. 6.14(b) we can see that, the levels of TAF, spread over the plane, exceeds the minimum activation value of a tip

cell, which in this experiment is $f_{act} = 0.001$.

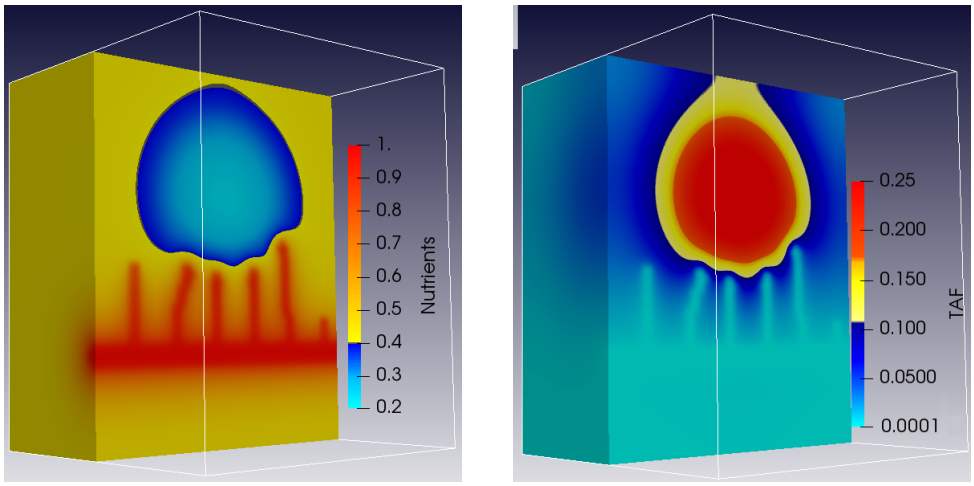

(a) Distribution of concentrations of nutrients.

(b) Distribution of concentrations of TAF.

Figure 6.14 – Vertical plane at $y = 0$ highlighting the concentration of nutrients and TAF.

Hypoxic and proliferative regions of the tumor are easily identified by projecting the levels of nutrients on their surface, as can be seen in Fig. 6.15(a). In blue the hypoxic region and in yellow and red the proliferative region. We also observed in Fig. 6.15(b) that the lower part of the tumor, which is in contact with capillaries, has a higher concentration of nutrients.

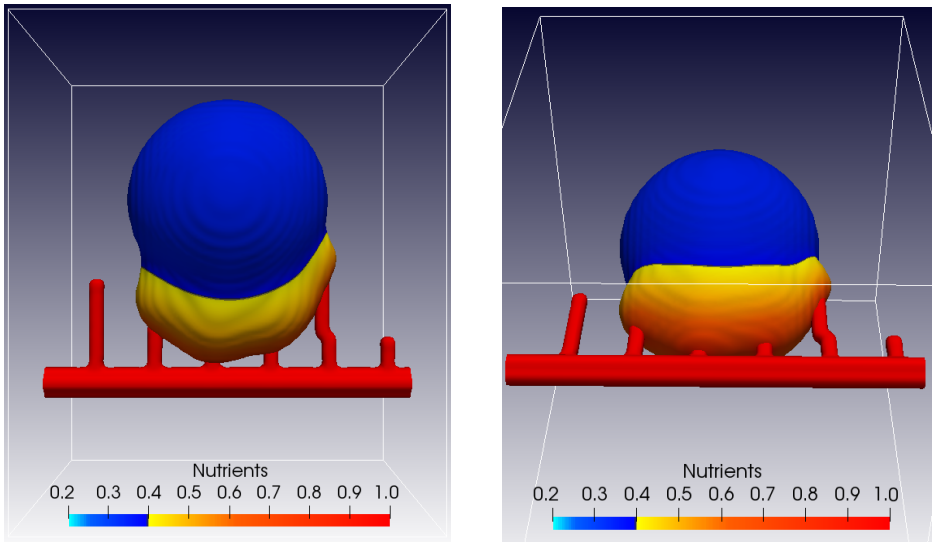

(a) Concentration thresholds from 0.2 to 0.4 determine the hypoxic region of the tumor and levels greater than 0.4 indicate a proliferative region.

(b) View of the lower part of the tumor, revealing that the region close to the capillaries has high levels of nutrients.

Figure 6.15 – Concentration of nutrients distributed over the surfaces of the tumor, vessel and capillaries.

Figure 6.16(a) and (b) show the concentration of TAF on the surfaces of the tumor, vessel and capillaries. We observed that the regions of the tumor that are close to the capillaries have low levels of TAF, while far distant regions have high levels.

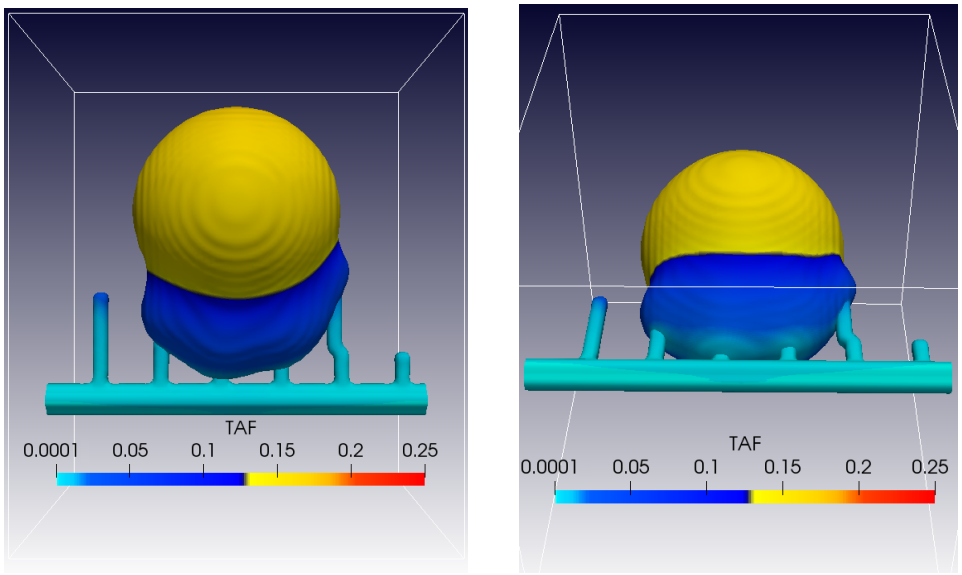

(a) After $t = 27.4$ hours, TAF concentration are greater than $f_{act} = 0.001$ over all capillaries and vessel.

(b) Lower view of the tumor, revealing that near the capillaries the TAF concentration are lower.

Figure 6.16 – Concentration of TAF distributed over the surfaces of the tumor, vessel and capillaries.

In this example, as in that presented in Section 6.2, the necrotic nucleus disappeared at the end of the simulation. This is due to the diffusion of nutrients, the proximity between the tumor and the vessel and, also, the rapid arrival of the capillary network, distributing nutrients throughout the tumor region. The distinction between tumor layers, made according to the distribution of nutrients, does not ensure the maintenance of the necrotic nucleus. This is a characteristic of the model that can be modified, ensuring better demarcation and preservation of the necrotic nucleus. In the model presented by Lima et al. (2014), the necrotic, hypoxic and proliferative regions are described individually as different phases, ensuring a better demarcation of those regions.

6.4 Tridimensional configuration with curvilinear tubular vessel

In this experiment, we consider a spherical tumor near a curvilinear tubular vessel. A spherical tumor, with a 175μm radius, and a curvilinear tubular vessel, with a 25μm radius, are placed in a $625 \times 625 \times 750 \mu m^3$ three-dimensional domain. The initial distance between tumor and vessel is 115.8μm and we consider the radius of the tip cells measures 12.5μm. In Fig. 6.17(a) we have the initial vessel and tumor configuration. As in the previous example (Section 6.3), we used a coarse mesh of $50 \times 50 \times 60$ C^1 quadratic

elements and the processing time was also limited to 360 hours with the same equipment configurations.

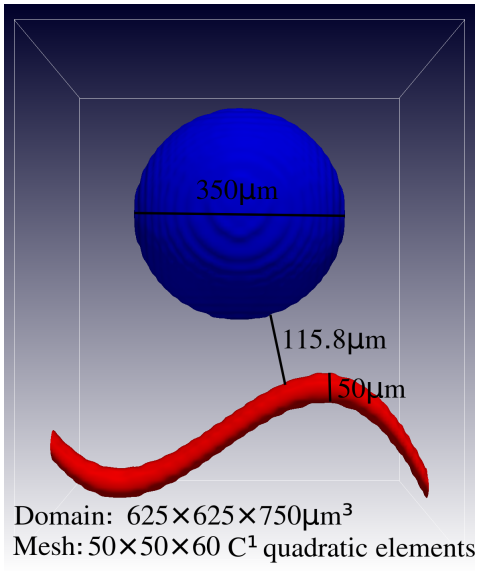

(a) Initial conditions for vessel and tumor.

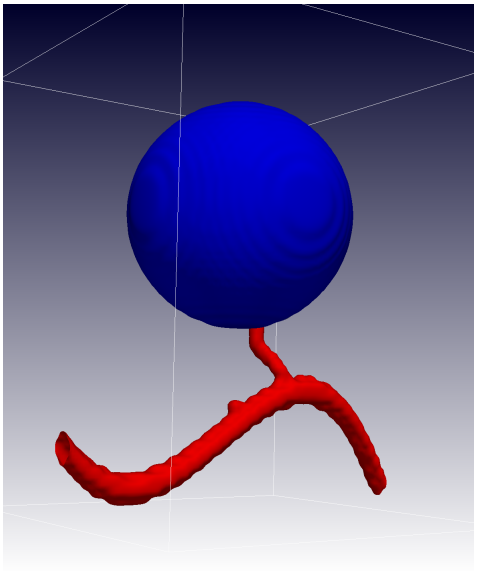

(b) The first capillary reaches the tumor in $t = 11.05$ hours.

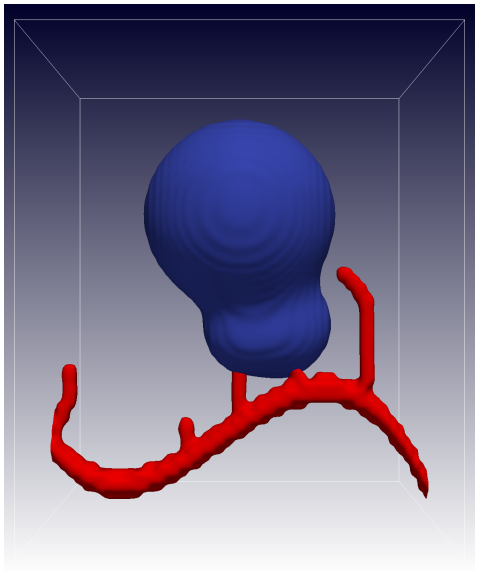

(c) Two capillaries penetrate the tumor at $t = 30.72$ hours.

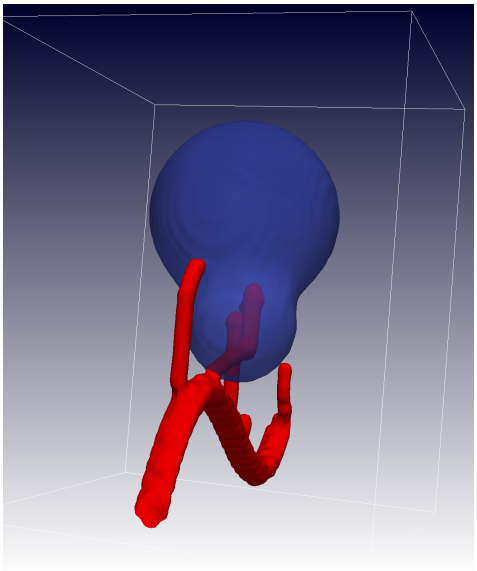

(d) Position and shape of internal capillaries.

Figure 6.17 – Formation of the capillary network considering a spherical tumor and a curvilinear tubular vessel. Tumor in blue and vessel in red.

Initially the tumor grows, consuming the available nutrients and increasing its volume from $2.25 \times 10^7 \mu m^3$ to $2.92 \times 10^7 \mu m^3$ in 14.34 hours. After the initial growth, the tumor volume decreases until the end of the simulation. The first capillary reaches the tumor in $t = 11.05$ hours (see Fig. 6.17(b)), at which time the tumor was still increasing in volume. The increase in the volume of the region in contact with the capillaries and the decrease in the volume in the opposite region reduce the total tumor volume to $2.03 \times 10^7 \mu m^3$ after

30.72 hours, see Fig. 6.17(c) and (d). During the processing time, only 5 capillaries were born and two of them penetrated the tumor.

For a better understanding of nutrients distribution, we consider a vertical plane at $y = 0$, as shown in Fig. 6.18(a). The highest levels of nutrients occur over the vessel and capillaries (red), and the lowest are in the center of the tumor (light blue). In the yellow region, nutrient levels are above 0.4, indicating that tumor cells in those regions are considered proliferative. Figure 6.18(b) shows a projection of nutrient levels on the tumor surface, demarcating the hypoxic and proliferative regions. Tumor regions that are closer to the capillaries have higher levels of nutrients.

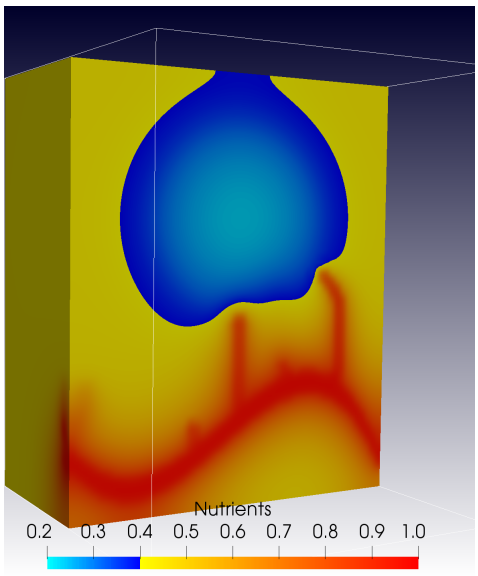

(a) Concentration of nutrients on the vertical plane that cuts tumor and vessel. Nutrient levels greater than 0.2 indicate the absence of a necrotic core

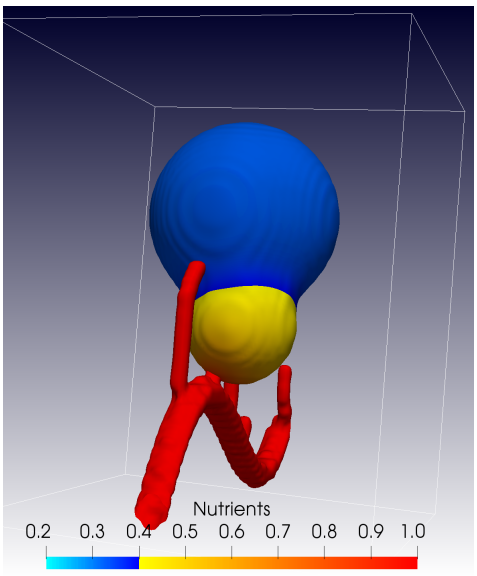

(b) Concentration of nutrients distributed over the surfaces of the tumor, vessel and capillaries. In blue the hypoxic region and in yellow the proliferative region.

Figure 6.18 – Concentration of nutrients on the vertical plane $y = 0$ and on the surface of the tumor, vessel and capillaries after 30.72 hours.

The disappearance of the necrotic core also occurred in this experiment. Initially, the tumor has only necrotic core and proliferative layer, as can be seen in Fig. 6.19(a). The diffusion of nutrients promotes the decrease of the necrotic nucleus, while the diffusion associated with the consumption of nutrients generates the hypoxic layer. After $t = 11.53$ hours the hypoxic region occupies most of the tumor, a thin proliferative layer covers the entire tumor and the necrotic nucleus has been reduced to a small central region, disappearing in the next time, see Fig. 6.19(b). At $t = 30.72$ hours (FIg. 6.19(c)), the proliferative region is concentrated around the capillaries and the rest of the tumor is formed by hypoxic cells.

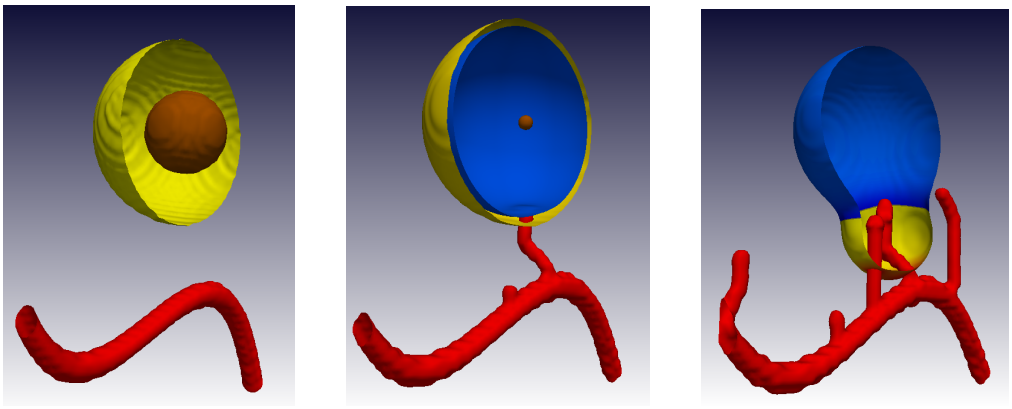

(a) $t = 0$ hours. (b) $t = 11.53$ hours. (c) $t = 30.72$ hours.

Figure 6.19 – Configuration of hypoxic, proliferative and necrotic regions at different times of the simulation. In yellow the surface that limits the proliferative layer, in blue the surface that limits the hypoxic layer, in brown the necrotic nucleus and in red the vessel and capillaries. (a) Start of simulation, the tumor has only the proliferative layer and necrotic nucleus. (b) After $t = 11.53$ hours, the hypoxic layer already occupies most of the tumor, reducing the proliferative layer and necrotic nucleus. (c) At the end of the simulation, the tumor is composed of hypoxic and proliferative regions.

The TAF concentration on the vertical plane $y = 0$, which cuts off the tumor and vessel, are shown in Fig. 6.20(a). Concentration greater than $f_{act} = 0.001$ over the vessel and capillaries indicate that the amount of TAF is sufficient to awaken new tip cells. Figure 6.20(b) shows the projection of TAF levels on the tumor, vessel and capillaries.

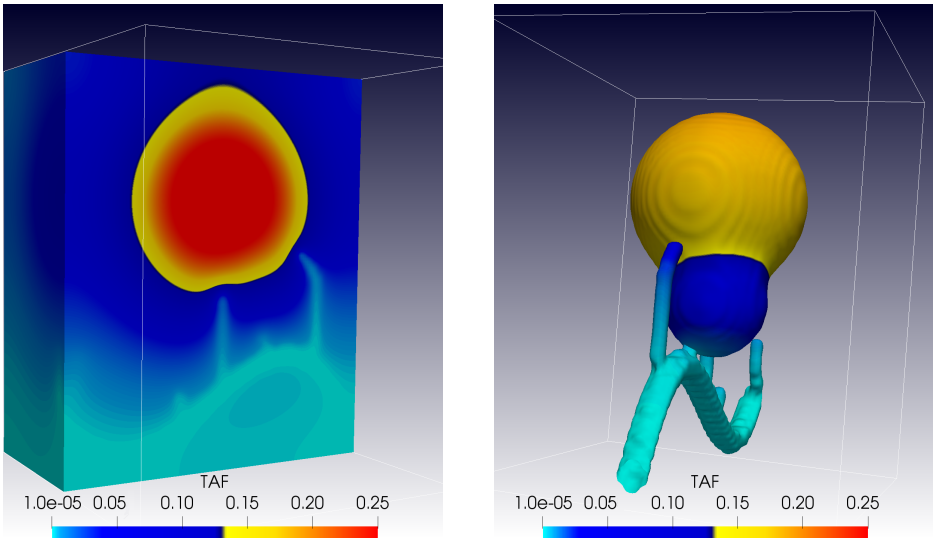

(a) Distribution of TAF concentration on the vertical plane that cuts tumor and vessel.

(b) TAF concentration are greater than $f_{act} = 0.001$ over all capillaries and vessel.

Figure 6.20 – TAF concentration on the vertical plane $y = 0$ and on the surface of the tumor, vessel and capillaries after 30.72 hours.

The initial time step is $\Delta t = 10^{-11}$ and, with the adaptive process, it increases rapidly until reaching the value of $\Delta t = 0.72$, interrupting the growth when the first tip cell is activated, see Fig. 6.21. After that instant, we have oscillations, with values ranging from $\Delta t = 0.23$ to $\Delta t = 7.0$, reaching the end of the simulation with the value $\Delta t = 0.26$.

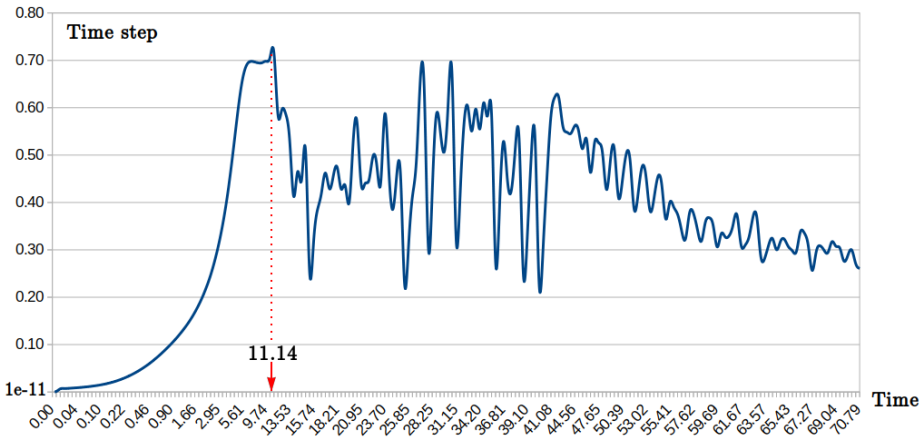

Figure 6.21 – Graph with time step variation for a spherical tumor and a curvilinear tubular vessel. Time $t = 11.14$ is equivalent to physical time $t = 4.84$ hours and final time $t = 70.79$ is equivalent to time 30.72 hours, when the scale $T = 1562.5s$ is considered.

6.5 Tumor cords

In this section we present three numerical experiments describing the behavior of tumor cords. In these experiments, we analyze the model's ability to represent the development of a tumor cord, its adaptation to the vessel shape and its new concentration of nutrients. For the development of the tumor without the aid of angiogenesis, we need the tumor to be less than 180μm from the vessel. According to Harris (2002), this is the distance that oxygen diffuses as it passes from the vessel to the cells, before being completely metabolized.

The tumor cord was studied in Bertuzzi et al. (2002), Bellomo et al. (2008), Moore et al. (1985), Bertuzzi and Gandolfi (2000), Bertuzzi et al. (2004), Astanin and Preziosi (2009), S. and Tosin (2007). Bellomo et al. (2008) states that the proliferative zone will be (internal) next to the nutrient supply and the necrotic zone will be the outermost layer. Some details of other studies on the tumor cord are presented in Section 2.1.3.

The first experiment is carried out in a two-dimensional domain and the last two in three-dimensional domains. Here we also use the LoboC supercomputer, located at UFRJ. In each simulation, we use an exclusive node and 48 cpus, operating in parallel with 12 mpiprocs. In these experiments, the discrete part of the model was not activated. The configurations of solvers, preconditioners and time-step adaptivity used are the same as those for experiments with angiogenesis.

6.5.1 Tumor cord - Two-dimensional configuration with curvilinear vessel

The same configuration of the experiment presented in Section 6.2 is considered in this experiment, but without the activation of angiogenesis. The main idea of this experiment is to verify the model ability to represent some characteristics of the tumor cord in a two-dimensional environment. We simulated a curved vessel to check the influence of capillary shape on the tumor growth. The initial configuration of the vessel and tumor can be seen in Fig. 6.11(a). Initially, a symmetrical growth is observed, then the tumor cells proliferated towards the vessel, assuming their shape, as shown in Figs. 6.22(a)-6.22(f).

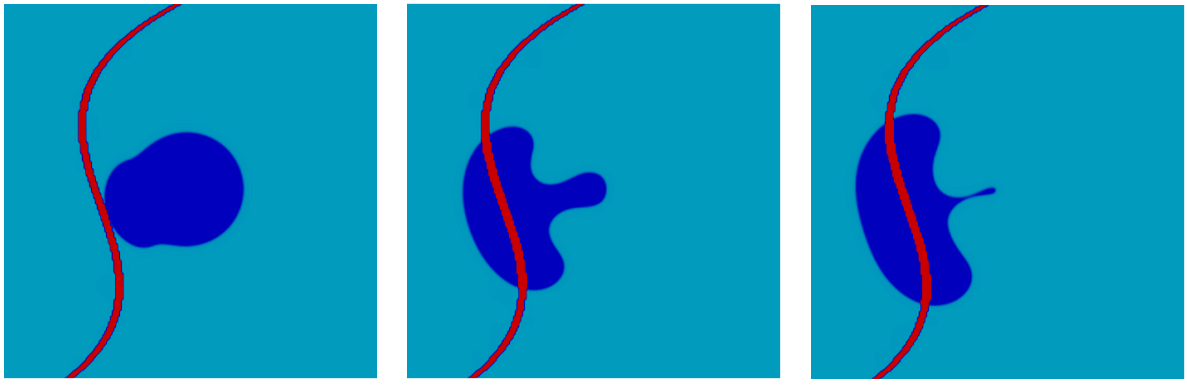

(a) The tumor grows towards the vessel at time $t = 31.64$ hours.

(b) Most of the tumor already involves the vessel at time $t = 82.70$ hours.

(c) A small region separates from the larger part of the tumor at time $t = 98.16$ hours.

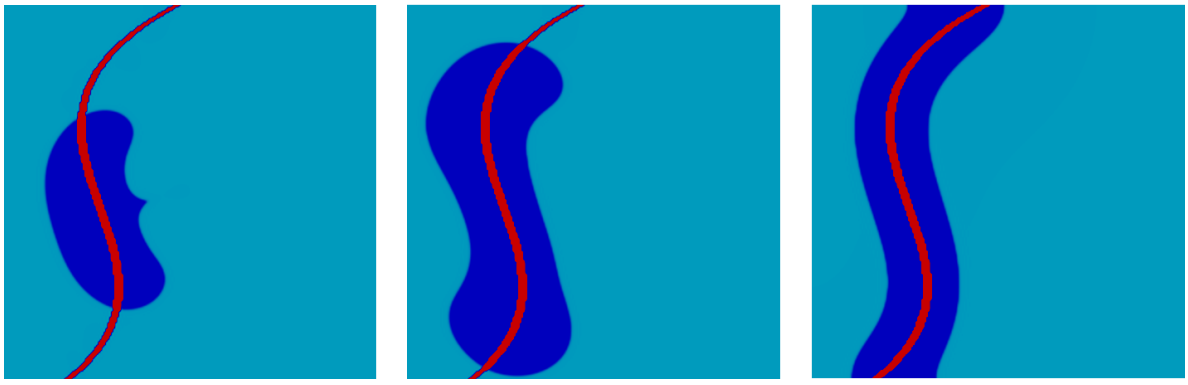

(d) The smaller region disappears completely at time $t = 107.90$ hours.

(e) The tumor develops quickly following the shape of the vessel at time $t = 176.26$ hours.

(f) The tumor completely surrounds the vessel at time $t = 4340.3$ hours.

Figure 6.22 – Behavior of the model for a tumor that does not trigger angiogenesis that is born in the vicinity of a vessel. After $t = 4340.3$ hours of simulation, the tumor forms a constant layer, 100μm thick, covering the entire vessel.

The increase in volume in one region of the tumor and the decrease in volume in the opposite region are confused with a possible movement of the tumor. In Fig. 6.22(c), we see that the tumor divides into two parts, a larger part, which advances over the vessel, and a smaller part, which disappears in the next steps of time. This behavior can be better understood by looking at Fig. 6.23(a), where we see that the smallest part is over a region

with a low level of nutrients, being formed by necrotic cells. Whereas, in Fig. 6.23(b) we see that at time 4340.3 hours the tumor has no necrotic layer, it has a thin layer of hypoxic cells (in black) and the rest formed by proliferative cells. Thus, in the final configuration of the simulation we observed a great amount of nutrients in the inner part of the tumor and a low concentration of nutrients in the part of the tumor is farthest from the capillary, leading to the hypoxia of the cells.

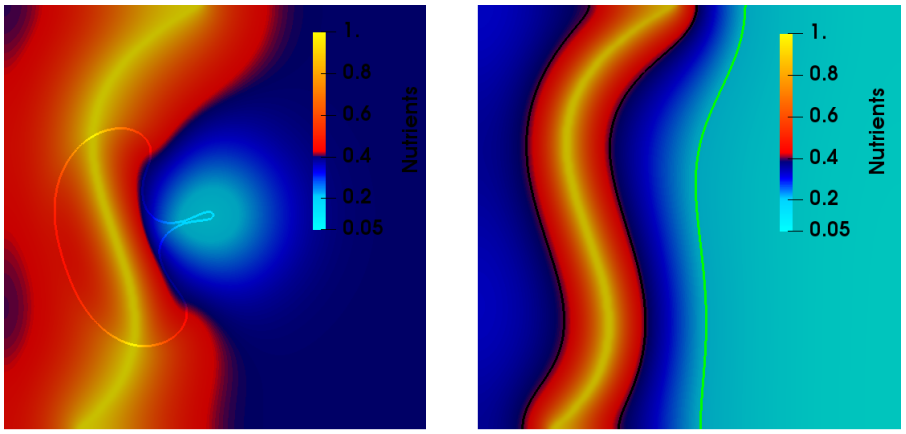

(a) Concentration of nutrients at time $t = 98.16$ hours. The curve highlights the outline of the tumor.

(b) Concentration of nutrients at time $t = 4340.3$ hours. The green curve highlights the 0.2.

Figure 6.23 – Concentration of nutrients at $t = 98.16$ and $t = 4340.3$ hours.

The tumor layer surrounding the vessel has a thickness of approximately 110μm, resulting in a tumor cord of approximately 245μm in diameter. A perpendicular section to the vessel is shown in Fig. 6.24, showing the configuration of the fields at time $t = 4340.3$h.

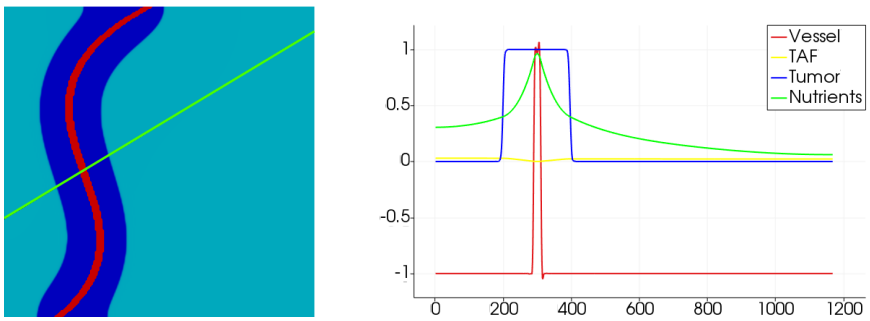

(a) In green a perpendicular section to the vessel.

(b) Section configuration of the fields at time $t = 4340.3$ hours.

Figure 6.24 – Cut perpendicular to the vessel, indicating distances at time $t = 4340.3$ hours. Applying the length scale $L = 1.25\mu$m, a distance of 100 in the graph (b) is equivalent to 125μm.

When performing the section perpendicular to the vessel, we observed a small numerical instability in the phase-field that describes the vessel, see Fig. 6.24(b). We note that, depending on the position of the cut, this instability is changes, even disappearing in

some positions. This instability is located over the phase transition and can hardly be seen in Figure 6.24(a).

A graph describing the variation in the area of the tumor region is shown in Fig. 6.25. Initially, the tumor develops by consuming the nutrients available in the host tissue for 20.13 hours. Between 20.13 and 56.46 hours, the tumor reduces its total area, gaining area in the region close to the nutrient source and losing it in the most distant region. After 56.46 hours the tumor starts to increase its total area. The largest visible area of the tumor occurs at $t = 219.79$ hours, reaching an area of $40.53 \times 10^4 \mu m^2$. The evolution of the system towards a steady state can be seen at the end of the graph, where the area assumes the constant value $33.3 \times 10^4 \mu m^2$ after 4340.3 hours until the end of the simulation, at 28948.26 hours.

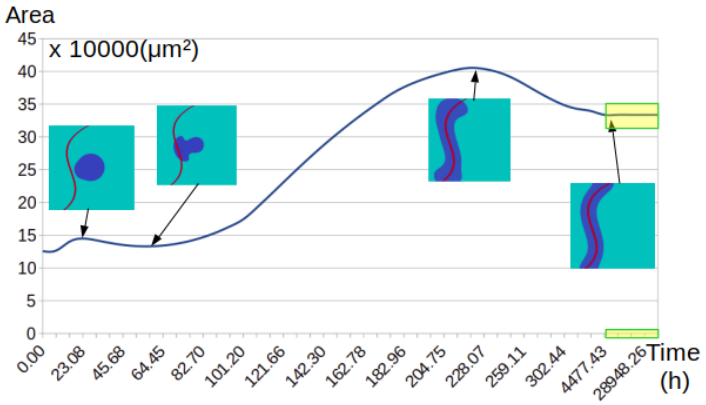

Figure 6.25 – Area Variation of the tumor region. Initial area $12.6 \times 10^4 \mu m^2$, final area (visible) $33.4 \times 10^4 \mu m^2$ after 4340.3h (180.8 days) until the end of the simulation, at 28948.26 hours (1206.2 days).

6.5.2 Tumor cord - Three-dimensional configuration with one rectilinear vessel

A spherical tumor with $200\mu m$ radius is placed in the vicinity of a straight vessel. In this experiment the distance between the pre-existing vessel and the tumor is of $112\mu m$ (see Fig. (6.26(a))), thus allowing the arrival of nutrients from the vessel to feed the tumor. The dimensions of the domain are $1000 \times 750 \times 1000 \mu m^3$.

Initially the tumor consumes the surrounding nutrients and has a small uniform increase in volume. The concentration of nutrients on the vessel diffuses into the tissue and reaches the tumor, so the tumor region closest to the vessel develops and gains volume, see Fig. 6.26(b). The tumor region more distant the vessel does not receive enough nutrients for growth, decreasing in volume, see Fig. 6.26(b). Figure 6.26(d) shows the tumor divided into two parts. The largest part of the tumor continues to gain volume, while the smallest loses volume until it disappears completely, as shown in Fig. 6.26(e). Finally, the tumor completely envelops the vessel, forming a cylindrical layer around the vessel, Fig. 6.26(f).

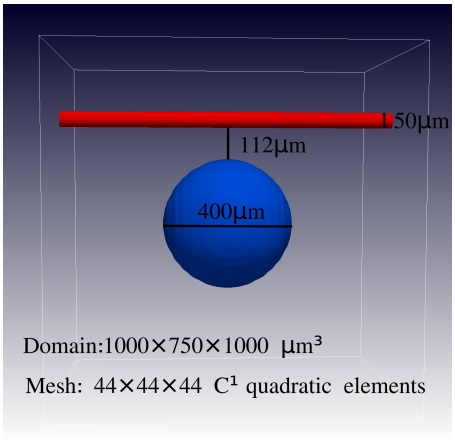

(a) Initial conditions for vessel and tumor.

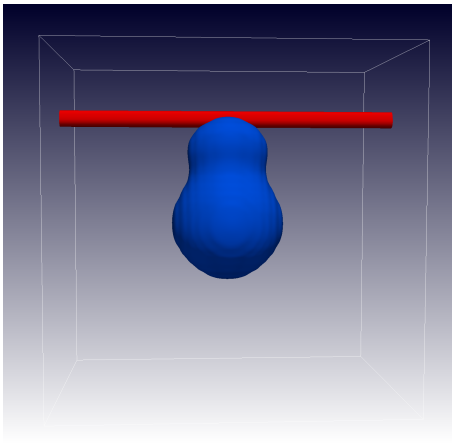

(b) Tumor growth towards the vessel, $t =$ 30.39 hours.

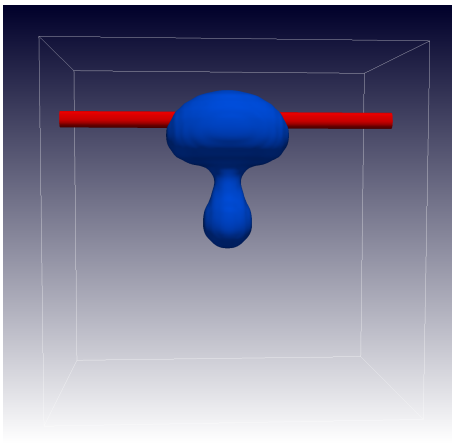

(c) Part of the tumor involves the vessel, $t = 41.39$ hours.

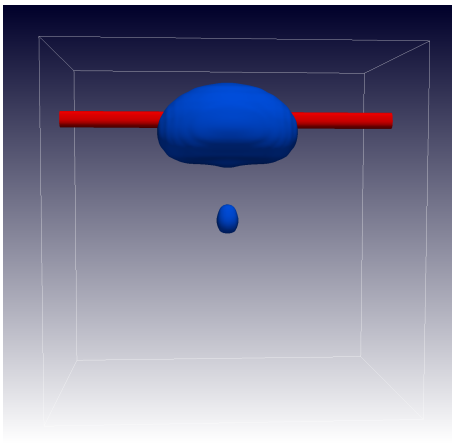

(d) The tumor separates into two parts, $t = 45.15$ hours.

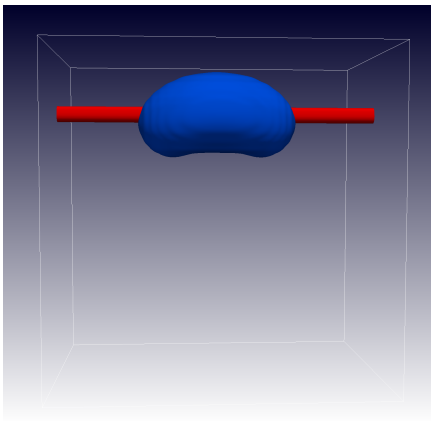

(e) The smallest part disappears and the largest continues to grow, $t =$ 49.75 hours.

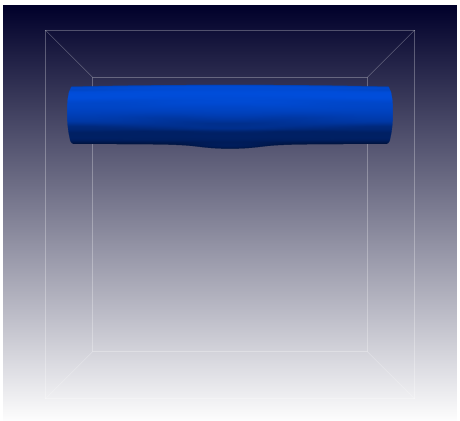

(f) The tumor completely surrounds the vessel and keeps the layer size constant, $t = 385.91$ hours.

Figure 6.26 – Tumor development in the vicinity of a straight vessel during a 385.91 hours simulation. Tumor in blue and vase in red.

A greater thickness of the tumor in the central region, can be seen in Fig. 6.26(f). Applying transparency filter to the tumor layer, we reveal a similar behavior in the vessel, see Fig. 6.27(a). This observed phenomenon can be eliminated by modifying one of the equations in system (4.1)-(4.4). More precisely by eliminating term $\mathcal{B}_p(f)c\mathcal{H}(c)$ from Eq. (4.2). The elimination of this term makes Eq. (4.2) conservative, maintaining the initial shape of the vessel throughout the simulation. Figure 6.27(b) shows the end of a new simulation after the change.

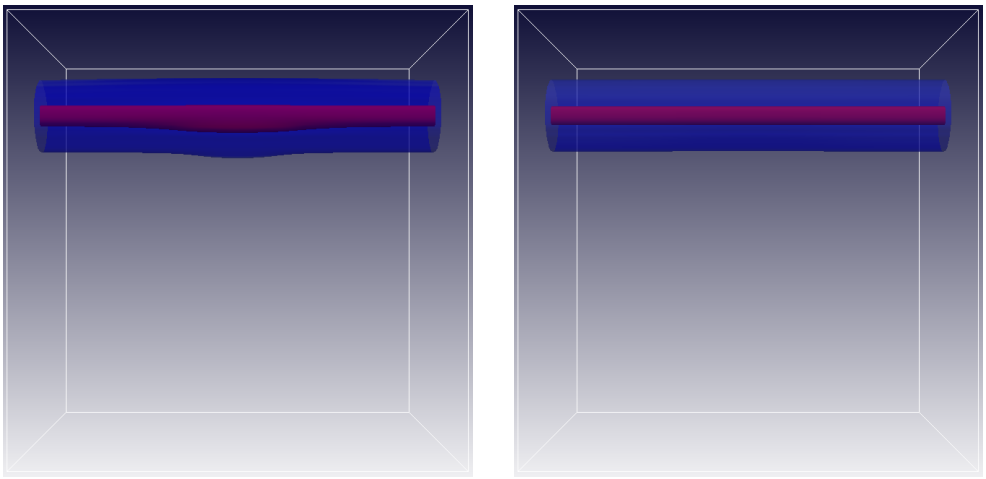

(a) Vessel shape at time $t = 385.91$, using original model.

(b) Vessel shape at time $t = 385.91$, eliminating the last term of equation (4.2).

Figure 6.27 – Comparison between the final results of the vessel in two simulations at time $t = 385.91$ hours: (a) Simulation using the original model(Xu et al., 2016) and (b) simulation using the model after eliminating the term $\mathcal{B}_p(f)c\mathcal{H}(c)$.

The division of the tumor into two parts, seen in Fig. 6.26(d), may be better understood by making a more detailed analysis of the distribution of nutrients over the domain. Figures 6.28(a)-(f) show the distribution of nutrients at the same moments recorded in Figs. 6.26(a)-(f). Looking at Fig. 6.28(c), we notice that the tumor region closest to the vessel consumes nutrients from the vessel and gains volume. The tumor region more distant the vessel has no access to this source of nutrients and loses volume. Figure 6.28(d) shows that, after the division of the tumor, one of the parts remains in a region with a low level of nutrients, losing volume until it disappears. In Fig. 6.28(b) we observe high levels of nutrient forming a constant layer around the vessel and part of that layer being consumed by the tumor. In the Figs. 6.28(c)-(f), we see the thickness of the layer decreasing as the tumor advances. At the end of the simulation (385.91h) a cylindrical tumor with a diameter of 150μm is formed covering the entire length of the vessel. The tumor is composed predominantly of a proliferative layer and covered by a thin layer of hypoxic cells. Figure 6.28(f) shows that, in addition to consuming nutrients from the vessel, the tumor cells consume nutrients that are around the tumor cord.

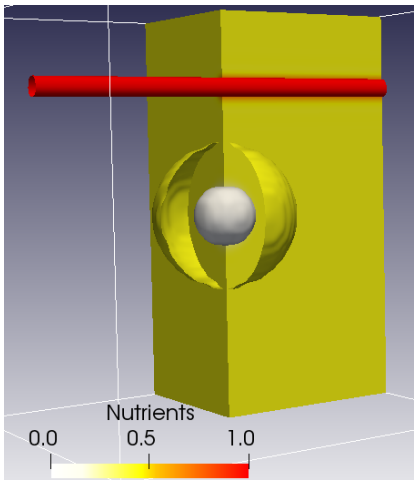

(a) Initial amounts of nutrients. The tumor is composed of a necrotic nucleus and a proliferative layer.

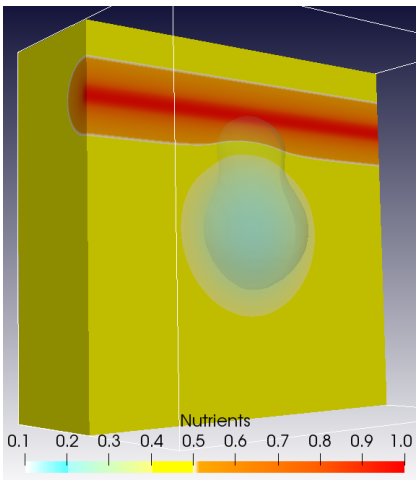

(b) Part of the tumor already feeds on nutrients that are in the vessel.

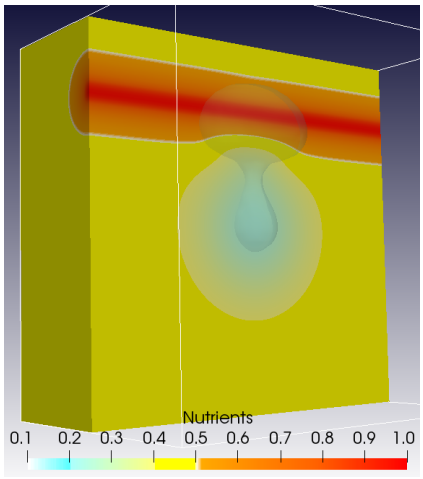

(c) The part of the tumor closest to the vessel increases in volume and the part further away decreases.

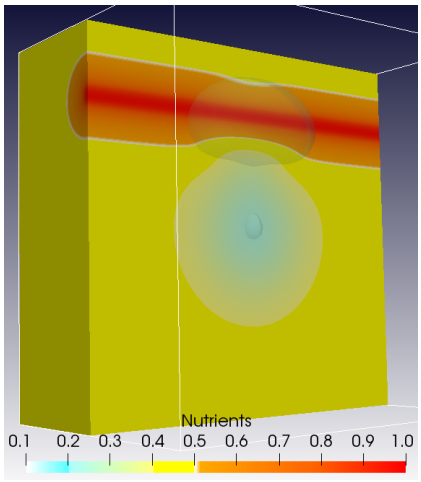

(d) The tumor divides and the smallest part occupies a region with a low level of nutrients.

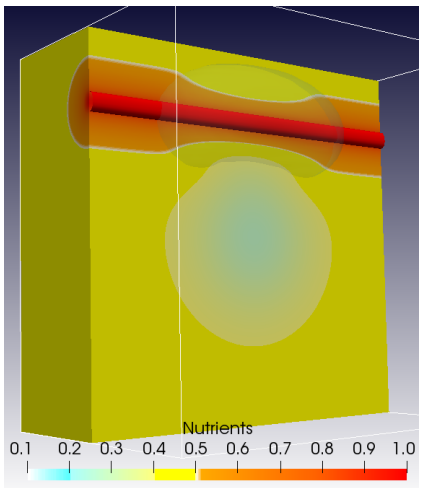

(e) With low levels of nutrients, the smallest part of the tumor disappears.

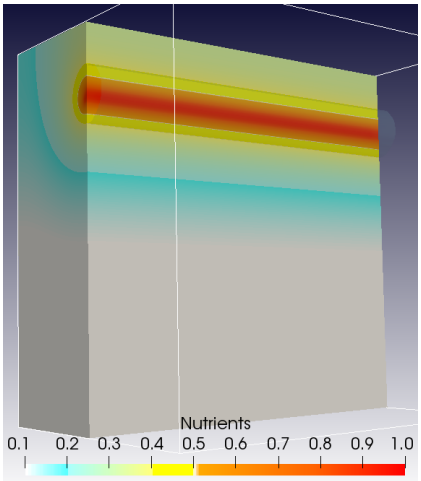

(f) The innermost part of the tumor becomes proliferative and the superficial layer hypoxic.

Figure 6.28 – Nutrient settings in the development of the cord tumor.

6.5.3 Tumor cord - Three-dimensional configuration with curvilinear tubular vessel

To conclude this section of experiments, we consider a spherical tumor with 200μm of radius at a distance of 112.3μm from a curvilinear tubular vessel, Fig. 6.29(a). The dimensions of the domain are $1000 \times 750 \times 1000\mu\text{m}^3$. As in previous experiments, the tumor initially develops symmetrically, consuming the nutrients available in the host tissue. Due to the proximity of the vessel, nutrients reach the tumor, promoting its growth, see Figs. 6.29(b) and (c). In Fig. 6.29(d) we see the tumor divided into two parts, one of them completely surrounding the vessel. The smaller part does not develop, disappearing completely in the next steps, see Fig. 6.29(e). In the end ($t = 198.99$h), the tumor assumes the shape of the pre-existing vessel, maintaining a constant layer along the vessel, as we can see in Fig. 6.29(f). The tumor cord formed has a constant diameter of 175μm. Like the two-dimensional experiment (Section 6.5.1), the evolution of the system reaches a steady state from the time $t = 140$hs.

This sequence of events was repeated in the three experiments that aimed to represent the tumor cord, regardless of the geometric shape of the vessel and the amount of dimensions of the domain.

Figures 6.30(a)-(f) show the distribution of nutrients in the moments referring to Figs. 6.29(a)-(f). In Fig. 6.30(a) we have the initial conditions of the simulation for the Nutrient, with level 1 (red) on capillary, 0 (white) on the necrotic core and 0.45 (yellow) on the rest of the domain. At time $t = 28.91$ hours, the lowest level of nutrients is found in the center of the tumor, however, according to the layer distinction adopted, this region is not considered necrotic, but hypoxic ($0.2 < \sigma \leqslant 0.4$), as can be seen in Fig. 6.30(b). Figure 6.30(c) shows that, the increase in the volume of the tumor region around the vessel and the decrease in the volume of the most distant region, occur due to the difference in the availability of nutrients in the regions. In Fig. 6.30(d) is shown that, the low level of nutrient available in one of the regions of the tumor prevents its development and causes its separation from the region that proliferates. Level 5 of nutrients is highlighted by a white layer that surrounds the vessel, indicating a radial symmetry in the diffusion of nutrients, see Fig. 6.30(b). We can see in Figs. 6.30(c)-(f) the decrease in the concentration of nutrients around the vessel, causing the retraction of the white layer, which marks the level 5 of nutrients. After $t = 198.99$ hours of simulation, the distribution of nutrients becomes radially symmetrical, obeying the geometry of the vessel and with a decreasing level of nutrients when moving away from the vessel.

We emphasize that the formation of the structure is due to the general dynamics, promoted by a unique system of equations, without the inclusion of any numerical device directing the behavior of the tumor field.

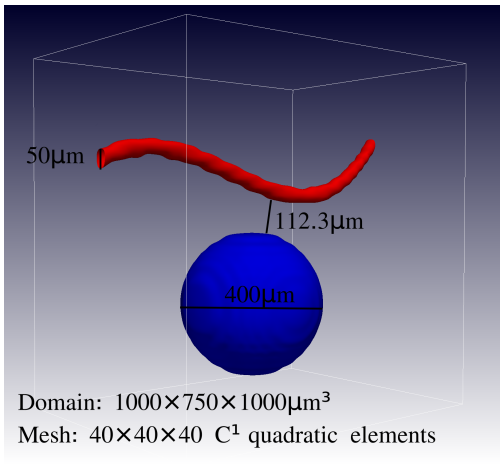

(a) Initial conditions for vessel and tumor.

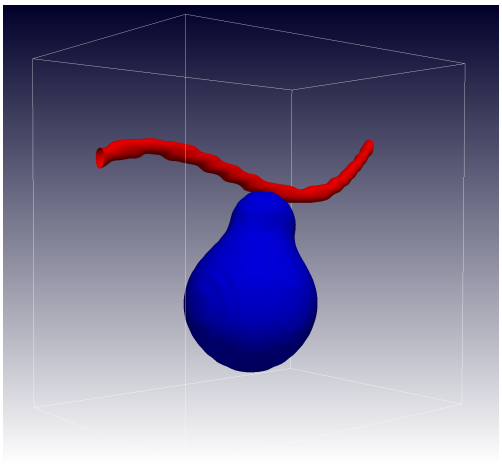

(b) Tumor growth towards the vessel, t = 28.91 hours.

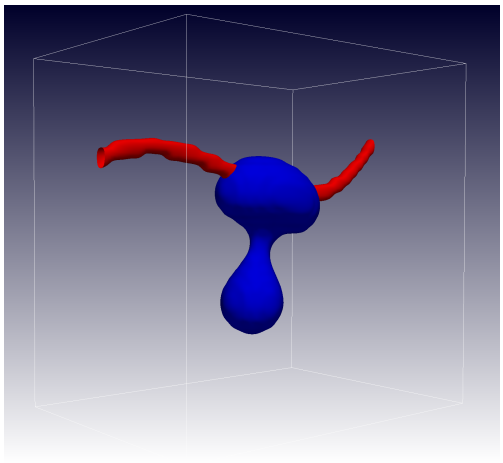

(c) Part of the tumor involves the vessel, t = 42.07 hours.

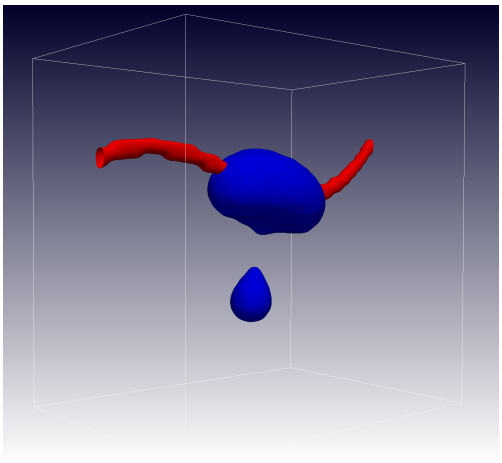

(d) The tumor separates into two parts, t = 45.30 hours.

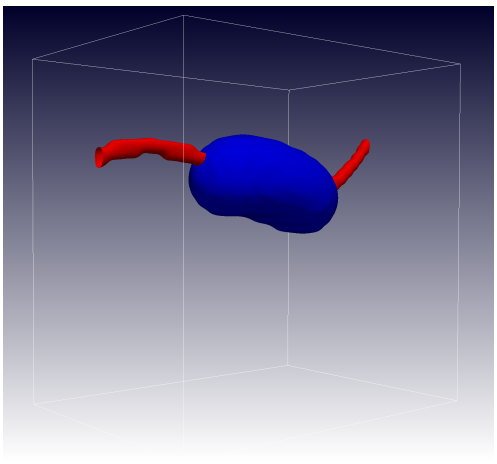

(e) The smallest part disappears and the largest continues to grow, t = 53.40 hours.

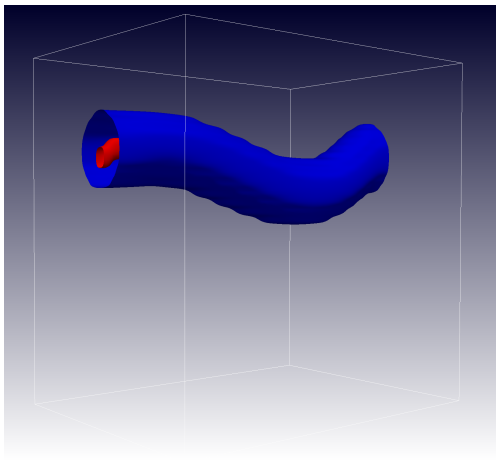

(f) The tumor completely surrounds the vessel, assuming its shape, t = 198.99 hours.

Figure 6.29 – Development of a tumor in the vicinity of a curved tubular vessel. Tumor in blue and vase in red.

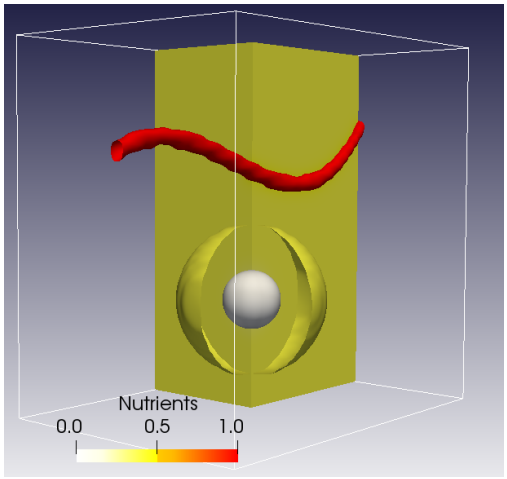

(a) Initial amounts of nutrients. The tumor is composed of a necrotic nucleus and a proliferative layer, $t = 0$ hour.

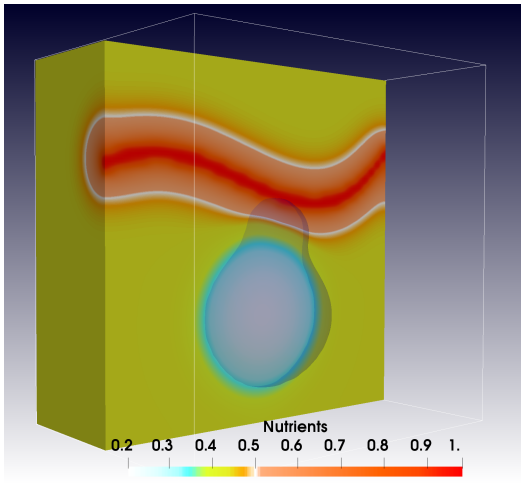

(b) Part of the tumor already feeds on nutrients that are in the vessel, $t = 28.91$ hours.

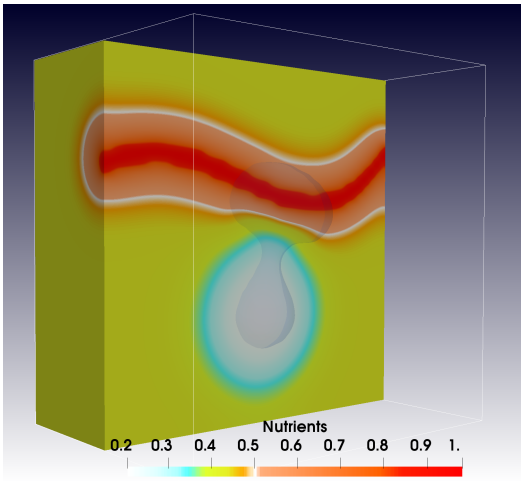

(c) The part of the tumor closest to the vessel increases in volume and the part further away decreases, $t = 42.07$ hours.

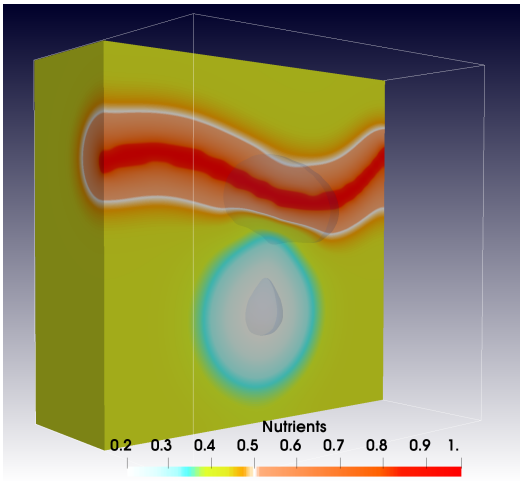

(d) The tumor divides and the smallest part occupies a region with a low level of nutrients, $t = 45.30$ hours.

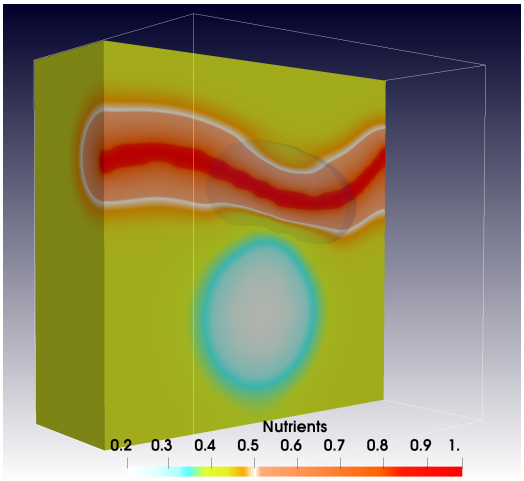

(e) With low levels of nutrients, the smallest part of the tumor disappears, $t = 53.40$ hours.

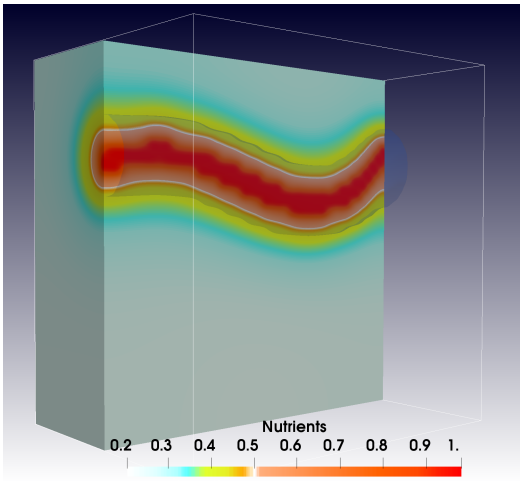

(f) The innermost part of the tumor becomes proliferative and the superficial layer hypoxic, $t = 198.99$ hours.

Figure 6.30 – Nutrient settings in the development of the cord tumor.

The experiments carried out in Section 6.1 showed that, without the arrival of a new source of nutrients, the tumor consumes the nutrients available around it and, after a small growth, it shrinks in size until it disappears. We evaluated that the total disappearance of the tumor is a flaw in the model and can be corrected with the inclusion of mechanisms that can demarcate and maintain its position. Modifying the shape of the chemical potential μ_ϕ or adding new phase-fields are two viable options. Therefore, without the activation of angiogenesis, the distance between tumor and vessel is essential. Tumor regions close to the vessel receive a greater amount of nutrients, when they reach levels above 0.4, proliferation occurs. If a region of the tumor remains with nutrient levels below 0.4 it will disappear over time, as we saw in all experiments performed in Section 6.5. In addition to the distance between the vessel and the tumor, the speed of diffusion of nutrients and the speed at which the tumor loses volume are important parameters, and they must be well calibrated because, in this model, they contribute to the growth or extinction of the tumor.

7 CONCLUDING REMARKS

The goal of this thesis was to study of development and numerical solution of phase-field based tumor growth models using isogeometric analysis for the implementation of the models consisting of a system of fourth-order partial differential equations, with good results in 2D and 3D. The use of C^1 continuous basis functions allowed the direct use of a primal formulation of the equations. In terms of biological significance, the two models studied, the mechanical and the phenomenological, addresses two main aspects of the *in vivo* tumor development, namely, the influence of stress fields on the tumor growth (since growth is constrained by the surrounding ECM), and the interaction between the tissue and cellular scales within the process of angiogenesis, marking the transition from avascular to vascular phases, respectively.

Numerical experiments have shown that our implementation of the phenomenological model is capable of representing the growth of tumors in the avascular phase and the recruitment of a capillary network to trigger the vascular phase. We observed that the behavior of the constituents of the fluid, nutrient and TAF, and their interaction with the tumor and the vessel, can be improved. The control of tumor layers, carried out according to the concentration of nutrients, caused unexpected results. As revealed by suppressing angiogenesis in the model, tumors far from the vessel disappear over time. On the other hand, tumors close to the vessel lose the necrotic nucleus with the arrival of nutrients. The inclusion of the conductivity tensor gave the model the capacity of a more realistic formation of the capillary network. In addition, we also observed that, the model may represent the branching of new vessels in the newly created capillary network. The geometric shapes of the pre-existing vessels, as well as the dimension of the domain, did not interfere in the dynamics of the model, but the distance from the tumor to the vessel is fundamental in the behavior of tumor growth.

The placement of the tumor and the vessel at a distance of less than 120μm and the inhibition of angiogenesis, provided the growth of the tumor towards the vessel, generating a behavior similar to the tumoral cord. The evolution of the system towards a steady state, forming a layer with constant thickness throughout the entire vessel, indicates that the model can describe one of the characteristics of the tumor cord. The distribution of nutrients in the internal part of the tumor, with a decreasing level when moving away from the vessel, are also in accordance with the characteristics of the tumor cord. The necrotic layer, which usually covers the tumor cord, was not observed in the experiments. The lack of an external necrotic layer can be corrected with a small change in the levels of nutrients required for the characterization of the layers.

We consider that the implemented phenomenological model was successful in simulating various events in the tumor environment, but we suggest some changes. The main change is the inclusion of a controller for the size of the necrotic zone, with the option of preventing its total disappearance. This control will be very useful, especially in modeling the tumor cord. The second suggestion would be to include a controller for the radius of the tip cells, giving the option to decrease their radius after the capillary comes into contact with the tumor. This control can help to simulate the pressure exerted by the tumor tissue in the internal vessels. The scales of time and space, as well as some parameters of speed and diffusion, must be calibrated according to the implementation proposed.

With respect to the implementation, the structure of PetIGA, an isogeometric analysis framework based on PETSc, facilitated the implementation of the phenomenological model, as the PETSc library provides the whole necessary stack beginning with distributed vector and sparse matrix data structures, preconditioners, linear solvers (direct and iterative), non-linear solvers, and time integration methods with adaptive time step control. The library has several function pointers that the user can intervene and add functionality. Using the *TSSetPreStep* function, the discrete part was inserted between the time steps by calling the agent-based model, that was implemented in C/C++ languages and using STL data structures, achieving good interaction with the continuous part of the model.

The mechanical model for tumor growth, presented in Chapter 5, is based on (Oden et al., 2010) and Faghihi et al. (2018). Using a generalized mixture theory, each constituent phase of the model were marked by a (scalar) concentration function with smooth but steep transitions, the so called phase-fields. As usual in the Continuum Mechanics framework, the energy balance, the second law of thermodynamics, and the novel microforce balance, were used in the formulation of the main constitutive equations, guaranteeing a thermodynamically consistent model, that consists of two mass balance equations, of the Cahn-Hilliard type, two force balance equations and a transport equation for the deformation gradient, this last one introduced to accommodate the Lagragian part of the model in an Eulerian description. With appropriate initial and boundary conditions, we believe that this model, in addition to describing tumor growth, can collaborate with the study of the influence of stress on the growth of solid tumors. The inhibition of tumor growth, imposed by the resistance of the host tissue, will be also the focus of studies with this model.

Our next steps are: the implementation of the mechanical model of four species, inclusion of mechanical forces in the phenomenological model and the calibration of the models using clinical data. For the phenomenological model, we intent to develop the incorporation of the movement of the tip cells in the continuous system. Also, we believe that, the decrease in the radius of the tip cell and the thickness of the capillaries

in the intra-tumor regions, in order to simulate the strangulation and collapse of the vessels, caused by the stress generated by growth can make the simulation more realistic. Furthermore, study on the penetration of drugs in solid tumors, analyzing the behavior of the tumor cord when the vessel in which it is supported receives some type of medication is another consideration to be taken into account.

A - APPENDIX TO CHAPTER 5

A.1 The Cauchy Tensor

Proposition 3. *Given the Neo-Hookean strain energy function*

$$W = \frac{G_T}{2}(\bar{I}_C^S - 3) + \frac{K_T}{2}(J_T^S - 1)^2 \tag{A.1}$$

the Cauchy tensor to the solid constituents will be

$$\mathbf{T}_T = \frac{1}{J_T^G}\left\{\frac{G_T}{(J_T^S)^{\frac{5}{3}}}\left[\mathbf{B}_T^S - \frac{1}{3}tr[\mathbf{B}_T^S]\mathbf{I}\right] + K_T(J_T^S - 1)\mathbf{I}\right\} - \epsilon\nabla\phi_T \otimes \nabla\phi_T \ + \Psi_T\mathbf{I} \tag{A.2}$$

where $\mathbf{B}_T^S = \mathbf{F}_T^S(\mathbf{F}_T^S)^T$.

Demonstration: Taking the derivatives of J_T^S and $\bar{I}_C^S$ in relation to $\mathbf{F}_T^S$ we will have

$$\frac{\partial J_T^S}{\partial \mathbf{F}_T^S} = \frac{\partial \det[\mathbf{F}_T^S]}{\partial \mathbf{F}_T^S} = \det[\mathbf{F}_T^S](\mathbf{F}_T^S)^{-T} = J_T^S(\mathbf{F}_T^S)^{-T} \tag{A.3}$$

and

$$\frac{\partial \bar{I}_C^S}{\partial \mathbf{F}_T^S} = \frac{\partial (J_T^S)^{-\frac{2}{3}}}{\partial \mathbf{F}_T^S}tr[(\mathbf{F}_T^S)^T\mathbf{F}_T^S] + (J_T^S)^{-\frac{2}{3}}\frac{\partial\ tr[(\mathbf{F}_T^S)^T\mathbf{F}_T^S]}{\partial \mathbf{F}_T^S} \tag{A.4}$$

$$= -\frac{2}{3}(J_T^S)^{-\frac{5}{3}}J_T^S(\mathbf{F}_T^S)^{-T}tr[(\mathbf{F}_T^S)^T\mathbf{F}_T^S] + (J_T^S)^{-\frac{2}{3}}2\mathbf{F}_T^S\frac{\partial\ tr[\mathbf{C}_T^S]}{\partial \mathbf{C}_T^S} \tag{A.5}$$

$$= -\frac{2}{3}(J_T^S)^{-\frac{2}{3}}(\mathbf{F}_T^S)^{-T}tr[(\mathbf{F}_T^S)^T\mathbf{F}_T^S] + 2(J_T^S)^{-\frac{2}{3}}\mathbf{F}_T^S \tag{A.6}$$

$$= 2(J_T^S)^{-\frac{2}{3}}\left[\mathbf{F}_T^S - \frac{1}{3}(\mathbf{F}_T^S)^{-T}tr[(\mathbf{F}_T^S)^T\mathbf{F}_T^S]\right]. \tag{A.7}$$

The derivatives of W in relation to $\mathbf{F}_T^S$ will be

$$\frac{\partial W}{\partial \mathbf{F}_T^S} = \frac{G_T}{2}\frac{\partial \bar{I}_C^S}{\partial \mathbf{F}_T^S} + K_T(J_T^S - 1)\frac{\partial J_T^S}{\partial \mathbf{F}_T^S} \tag{A.8}$$

$$= \frac{G_T}{2}\left\{2(J_T^S)^{-\frac{2}{3}}\left[\mathbf{F}_T^S - \frac{1}{3}(\mathbf{F}_T^S)^{-T}tr[(\mathbf{F}_T^S)^T\mathbf{F}_T^S]\right]\right\} + K_T(J_T^S - 1)J_T^S(\mathbf{F}_T^S)^{-T} \tag{A.9}$$

$$= \left\{G_T(J_T^S)^{-\frac{5}{3}}\left[\mathbf{F}_T^S(\mathbf{F}_T^S)^T - \frac{1}{3}tr[(\mathbf{F}_T^S)^T\mathbf{F}_T^S]\mathbf{I}\right] + K_T(J_T^S - 1)\mathbf{I}\right\}J_T^S(\mathbf{F}_T^S)^{-T} \tag{A.10}$$

$$= \left\{G_T(J_T^S)^{-\frac{5}{3}}\left[\mathbf{F}_T^S(\mathbf{F}_T^S)^T - \frac{1}{3}tr[\mathbf{F}_T^S\left(\mathbf{F}_T^S\right)^T]\mathbf{I}\right] + K_T(J_T^S - 1)\mathbf{I}\right\}J_T^S(\mathbf{F}_T^S)^{-T} \tag{A.11}$$

$$= \left\{G_T(J_T^S)^{-\frac{5}{3}}\left[\mathbf{B}_T^S - \frac{1}{3}tr[\mathbf{B}_T^S]\mathbf{I}\right] + K_T(J_T^S - 1)\mathbf{I}\right\}J_T^S(\mathbf{F}_T^S)^{-T} \tag{A.12}$$

$$= \left\{\frac{G_T}{(J_T^S)^{\frac{5}{3}}}\left[\mathbf{B}_T^S - \frac{1}{3}tr[\mathbf{B}_T^S]\mathbf{I}\right] + K_T(J_T^S - 1)\mathbf{I}\right\}J_T^S(\mathbf{F}_T^S)^{-T} \tag{A.13}$$

$$\frac{\partial W}{\partial \mathbf{F}_T^S} = \left\{ \frac{G_T}{(J_T^S)^{\frac{5}{3}}} \left[\mathbf{B}_T^S - \frac{1}{3} tr[\mathbf{B}_T^S]\mathbf{I} \right] + K_T(J_T^S - 1)\mathbf{I} \right\} J_T^S (\mathbf{F}_T^S)^{-T}. \tag{A.14}$$

Substituting (A.14) at (5.59) we get the result

$$\begin{aligned}
\mathbf{T}_T &= \frac{1}{J_T^S J_T^G} \frac{\partial W_T}{\partial \mathbf{F}_T^S} \left(\mathbf{F}_T^S\right)^T - \epsilon \nabla\phi_T \otimes \nabla\phi_T \ + \Psi_T \mathbf{I} \\
&= \frac{1}{J_T^S J_T^G} \left\{ \left\{ \frac{G_T}{(J_T^S)^{\frac{5}{3}}} \left[\mathbf{B}_T^S - \frac{1}{3} tr[\mathbf{B}_T^S]\mathbf{I} \right] + K_T(J_T^S - 1)\mathbf{I} \right\} J_T^S (\mathbf{F}_T^S)^{-T} \right\} \left(\mathbf{F}_T^S\right)^T \\
&\quad - \epsilon \nabla\phi_T \otimes \nabla\phi_T \ + \Psi_T \mathbf{I} \\
&= \frac{1}{J_T^G} \left\{ \frac{G_T}{(J_T^S)^{\frac{5}{3}}} \left[\mathbf{B}_T^S - \frac{1}{3} tr[\mathbf{B}_T^S]\mathbf{I} \right] + K_T(J_T^S - 1)\mathbf{I} \right\} - \epsilon \nabla\phi_T \otimes \nabla\phi_T \ + \Psi_T \mathbf{I}
\end{aligned} \tag{A.15}$$

A.2 The derivative of Ψ_T^{els} with respect to ϕ_T

Demonstration of (5.74).

$$\frac{\partial \Psi_T^{els}}{\partial \phi_T} = \frac{\partial \Lambda_T^G}{\partial \phi_T} \left(\hat{\mathbf{T}}_T^{en} \mathbf{F}_T^{-T} : \mathbf{F}_T^S \right) \tag{A.16}$$

Demonstration:

From (5.34) we have

$$\frac{\partial \Psi_T^{els}}{\partial \mathbf{F}_T} = \hat{\mathbf{T}}_T^{en} \mathbf{F}_T^{-T}, \tag{A.17}$$

and from $\mathbf{F}_T = \mathbf{F}_T^S \mathbf{F}_T^G$ we have

$$\frac{\partial \mathbf{F}_T}{\partial \mathbf{F}_T^G} = \mathbf{F}_T^S \otimes \mathbf{I} \,, \tag{A.18}$$

so

$$\begin{aligned}
\frac{\partial \Psi_T^{els}}{\partial \phi_T} &= \frac{\partial \Psi^{els}}{\partial \mathbf{F}_T} : \frac{\partial \mathbf{F}_T}{\partial \mathbf{F}_T^G} : \frac{\partial \mathbf{F}_T^G}{\partial \phi_T} \\
&= \hat{\mathbf{T}}_T^{en} \mathbf{F}_T^{-T} : \left[\mathbf{F}_T^S \otimes \mathbf{I} \right] : \frac{\partial \mathbf{F}_T^G}{\partial \phi_T} \\
&= \mathbf{I} \left(\hat{\mathbf{T}}_T^{en} \mathbf{F}_T^{-T} : \mathbf{F}_T^S \right) : \frac{\partial \mathbf{F}_T^G}{\partial \phi_T} \\
&= \left(\mathbf{I} : \frac{\partial \mathbf{F}_T^G}{\partial \phi_T} \right) \left(\hat{\mathbf{T}}_T^{en} \mathbf{F}_T^{-T} : \mathbf{F}_T^S \right) \\
&= \frac{\partial \Lambda_T^G}{\partial \phi_T} \left(\hat{\mathbf{T}}_T^{en} \mathbf{F}_T^{-T} : \mathbf{F}_T^S \right) \,.
\end{aligned} \tag{A.19}$$

A.3 Relationship between material derivatives of $\mathbf{v}$ and $\mathbf{v}_\alpha$

Demonstration of (2.48).

$$\rho\frac{d\mathbf{v}}{dt} = \sum\left[\rho_\alpha\phi_\alpha\frac{d^\alpha\mathbf{v}_\alpha}{dt} - \nabla\cdot(\rho_\alpha\phi_\alpha\mathbf{v}_\alpha\otimes\mathbf{u}_\alpha) + \mathbf{v}_\alpha\left(S_\alpha - \nabla\cdot\mathbf{J}_\alpha\right)\right] \tag{A.20}$$

Demonstration:

Given the relation

$$\mathbf{v} = \frac{1}{\rho}\sum_{\alpha=1}^{N}\rho_\alpha\phi_\alpha\mathbf{v}_\alpha, \tag{A.21}$$

using mass concentration (2.29) we can rewrite

$$\mathbf{v} = \sum_{\alpha=1}^{N}\frac{\rho_\alpha\phi_\alpha}{\rho}\mathbf{v}_\alpha = \sum c_\alpha\mathbf{v}_\alpha \tag{A.22}$$

whose derivative is given by

$$\begin{aligned}\frac{d\mathbf{v}}{dt} &= \sum\frac{d(c_\alpha\mathbf{v}_\alpha)}{dt}\\ &= \sum\left[c_\alpha\frac{d\mathbf{v}_\alpha}{dt} + \mathbf{v}_\alpha\frac{dc_\alpha}{dt}\right],\end{aligned} \tag{A.23}$$

multiplying equality for ρ

$$\rho\frac{d\mathbf{v}}{dt} = \sum\left[\rho_\alpha\phi_\alpha\frac{d\mathbf{v}_\alpha}{dt} + \mathbf{v}_\alpha\rho\frac{dc_\alpha}{dt}\right] \tag{A.24}$$

from (2.36) and (2.45) we have

$$\begin{aligned}\rho\frac{d\mathbf{v}}{dt} &= \sum\left[\rho_\alpha\phi_\alpha\left(\frac{d^\alpha\mathbf{v}_\alpha}{dt} - (\nabla\mathbf{v}_\alpha)\mathbf{u}_\alpha\right) + \mathbf{v}_\alpha\left(S_\alpha - \nabla\cdot\mathbf{J}_\alpha - \nabla\cdot(\rho_\alpha\phi_\alpha\mathbf{u}_\alpha)\right)\right]\\ &= \sum\left[\rho_\alpha\phi_\alpha\frac{d^\alpha\mathbf{v}_\alpha}{dt} - (\nabla\mathbf{v}_\alpha)(\rho_\alpha\phi_\alpha\mathbf{u}_\alpha) - \nabla\cdot(\rho_\alpha\phi_\alpha\mathbf{u}_\alpha)\mathbf{v}_\alpha + \mathbf{v}_\alpha\left(S_\alpha - \nabla\cdot\mathbf{J}_\alpha\right)\right]\\ &= \sum\left[\rho_\alpha\phi_\alpha\frac{d^\alpha\mathbf{v}_\alpha}{dt} - \nabla\cdot(\rho_\alpha\phi_\alpha\mathbf{v}_\alpha\otimes\mathbf{u}_\alpha) + \mathbf{v}_\alpha\left(S_\alpha - \nabla\cdot\mathbf{J}_\alpha\right)\right],\end{aligned} \tag{A.25}$$

that demonstrate the result.

A.4 New relationship between material derivatives of $\mathbf{v}$ and $\mathbf{v}_\alpha$

Demonstration of (2.49).

$$\rho\frac{d\mathbf{v}}{dt} = \sum\left[\rho_\alpha\phi_\alpha\frac{d^\alpha\mathbf{v}_\alpha}{dt} - \nabla\cdot(\rho_\alpha\phi_\alpha\mathbf{u}_\alpha\otimes\mathbf{u}_\alpha) + \mathbf{u}_\alpha\left(S_\alpha - \nabla\cdot\mathbf{J}_\alpha\right)\right] \tag{A.26}$$

Demonstration: The relation (2.48) can be rewritten by substituting $\mathbf{v}_\alpha$ for $\mathbf{u}_\alpha + \mathbf{v}$ in the last two terms of the second member, obtaining

$$\begin{aligned}\rho\frac{d\mathbf{v}}{dt} &= \sum\left[\rho_\alpha\phi_\alpha\frac{d^\alpha\mathbf{v}_\alpha}{dt} - \nabla\cdot(\rho_\alpha\phi_\alpha(\mathbf{u}_\alpha+\mathbf{v})\otimes\mathbf{u}_\alpha) + (\mathbf{u}_\alpha+\mathbf{v})\left(S_\alpha - \nabla\cdot\mathbf{J}_\alpha\right)\right]\\ &= \sum\left[\rho_\alpha\phi_\alpha\frac{d^\alpha\mathbf{v}_\alpha}{dt} - \nabla\cdot(\rho_\alpha\phi_\alpha\mathbf{u}_\alpha\otimes\mathbf{u}_\alpha) + \mathbf{u}_\alpha\left(S_\alpha - \nabla\cdot\mathbf{J}_\alpha\right)\right]\\ &\quad - \sum\left[\nabla\cdot(\rho_\alpha\phi_\alpha\mathbf{v}\otimes\mathbf{u}_\alpha)\right] + \mathbf{v}\sum\left(S_\alpha - \nabla\cdot\mathbf{J}_\alpha\right)\end{aligned} \tag{A.27}$$

applying the product rule in the second sum we have

$$\nabla\cdot(\rho_\alpha\phi_\alpha\mathbf{v}\otimes\mathbf{u}_\alpha) = [\nabla\mathbf{v}]\rho_\alpha\phi_\alpha\mathbf{u}_\alpha + \nabla\cdot(\rho_\alpha\phi_\alpha\mathbf{u}_\alpha)\,\mathbf{v} \tag{A.28}$$

$$\begin{aligned}\sum\left[\nabla\cdot(\rho_\alpha\phi_\alpha\mathbf{v}\otimes\mathbf{u}_\alpha)\right] &= [\nabla\mathbf{v}]\sum\rho_\alpha\phi_\alpha\mathbf{u}_\alpha + \nabla\cdot\left(\sum\rho_\alpha\phi_\alpha\mathbf{u}_\alpha\right)\mathbf{v}\\ &= [\nabla\mathbf{v}]\mathbf{0} + \nabla\cdot(\mathbf{0})\,\mathbf{v}.\end{aligned} \tag{A.29}$$

using (A.29) and (2.42) in (A.27) we have the result

$$\rho\frac{d\mathbf{v}}{dt} = \sum\left[\rho_\alpha\phi_\alpha\frac{d^\alpha\mathbf{v}_\alpha}{dt} - \nabla\cdot(\rho_\alpha\phi_\alpha\mathbf{u}_\alpha\otimes\mathbf{u}_\alpha) + \mathbf{u}_\alpha\left(S_\alpha - \nabla\cdot\mathbf{J}_\alpha\right)\right]. \tag{A.30}$$

B - APPENDIX TO CHAPTER 6

B.1 Bidimensional configuration with two closer vessels

In this experiment a circular tumor of 200μm radius is placed in the center of a 1000μm side square domain, discretized by a mesh with 256 C^1 quadratic elements in each direction. At the top of the domain there is a straight vessel at a distance of 200μm from the tumor and at the bottom there is another at a distance of 237μm from the tumor, as shown in Fig. B.1(a).

Initially, the tumor consumes the nutrients around it, growing uniformly until its radius reaches 210.6μm. Growth occurs during $t = 14.95h$, increasing the area of the tumor region from $12.6 \times 10^4 \mu\text{m}^2$ to $13.9 \times 10^4 \mu\text{m}^2$. After this period, with the reduction in the supply of nutrients, the tumor region decreases in size, returning to its initial size after 27.88 hours of simulation. At that time, two capillaries already feed the tumor, yet their total area continues to decrease. The tumor reaches its minimum area of $11.7 \times 10^4 \mu\text{m}^2$ after 36.59 hours of simulation.

The first tip cell is activated in the upper vessel after 9.13 hours of simulation. Two other cells are activated in the upper vessel before the first cell is activated in the lower vessel, after 9.72 hours. The time taken for the first capillary born in the upper vessel to reach the tumor was $t = 26.83$ hours, while the capillary from the lower vessel spent $t = 34.46$ hours. In Fig. B.1(b) we can see capillaries feeding the tumor and new capillaries growing in their direction.

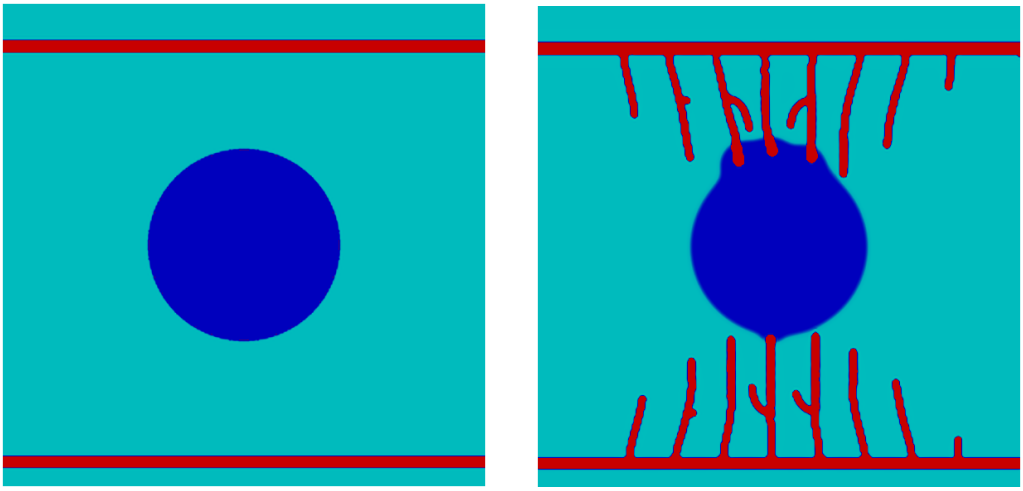

(a) Initial configuration of the vessel and tumor.

(b) Capillaries feeding the tumor, $t = 36.59h$.

Figure B.1 – The formation of the new capillary network.

The final behavior of the nutrient and the angiogenic factor are shown in Figs.B.2(a) and B.2(b).

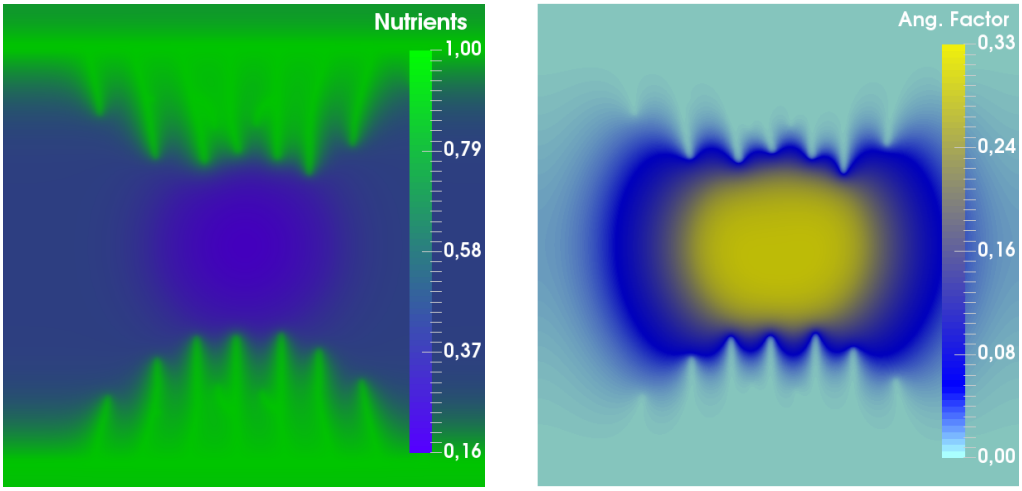

(a) Final configuration of σ.

(b) Final configuration of f.

Figure B.2 – Nutrient and angiogenic factor in the final configuration, $t = 36.59$h.

BIBLIOGRAPHY

AIRD, W. C. Endothelial cell heterogeneity. *Cold Spring Harbor Perspectives in Medicine*, v. 2, n. 1, p. 1–14, 2012. ISSN 21571422. <https://doi.org/10.1101/cshperspect.a006429>.

AKKERMAN, I.; BAZILEVS, Y.; CALO, V. M.; HUGHES, T. J. R.; HULSHOFF, S. The role of continuity in residual-based variational multiscale modeling of turbulence. *Computational Mechanics*, v. 41, n. 3, p. 371–378, dec 2007. ISSN 0178-7675. <http://link.springer.com/10.1007/s00466-007-0193-7>.

ALARCóN, T.; BYRNE, H.; MAINI, P. Towards whole-organ modelling of tumour growth. *Progress in Biophysics and Molecular Biology*, v. 85, n. 2, p. 451 – 472, 2004. ISSN 0079-6107. Modelling Cellular and Tissue Function. <http://www.sciencedirect.com/science/article/pii/S007961070400032X>.

AMBROSI, D.; ATESHIAN, G. A.; ARRUDA, E. M.; COWIN, S. C.; DUMAIS, J.; GORIELY, A.; HOLZAPFEL, G. A.; HUMPHREY, J. D.; KEMKEMER, R.; KUHL, E.; OLBERDING, J. E.; TABER, L. A.; GARIKIPATI, K. Perspectives on biological growth and remodeling. *Journal of the Mechanics and Physics of Solids*, v. 59, n. 4, p. 863–883, 2011. ISSN 00225096. <https://doi.org/10.1016/j.jmps.2010.12.011>.

AMBROSI, D.; MOLLICA, F. On the mechanics of a growing tumor. *International Journal of Engineering Science*, v. 40, n. 12, p. 1297–1316, jul 2002. ISSN 00207225. <https://linkinghub.elsevier.com/retrieve/pii/S0020768302003529https://linkinghub.elsevier.com/retrieve/pii/S0020722502000149>.

AMBROSI, D.; PREZIOSI, L.; VITALE, G. The insight of mixtures theory for growth and remodeling. *Zeitschrift für angewandte Mathematik und Physik*, v. 61, n. 1, p. 177–191, feb 2010. ISSN 0044-2275. <http://link.springer.com/10.1007/s00033-009-0037-8>.

ARAUJO, R. P.; MCELWAIN, D. L. S. A history of the study of solid tumour growth: The contribution of mathematical modelling. *Bulletin of Mathematical Biology*, v. 66, n. 5, p. 1039–1091, 2004. ISSN 00928240. <https://doi.org/10.1016/j.bulm.2003.11.002>.

ARAUJO, R. P.; MCELWAIN, D. L. S. A Mixture Theory for the Genesis of Residual Stresses in Growing Tissues I: A General Formulation. *SIAM Journal on Applied Mathematics*, v. 65, n. 4, p. 1261–1284, jan 2005. ISSN 0036-1399. <http://epubs.siam.org/doi/10.1137/040607113>.

ASTANIN, P.; TOSIN, A. Mathematical model of tumour cord growth along the source of nutrient. *Mathematical Modelling of Natural Phenomena*, v. 2, n. 3, p. 153–177, 2007. ISSN 09735348. <https://doi.org/10.1051/mmnp:2007007>.

ASTANIN, S.; PREZIOSI, L. Mathematical modelling of the Warburg effect in tumour cords. *Journal of Theoretical Biology*, v. 258, p. 578–590, 2009. <https://doi.org/10.1016/j.jtbi.2009.01.034>.

ATESHIAN, G. A.; HUMPHREY, J. D. Continuum Mixture Models of Biological Growth and Remodeling: Past Successes and Future Opportunities. *Annual Review of Biomedical*

Engineering, v. 14, n. 1, p. 97–111, 2012. ISSN 1523-9829. <http://www.annualreviews.org/doi/10.1146/annurev-bioeng-071910-124726>.

BALAY, S.; ABHYANKAR, S.; ADAMS, M. F.; BROWN, J.; BRUNE, P.; BUSCHELMAN, K.; DALCIN, L.; EIJKHOUT, V.; GROPP, W. D.; KAUSHIK, D.; KNEPLEY, M. G.; MCINNES, L. C.; RUPP, K.; SMITH, B. F.; ZAMPINI, S.; ZHANG, H.; ZHANG, H. *PETSc Users Manual*. Argonne National Laboratory, 2016. 273 p. <http://www.mcs.anl.gov/petsc>.

BALDING, D.; MCELWAIN, D. A mathematical model of tumour-induced capillary growth. *Journal of Theoretical Biology*, v. 114, n. 1, p. 53 – 73, 1985. ISSN 0022-5193. <http://www.sciencedirect.com/science/article/pii/S0022519385802551>.

BARBOSA, P. W.; De Côtes, A. M.; CATABRIGA, L. Studies of a Hybrid and Multiscale Tumor Growth Model via Isogeometric Analysis using PetIGA. *Proceedings - 2017 IEEE 17th International Conference on Bioinformatics and Bioengineering, BIBE 2017*, v. 2018-Janua, p. 69–74, 2017. <https://ieeexplore.ieee.org/document/8251268>.

BAZILEVS, Y.; CALO, V. M.; COTTRELL, J. A.; HUGHES, T. J.; REALI, A.; SCOVAZZI, G. Variational multiscale residual-based turbulence modeling for large eddy simulation of incompressible flows. *Computer Methods in Applied Mechanics and Engineering*, v. 197, n. 1-4, p. 173–201, 2007. ISSN 00457825. <https://doi.org/10.1016/j.cma.2007.07.016>.

BAZILEVS, Y.; CALO, V. M.; ZHANG, Y.; HUGHES, T. J. Isogeometric fluid-structure interaction analysis with applications to arterial blood flow. *Computational Mechanics*, v. 38, n. 4-5, p. 310–322, 2006. ISSN 01787675. <https://doi.org/10.1007/s00466-006-0084-3>.

BAZILEVS, Y.; HSU, M.; KIENDL, J.; WÜCHNER, R.; BLETZINGER, K. 3D Simulation of Wind Turbine Rotors at Full Scale. Part II: Fluid – Structure Interaction Modeling with Composite Blades. *International Journal for Numerical Methods in Fluids*, v. 65, n. October 2010, p. 236–253, 2011. ISSN 02712091. <https://doi.org/10.1002/fld.2454>.

BAZILEVS, Y.; HSU, M. C.; SCOTT, M. A. Isogeometric fluid-structure interaction analysis with emphasis on non-matching discretizations, and with application to wind turbines. *Computer Methods in Applied Mechanics and Engineering*, Elsevier B.V., v. 249-252, p. 28–41, 2012. ISSN 00457825. <http://dx.doi.org/10.1016/j.cma.2012.03.028>.

BELLOMO, N.; LI, N. K.; MAINI, P. K. On the foundations of cancer modelling: selected topics, speculations, and perspectives. *Mathematical Models and Methods in Applied Sciences*, v. 18, n. 4, p. 593–646, 2008. <https://doi.org/10.1142/S0218202508002796>.

BELYTSCHKO, T.; KAM, W.; MORAN, B.; ELKHODARY, K. I. *Nonlinear finite elements for continua and structures*. 2nd. ed. Wiley, 2014. 830 p. ISSN 0009-4978. ISBN 9781118632703. <https://www.wiley.com//legacy/wileychi/belytschko{_}nonline>.

BENSON, D. J.; BAZILEVS, Y.; DELUYCKER, E.; HSU, M.-C.; SCOTT, M.; HUGHES, T. J. R.; BELYTSCHKO, T. A generalized finite element formulation for arbitrary basis functions: from isogeometric analysis to XFEM. *International Journal for Numerical Methods in Engineering*, v. 83, n. 6, p. 765–785, 2010. <https://doi.org/10.1002/nme.2864>.

BENSON, D. J.; HARTMANN, S.; BAZILEVS, Y.; HSU, M. C.; HUGHES, T. J. Blended isogeometric shells. *Computer Methods in Applied Mechanics and Engineering*, Elsevier B.V., v. 255, p. 133–146, 2013. ISSN 00457825. <http://dx.doi.org/10.1016/j.cma.2012.11.020>.

BERTUZZI, A.; FASANO, A.; GANDOLFI, A. A free boundary problem with unilateral constraints describing the evolution of a tumour cord under the influence of cell killing agents. *SIAM Journal on Mathematical Analysis*, v. 36, n. 3, p. 882–915, 2004. ISSN 00361410. <https://doi.org/10.1137/S003614002406060>.

BERTUZZI, A.; FASANO, A.; GANDOLFI, A.; MARANGI, D. Cell kinetics in tumour cords studied by a model with variable cell cycle length. *Mathematical Biosciences*, v. 178, p. 103–125, 2002. <https://doi.org/10.1016/S0025-5564(01)00114-6>.

BERTUZZI, A.; GANDOLFI, A. Cell Kinetics in a Tumor Cord. *Journal of Theoretical Biology*, v. 204, p. 587–599, 2000. ISSN 00225193. <https://doi.org/10.1006/jtbi.2000.1079>.

BORDEN, M. J.; VERHOOSEL, C. V.; SCOTT, M. A.; HUGHES, T. J.; LANDIS, C. M. A phase-field description of dynamic brittle fracture. *Computer Methods in Applied Mechanics and Engineering*, Elsevier B.V., v. 217-220, p. 77–95, 2012. ISSN 00457825. <http://dx.doi.org/10.1016/j.cma.2012.01.008>.

BOWEN, R. M. Theory of Mixtures. *Continuum Physics - Mixtures and EM Field Theories*, v. 3, p. 9–135, 1976. <https://doi.org/10.1016/B978-0-12-240803-8.50017-7>.

BUSSOLINO, F.; JAIN, R.; BYRNE, H.; DROCHON, A.; MOLLICA, F.; AUDERO, E.; BELLOMO, N.; HERRERO, M.; SLEEMAN, B.; LELIEVRE, S.; AMBROSI, D.; NETTI, P.; ARAKELYAN, L.; VAINSTAIN, V.; AGUR, Z.; LEYRAT, A.; DUPERRAY, A.; VERDIER, C.; CHOTARD-GHODSNIA, R.; ANDERSON, A.; PLACHOT, C.; LEVINE, H.; BERTOTTI, M.; MOTTA, S.; CASTIGLIONE, F.; GINOSAR, Y.; DAUGULIS, P.; HARPAK, H.; MERBL, Y.; SELITSER, V.; KOGAN, Y.; ARESE, M.; GIRAUDO, E.; MARCHIO, S.; MITOLA, S.; PRIMO, L.; SERINI, G.; CHAPLAIN, M.; SAFER, H.; GROSS, L.; LENHART, S.; MAINI, P.; ETHERIDGE, A.; VOIT, E.; PREZIOSI, L. E. *Cancer Modelling and Simulation*. CRC Press, 2003. 452 p. ISBN 1-58488-361-8. <https://doi.org/10.1201/9780203494899>.

BYRNE, H. Modelling solid tumour growth using the theory of mixtures. *Mathematical Medicine and Biology*, v. 20, n. 4, p. 341–366, dec 2003. ISSN 1477-8599. <https://academic.oup.com/imammb/article-lookup/doi/10.1093/imammb/20.4.341>.

BYRNE, H.; PREZIOSI, L. Modelling solid tumour growth using the theory of mixtures. *Mathematical Medicine and Biology: A Journal of the IMA*, v. 20, n. 4, p. 341–366, 12 2003. ISSN 1477-8599. <https://doi.org/10.1093/imammb/20.4.341>.

BYRNE, H. M. Dissecting cancer through mathematics: from the cell to the animal model. *Nature Reviews Cancer*, v. 10, 2010. <https://doi.org/10.1038/nrc2808>.

CAPALDI, F. M. *Continuum mechanics: constitutive modeling of structural and biological materials*. Cambridge University Press, 2012. 343 p. ISBN 978-1-107-01181-6. <www.cambridge.org/9781107011816>.

CHAGNON, G.; OHAYON, J.; MARTIEL, J.-L.; FAVIER, D. Hyperelasticity Modeling for Incompressible Passive Biological Tissues. In: *Biomechanics of Living Organs*. Elsevier, 2017. p. 3–30. ISBN 9780128040096. <https://linkinghub.elsevier.com/retrieve/pii/C20150008322https://linkinghub.elsevier.com/retrieve/pii/B9780128040096000018>.

CHAPLAIN, M. A. J.; STUART, A. M. A Mathematical Model for the Diffusion of Tumour Angiogenesis Factor into the Surrounding Host Tissue. *Mathematical Medicine and Biology: A Journal of the IMA*, v. 8, n. 3, p. 191–220, 09 1991. ISSN 1477-8599. <https://doi.org/10.1093/imammb/8.3.191>.

CHAPLAIN, M. A. J.; STUART, A. M. A model mechanism for the chemotactic response of endothelial cells to tumour angiogenesis factor. *Mathematical Medicine and Biology: A Journal of the IMA*, v. 10, n. 3, p. 149–168, 09 1993. ISSN 1477-8599. <https://doi.org/10.1093/imammb/10.3.149>.

CHUNG, J.; HULBERT, G. A time integration algorithm for structural dynamics with improved numerical dissipation: the generalized-α method. *Journal of Applied Mechanics*, v. 60, n. 2, p. 371–375, 1993. <https://doi.org/10.1115/1.2900803>.

COLEMAN, B. D.; NOLL, W. Material symmetry and thermostatic inequalities in finite elastic deformations. *Archive for Rational Mechanics and Analysis*, v. 15, n. 2, p. 87–111, 1964. ISSN 00039527. <https://doi.org/10.1007/978-3-642-65817-4_10>.

CONCHA, F. A. *Solid-Liquid Separation in the Mining Industry*. Springer International Publishing, 2014. v. 105. ISBN 978-3-319-02483-7. <http://link.springer.com/10.1007/978-3-319-02484-4>.

COTTRELL, J.; REALI, A.; BAZILEVS, Y.; HUGHES, T. Isogeometric analysis of structural vibrations. *Computer Methods in Applied Mechanics and Engineering*, v. 195, n. 41-43, p. 5257–5296, 2006. ISSN 00457825. <https://linkinghub.elsevier.com/retrieve/pii/S0045782505005451>.

COTTRELL, J. A.; HUGHES, T. J. R.; BAZILEVS, Y. *Isogeometric Analysis*. Chichester, UK: John Wiley & Sons, Ltd, 2009. ISBN 9780470749081. <http://doi.wiley.com/10.1002/9780470749081>.

CRISTINI, V.; LI, X.; LOWENGRUB, J. S.; WISE, S. M. Nonlinear simulations of solid tumor growth using a mixture model: Invasion and branching. *Journal of Mathematical Biology*, v. 58, n. 4-5, p. 723–763, 2009. ISSN 03036812. <https://doi.org/10.1007/s00285-008-0215-x>.

CRISTINI, V.; LOWENGRUB, J. *Multiscale Modeling of Cancer: An Integrated Experimental and Mathematical Modeling Approach*. Cambridge University Press, 2010. ISBN 978-0-511-90069-3. <https://doi.org/10.1017/CBO9780511781452>.

DALCIN, L.; COLLIER, N.; VIGNAL, P.; CÔRTES, A. M. A.; CALO, V. M. PetIGA: A framework for high-performance isogeometric analysis. *Computer Methods in Applied Mechanics and Engineering*, v. 308, p. 151–181, 2016. ISSN 00457825. <https://doi.org/10.1016/j.cma.2016.05.011>.

DARCY, H. Les fontaines publiques de la ville de dijon. *Dalmont*, 1856.

DEISBOECK, T. S.; WANG, Z.; MACKLIN, P.; CRISTINI, V. Multiscale Cancer Modeling. *Annual Review of Biomedical Engineering*, v. 13, n. 1, p. 127–155, 2011. PMID: 21529163. <https://doi.org/10.1146/annurev-bioeng-071910-124729>.

DUDDU, R.; LAVIER, L. L.; HUGHES, T. J. R.; CALO, V. M. A finite strain Eulerian formulation for compressible and nearly incompressible hyper- elasticity using higher-order NURBS elements by. *International Journal for Numerical Methods in Engineering*, v. 1, n. 1, p. 1–33, 2010. <https://doi.org/10.1002/nme.3262>.

ECHTER, R.; BISCHOFF, M. Numerical efficiency, locking and unlocking of NURBS finite elements. *Computer Methods in Applied Mechanics and Engineering*, Elsevier B.V., v. 199, n. 5-8, p. 374–382, 2010. ISSN 00457825. <http://dx.doi.org/10.1016/j.cma.2009.02.035>.

ELGUEDJ, T.; BAZILEVS, Y.; CALO, V. M.; HUGHES, T. J. over(B, -) and over(F, -) projection methods for nearly incompressible linear and non-linear elasticity and plasticity using higher-order NURBS elements. *Computer Methods in Applied Mechanics and Engineering*, v. 197, n. 33-40, p. 2732–2762, 2008. ISSN 00457825. <https://doi.org/10.1016/j.cma.2008.01.012>.

EPSTEIN, M. *The Elements of Continuum Biomechanics*. Cambridge University Press, 2012. 371 p. ISBN 9781119999232. <https://onlinelibrary.wiley.com/doi/book/10.1002/9781118361016>.

FAGHIHI, D.; ODEN, J. T.; FENG, X.; LIMA, E. A. B. F.; HORMUTH, I. D. A.; YANKEELOV, T. E. ICES REPORT 18-09 May 2018 A Phase-Field Theory for Multi-constituent Diffusion and Deformation : Application to Avascular Tumor Growth by Diffusion and Deformation : Application to Avascular Tumor Growth. n. May, 2018.

FICK, A. Ueber diffusion. *Ann-der Phys*, v. 56, n. 94, 1855.

FOLKMAN, J. Tumor angiogenesis: therapeutic implications. *New England Journal of Medicine*, v. 285, n. 21, p. 1182–86, 1971. ISSN 0028-4793. <https://pubmed.ncbi.nlm.nih.gov/4938153/>.

FUNG, Y. *A First Course in Continuum Mechanics*. 2. ed. Prentice-Hall, 1977. 351 p. <https://ui.adsabs.harvard.edu/abs/1977ph...book.....F>.

GARG, I.; MIGA, M. I. Preliminary investigation of the inhibitory effects of mechanical stress in tumor growth. *Medical Imaging 2008: Visualization, Image-guided Procedures, and Modeling*, v. 6918, p. 69182L, 2008. ISSN 16057422. <https://doi.org/10.1117/12.773376>.

GARIKIPATI, K. The Kinematics of Biological Growth. *Applied Mechanics Reviews*, v. 6, p. 7, 2009. <https://doi.org/10.1115/1.3090829>.

GOMEZ, H.; CALO, V. M.; BAZILEVS, Y.; HUGHES, T. J. Isogeometric analysis of the Cahn–Hilliard phase-field model. *Computer Methods in Applied Mechanics and Engineering*, v. 197, n. 49-50, p. 4333–4352, sep 2008. ISSN 00457825. <https://linkinghub.elsevier.com/retrieve/pii/S0045782508001953>.

GOMEZ, H.; ZEE, K. G. van der. *Computational Phase-Field Modeling*. American Cancer Society, 2017. 1–35 p. ISBN 9781119176817. <https://onlinelibrary.wiley.com/doi/abs/10.1002/9781119176817.ecm2118>.

GONZALEZ, O.; STUARTT, A. M. *A First Course in Continuum Mechanics*. 1. ed. New York: Cambridge University Press, 2008. 414 p. ISBN 978-0-521-88680-2. <www.cambridge.org/9780521886802>.

GORIELY, A. *The Mathematics and Mechanics of Biological Growth*. New York, NY: Springer New York, 2017. v. 45. (Interdisciplinary Applied Mathematics, v. 45). ISBN 978-0-387-87709-9. <http://link.springer.com/10.1007/978-0-387-87710-5>.

GREENSPAN, H. On the growth and stability of cell cultures and solid tumors. *Journal of Theoretical Biology*, v. 56, n. 1, p. 229 – 242, 1976. ISSN 0022-5193. <http://www.sciencedirect.com/science/article/pii/S0022519376800549>.

GURTIN, M. E. Generalized Ginzburg-Landau and Cahn-Hilliard equations based on a microforce balance. *Physica D: Nonlinear Phenomena*, v. 92, p. 178–192, 1996. <https://doi.org/10.1016/0167-2789(95)00173-5>.

GURTIN, M. E.; FRIED, E.; ANAND, L. *The Mechanics and Thermodynamics of Continua*. Cambridge University Press, 2010. 694 p. ISBN 9781139482158. <https://doi.org/10.1017/CBO9780511762956>.

HACKETT, R. M. *Hyperelasticity Primer*. Cham: Springer International Publishing, 2016. 1–170 p. ISBN 978-3-319-23272-0. <http://link.springer.com/10.1007/978-3-319-23273-7>.

HANAHAN, D.; WEINBERG, R. A. The Hallmarks of Cancer - Review. *Cell*, v. 100, p. 57–70, 2000. <https://doi.org/10.1016/S0092-8674(00)81683-9>.

HANAHAN, D.; WEINBERG, R. A. Hallmarks of cancer: The next generation. *Cell*, Elsevier Inc., v. 144, n. 5, p. 646–674, 2011. ISSN 00928674. <http://dx.doi.org/10.1016/j.cell.2011.02.013>.

HARRIS, A. L. Hypoxia a key Regulatory Factor in Tumour Growth. *Nature Reviews Cancer*, v. 2, n. 1, p. 38–47, 2002. ISSN 14741768. <http://www.nature.com/doifinder/10.1038/nrc704>.

HAWKINS, A.; ZEE, K. G. V. D.; ODEN, J. T. Numerical simulation of a thermodynamically consistent four-species tumor growth model. *International Journal for Numerical Methods in Biomedical Engineering*, n. July, p. 3–24, 2011. <https://doi.org/10.1002/cnm.1467>.

HELLSTRÖM, M.; PHNG, L. K.; HOFMANN, J. J.; WALLGARD, E.; COULTAS, L.; LINDBLOM, P.; ALVA, J.; NILSSON, A. K.; KARLSSON, L.; GAIANO, N.; YOON, K.; ROSSANT, J.; IRUELA-ARISPE, M. L.; KALÉN, M.; GERHARDT, H.; BETSHOLTZ, C. Dll4 signalling through Notch1 regulates formation of tip cells during angiogenesis. *Nature*, v. 445, n. 7129, p. 776–780, 2007. ISSN 14764687. <https://doi.org/10.1038/nature05571>.

HILL A. V., P. R. S. L. The diffusion of oxygen and lactic acid through tissues. *Proceedings of the Royal Society of London. Series B, Containing Papers of a Biological Character*, v. 104, n. 728, p. 39–96, 1928. ISSN 0950-1193. <https://doi.org/10.1098/rspb.1928.0064>.

HUGHES, T. J. R.; COTTRELL, J. A.; BAZILEVS, Y. Isogeometric analysis: CAD, finite elements, NURBS, exact geometry and mesh refinement. *Computer Methods in Applied Mechanics and Engineering*, Elsevier, v. 194, n. 39, p. 4135–4195, 2005. <https://doi.org/10.1016/j.cma.2004.10.008>.

JAIN, R. K. Normalization of Tumor Vasculature: An Emerging Concept in Antiangiogenic Therapy. *Science*, v. 307, n. 5706, p. 58–62, 2005. ISSN 0036-8075. <http://www.sciencemag.org/cgi/doi/10.1126/science.1104819>.

JAIN, R. K.; MARTIN, J. D.; STYLIANOPOULOS, T. The Role of Mechanical Forces in Tumor Growth and Therapy. *Annual Review of Biomedical Engineering*, v. 16, n. 1, p. 321–346, 2014. ISSN 1523-9829. <https://doi.org/10.1146/annurev-bioeng-071813-105259>.

KOIKE, C.; MCKEE, T. D.; PLUEN, A.; RAMANUJAN, S.; BURTON, K.; MUNN, L. L.; BOUCHER, Y.; JAIN, R. K. Solid stress facilitates spheroid formation: potential involvement of hyaluronan. *British Journal of Cancer*, v. 86, p. 947 – 953, 2002. <https://doi.org/10.1038/sj.bjc.6600158>.

KOUMOUTSAKOS, P.; PIVKIN, I.; MILDE, F. The Fluid Mechanics of Cancer and Its Therapy. *Annual Review of Fluid Mechanics*, v. 45, n. 1, p. 325–355, 2013. ISSN 0066-4189. <http://www.annualreviews.org/doi/10.1146/annurev-fluid-120710-101102>.

LAIRD, A. K. Dynamics of tumor growth. *British Journal of Cancer*, v. 18, n. 3, p. 490–502, 1964. ISSN 15321827. <https://doi.org/10.1038/bjc.1964.55>.

LEE, E. H. Elastic-Plastic Deformation at Finite Strains. *Journal of Applied Mechanics*, v. 36, n. 1, p. 1–6, mar 1969. ISSN 0021-8936. <https://asmedigitalcollection.asme.org/appliedmechanics/article/36/1/1/424373/ElasticPlastic-Deformation-at-Finite-Strains>.

LIMA, E. A.; ODEN, J. T.; HORMUTH, D. A.; YANKEELOV, T. E.; ALMEIDA, R. C. Selection, calibration, and validation of models of tumor growth. *Mathematical Models and Methods in Applied Sciences*, v. 26, n. 12, p. 2341–2368, 2016. ISSN 02182025. <https://doi.org/10.1142/S021820251650055X>.

LIMA, E. A. B. F.; ODEN, J. T.; ALMEIDA, R. C. A hybrid ten-species phase-field model of tumor growth. *Mathematical Models and Methods in Applied Sciences*, v. 24, n. 13, p. 2569–2599, 2014. ISSN 0218-2025. <http://www.worldscientific.com/doi/abs/10.1142/S0218202514500304>.

LIU, J.; DEDÈ, L.; EVANS, J. A.; BORDEN, M. J.; HUGHES, T. J. Isogeometric analysis of the advective Cahn-Hilliard equation: Spinodal decomposition under shear flow. *Journal of Computational Physics*, v. 242, p. 321–350, 2013. ISSN 10902716. <http://dx.doi.org/10.1016/j.jcp.2013.02.008>.

LOWENGRUB, J. S.; FRIEBOES, H. B.; JIN, F.; CHUANG, Y.-L.; LI, X.; MACKLIN, P.; WISE, S. M.; CRISTINI, V. Nonlinear modelling of cancer: bridging the gap between cells and tumours. *Nonlinearity*, IOP Publishing, v. 23, n. 1, p. R1–R91, dec 2009. <https://doi.org/10.1088%2F0951-7715%2F23%2F1%2Fr01>.

LU, J.; YANG, G.; GE, J. Blending NURBS and Lagrangian representations in isogeometric analysis. *Computer Methods in Applied Mechanics and Engineering*, Elsevier B.V., v. 257, p. 117–125, 2013. ISSN 00457825. <http://dx.doi.org/10.1016/j.cma.2013.01.012>.

MACLAURIN, J.; CHAPMAN, J.; JONES, G. W.; ROOSE, T. The buckling of capillaries in solid tumours. *Proceedings of the Royal Society A: Mathematical, Physical and Engineering Sciences*, v. 468, n. 2148, p. 4123–4145, dec 2012. ISSN 1364-5021. <https://royalsocietypublishing.org/doi/10.1098/rspa.2012.0418>.

MANTZARIS, N. V.; WEBB, S.; OTHMER, H. G. Mathematical modeling of tumor-induced angiogenesis. *Journal of Mathematical Biology*, v. 49, n. 2, p. 111–187, 2004. ISSN 03036812. <https://doi.org/10.1007/s00285-003-0262-2>.

MOELANS, N.; BLANPAIN, B.; WOLLANTS, P. An introduction to phase-field modeling of microstructure evolution. *Calphad: Computer Coupling of Phase Diagrams and Thermochemistry*, v. 32, n. 2, p. 268–294, 2008. ISSN 03645916. <https://doi.org/10.1016/j.calphad.2007.11.003>.

MOORE, J. V.; HASLETON, P.; BUCKLEY, C. Tumour cords in 52 human bronchial and cervical squamous cell carcinomas: Inferences for their cellular kinetics and radiobiology. *Br. J. Cancer*, v. 51, p. 407–413, 1985. <https://doi.org/10.1038/bjc.1985.55>.

MOORE, J. V.; HOPKINS, H. A.; LOONEY, W. B. Tumour-cord parameters in two rat hepatomas that differ in their radiobiological oxygenation status. *Radiation and Environmental Biophysics*, v. 23, n. 3, p. 213–222, 1984. ISSN 0301634X. <https://doi.org/10.1007/BF01213223>.

MORELAND, K.; AYACHIT, U.; GEVECI, B.; QUAMMEN, C.; DEMARLE, D.; MORELAND, K.; BAUER, A.; BOECKEL, B.; LIPSA, D.; WESTPHAL, M.; POUDEROUX, J.; WALDON, S.; CHOUDHARY, A.; PHILIP, S.; ZAGARIS, G.; LORING, B.; MAXWELL, T.; PATCHETT, J.; AHRENS, J.; NOUANESENGSY, B.; SHERMAN, B. The ParaView Guide. *Sandia National Laboratories*, p. 251, 2016. ISSN 19357524. <https://www.paraview.org/>.

MPEKRIS, F.; ANGELI, S.; PIRENTIS, A. P.; STYLIANOPOULOS, T. Stress-mediated progression of solid tumors: effect of mechanical stress on tissue oxygenation, cancer cell proliferation, and drug delivery. *Biomechanics and Modeling in Mechanobiology*, Springer Berlin Heidelberg, v. 14, n. 6, p. 1391–1402, nov 2015. ISSN 1617-7959. <http://link.springer.com/10.1007/s10237-015-0682-0>.

NARAYANAN, H.; ARRUDA, E. M.; GROSH, K.; GARIKIPATI, K. The micromechanics of fluid-solid interactions during growth in porous soft biological tissue. *Biomechanics and Modeling in Mechanobiology*, v. 8, n. 3, p. 167–181, 2009. ISSN 16177959. <https://doi.org/10.1007/s10237-008-0126-1>.

NIA, H. T.; LIU, H.; SEANO, G.; DATTA, M.; JONES, D.; RAHBARI, N.; INCIO, J.; CHAUHAN, V. P.; JUNG, K.; MARTIN, J. D.; ASKOXYLAKIS, V.; PADERA, T. P.; FUKUMURA, D.; BOUCHER, Y.; HORNICEK, F. J.; GRODZINSKY, A. J.; BAISH, J. W.; MUNN, L. L.; JAIN, R. K. Solid stress and elastic energy as measures of tumour mechanopathology. *Nature Biomedical Engineering*, Nature Publishing Group, v. 1, n. 1, p. 1–11, 2017. ISSN 2157846X. <http://dx.doi.org/10.1038/s41551-016-0004>.

ODEN, J. T.; HAWKINS, A.; PRUDHOMME, S. General Diffuse-Interface Theories and an Approach To Predictive Tumor Growth Modeling. *Mathematical Models and Methods in Applied Sciences*, v. 20, n. 03, p. 477–517, 2010. ISSN 0218-2025. <http://www.worldscientific.com/doi/abs/10.1142/S0218202510004313>.

ODEN, J. T.; PRUDENCIO, E. E.; HAWKINS-DAARUD, A. Selection and assessment of phenomenological models of tumor growth. *Mathematical Models and Methods in Applied Sciences*, v. 23, n. 07, p. 1309–1338, 2013. <https://doi.org/10.1142/S0218202513500103>.

OGDEN, R. *Non-linear Elastic Deformations*. New York: Dover, 1984. 533 p. ISBN 0486696480. <https://doi.org/10.1002/zamm.19850650903>.

PADERA, T. P.; STOLL, B. R.; TOOREDMAN, J. B.; CAPEN, D.; TOMASO, E. di; JAIN, R. K. Cancer cells compress intratumour vessels. *Nature*, v. 427, n. February, p. 1, 2004. <https://doi.org/10.1038/427695a>.

PIEGL, L.; TILLER, W. *The NURBS book*. Springer, 1997. v. 35. ISSN 0009-4978. <https://www.springer.com/gp/book/9783642973857>.

RAJAGOPAL, K. R.; TAO, L. *Mechanics of Mixtures*. World Scientific, 1995. v. 35. 195 p. <https://doi.org/10.1142/2197>.

REDDY, J. N. *An Introduction to Continuum Mechanics*. 2. ed. Cambridge University Press, 2013. 450 p. <https://doi.org/10.1017/CBO9781139178952>.

RODRIGUEZ, E. K.; HOGER, A.; MCCULLOCH, A. D. Stress-dependent finite growth in soft elastic tissues. *Journal of Biomechanics*, v. 27, n. 4, p. 455–467, apr 1994. ISSN 00219290. <https://linkinghub.elsevier.com/retrieve/pii/0021929094900213>.

ROOSE, T.; CHAPMAN, S. J.; MAINI, P. K. Mathematical Models of Avascular Tumor Growth. *SIAM Review*, v. 49, n. 2, p. 179–208, 2007. ISSN 1095-7200. <https://doi.org/10.1137/S0036144504446291>.

RUDRARAJU, S.; MILLS, K. L.; KEMKEMER, R.; GARIKIPATI, K. *Computer Models in Biomechanics*. Dordrecht: Springer Netherlands, 2013. 293–303 p. ISBN 978-94-007-5463-8. <http://link.springer.com/10.1007/978-94-007-5464-5>.

S., A.; TOSIN, A. Mathematical model of tumour cord growth along the source of nutrient. *Mathematical Modelling of Natural Phenomena*, v. 2, n. 3, p. 153–177, 2007. ISSN 09735348. <https://doi.org/10.1051/mmnp:2007007>.

SAAD, Y.; SCHULTZ, H. {GMRES}: A generalized minimal residual algorithm for solving nonsymmetric linear systems. *SIAM Journal on Scientific and Statistical Computing*, Argonne National Laboratory, v. 7, n. 3, p. 856–869, 1986. <https://doi.org/10.1137/0907058>.

SCALERANDI, M.; PEGGION, F.; Capogrosso Sansone, B.; BENATI, C. Avascular and vascular phases in tumor cords growth. *Mathematical and Computer Modelling*, v. 37, n. 11, p. 1191–1200, 2003. ISSN 08957177. <https://doi.org/10.1016/S0895-7177(03)00130-4>.

STOKES, C. L.; LAUFFENBURGER, D. A. Analysis of the roles of microvessel endothelial cell random motility and chemotaxis in angiogenesis. *Journal of Theoretical Biology*, v. 152, p. 377–403, 1991. <https://doi.org/10.1016/S0022-5193(05)80201-2>.

STYLIANOPOULOS, T.; MARTIN, J. D.; CHAUHAN, V. P.; JAIN, S. R.; DIOP-FRIMPONG, B.; BARDEESY, N.; SMITH, B. L.; FERRONE, C. R.; HORNICEK, F. J.; BOUCHER, Y.; MUNN, L. L.; JAIN, R. K. Causes, consequences, and remedies for growth-induced solid stress in murine and human tumors. *Proceedings of the National Academy of Sciences*, v. 109, n. 38, p. 15101–15108, 2012. ISSN 0027-8424. <https://www.pnas.org/content/109/38/15101>.

STYLIANOPOULOS, T.; MARTIN, J. D.; SNUDERL, M.; MPEKRIS, F.; JAIN, S. R.; JAIN, R. K. Coevolution of Solid Stress and Interstitial Fluid Pressure in Tumors During Progression: Implications for Vascular Collapse. *Cancer Research*, v. 73, n. 13, p. 3833–3841, jul 2013. ISSN 0008-5472. <http://cancerres.aacrjournals.org/lookup/doi/10.1158/0008-5472.CAN-12-4521>.

SUCHTING, S.; FREITAS, C.; TORO, R. del; NOBLE, F.; BENEDITO, R.; BREANT, C.; DUARTE, A.; EICHMANN, A. The Notch ligand Delta-like 4 (Dll4) negatively regulates endothelial tip cell formation and vessel branching. *The FASEB Journal*, v. 21, n. 5, p. 3225–3230, 2007. ISSN 0892-6638. <https://doi.org/10.1096/fasebj.21.5.A15-a>.

SUN, S.; WHEELER, M. F.; OBEYESEKERE, M.; PATRICK, C. W. A deterministic model of growth factor-induced angiogenesis. *Bulletin of Mathematical Biology*, v. 67, n. 2, p. 313–337, 2005. ISSN 00928240. <https://doi.org/10.1016/j.bulm.2004.07.004>.

SZYMAŃSKA, Z.; CYTOWSKI, M.; MITCHELL, E.; MACNAMARA, C. K.; CHAPLAIN, M. A. Computational Modelling of Cancer Development and Growth: Modelling at Multiple Scales and Multiscale Modelling. *Bulletin of Mathematical Biology*, v. 80, n. 5, p. 1366–1403, 2018. ISSN 15229602. <https://doi.org/10.1007/s11538-017-0292-3>.

TABER, L. A. *Nonlinear Theory of Elasticity: Applications in Biomechanics*. 1. ed. World Scientific Pub., 2004. 399 p. ISBN 9812387358. <https://doi.org/10.1002/zamm.200790020>.

TABER, L. A. Theoretical study of Beloussov's hyper-restoration hypothesis for mechanical regulation of morphogenesis. *Biomechanics and Modeling in Mechanobiology*, v. 7, n. 6, p. 427–441, dec 2008. ISSN 1617-7959. <http://link.springer.com/10.1007/s10237-007-0106-x>.

TANNOCK, I. F.; BRISTOW, R. G.; HILL, R. P.; HARRINGTON, L. *The Basic Science of Oncology*. 5ed.. ed. McGraw Hill, 2013. 588 p. ISBN 9780071745208 / 0071745203. <https://doi.org/10.1002/hed.2880150320>.

TAYLOR, R. L. Isogeometric analysis of nearly incompressible solids. *International Journal for Numerical Methods in Engineering*, v. 87, n. 1-5, p. 273–288, jul 2011. ISSN 00295981. <http://doi.wiley.com/10.1002/nme.3048>.

TOSIN, A. Multiphase modeling and qualitative analysis of the growth of tumor cords. *Interactions*, p. 34, 2009. ISSN 15561801. <http://arxiv.org/abs/0906.5077>.

TRAVASSO, R. D. M.; POIRé, E. C.; CASTRO, M.; RODRGUEZ-MANZANEQUE, J. C.; HERNáNDEZ-MACHADO, A. Tumor angiogenesis and vascular patterning: A mathematical model. *PLOS ONE*, Public Library of Science, v. 6, n. 5, p. 1–10, 05 2011. <https://doi.org/10.1371/journal.pone.0019989>.

TRUESDELL, C. Sulle basi della termomeccanica. I. *Rend. Lincei*, n. 8, p. 22–38, 1957.

TRUESDELL, C. A. *A first course in rational continuum mechanics*. San Diego: Academic Press, 1992. 390 p. ISBN 0080873871.

VILANOVA, G.; COLOMINAS, I.; GOMEZ, H. Capillary networks in tumor angiogenesis: From discrete endothelial cells to phase-field averaged descriptions via isogeometric analysis. *International Journal for Numerical Methods in Biomedical Engineering*, v. 29, n. 1, p. 1015–1037, 2013. ISSN 20407939. <https://doi.org/10.1002/cnm.2552>.

WARD, J. P.; KING, J. R. Mathematical modelling of avascular-tumour growth. *Mathematical Medicine and Biology: A Journal of the IMA*, v. 14, n. 1, p. 39–69, 03 1997. ISSN 1477-8599. <https://doi.org/10.1093/imammb/14.1.39>.

WEINBERG, R. A. *The biology of cancer*. 2. ed. [S.l.]: Garland Science, 2014. 963 p. ISBN 9780815342199.

WEIS, J. A.; MIGA, M. I.; ARLINGHAUS, L. R.; LI, X.; CHAKRAVARTHY, A. B.; ABRAMSON, V.; FARLEY, J.; YANKEELOV, T. E. A mechanically coupled reaction-diffusion model for predicting the response of breast tumors to neoadjuvant chemotherapy. *Physics in Medicine and Biology*, v. 58, n. 17, p. 5851–5866, 2013. ISSN 00319155. <https://doi.org/10.1088%2F0031-9155%2F58%2F17%2F5851>.

XU, J.; VILANOVA, G.; GOMEZ, H. A Mathematical Model Coupling Tumor Growth and Angiogenesis. *PLoS One*, v. 11, n. 2, p. e0149422, 2016. ISSN 1932-6203. <http://dx.plos.org/10.1371/journal.pone.0149422>.

ZHU, C.; BAO, G.; WANG, N. Cell Mechanics: Mechanical Response, Cell Adhesion, and Molecular Deformation. *Annual Review of Biomedical Engineering*, v. 2, n. 1, p. 189–226, 2002. ISSN 1523-9829. <https://doi.org/10.1146/annurev.bioeng.2.1.189>.